Modeling Electronic Transport in Disordered Mesoscopic Systems

Chenyi Zhou

Department of Physics
McGill University
Montréal, Canada

February, 2020

A Thesis submitted to McGill University
in partial fulfillment of the requirements for the degree of
Doctor of Philosophy

Abstract

The aim of this thesis is to extend the theoretical framework of nonequilibrium electronic transport to incorporate quantum effects in disordered mesoscopic systems. Our theoretical methods are developed based on the diagrammatic perturbation technique formulated with the Keldysh nonequilibrium Green's functions. Given the real-space Hamiltonian of the transport system together with thermal reservoir parameters, we seek to compute the electronic structure and the charge current taking the various quantum effects into account. Following this methodology, the three most important and ubiquitous disordered mesoscopic effects are addressed, viz. weak localization, energy relaxation, and the Altshuler-Aronov (AA) effect, all of which give rise to corrections to the classical Drude description of electronic transport. Specialized theoretical methods are developed for the respective physical effects. For weak localization we develop a Cooperon-based diagrammatic scheme using the so-called dual fermion (DF) technique in order to take into account nonlocal interference processes which have been neglected in the prevailing coherent potential approximation (CPA). Numerical simulations have shown that, compared to CPA, our DF method yields more accurate results for transport properties of disordered quantum wires, and that in particular it is able to predict the negative magnetoresistance effect which is a signature of weak localization. The energy relaxation in disordered interacting wires is tackled with a self-consistent GW-CPA scheme. Using this computational method we study how the energy distribution of interacting electrons evolves under increasing interaction and external field strengths. In addition, the same computational scheme is also employed to simulate the Coulomb drag effect between parallel quantum wires. The interesting dependence of nonequilibrium drag current on the chemical potentials of reservoirs is discussed. As to the AA effect, the original diagrammatic formulation by Altshuler and Aronov is generalized to the real-space Keldysh formalism. Then, both theoretical and numerical diagram calculations show that for a disordered wire at nonequilibrium the AA effect leads to anomalous DOS corrections at its respective Fermi energies, and that the magnitudes of these (local) DOS corrections are position-dependent. The AA effect on transport properties is also analyzed, which shows nontrivial behaviors with respect to system sizes and bias voltages.

Résumé

L'objectif de cette thèse est d'étendre le cadre théorique du transport électronique pour incorporer les effets quantiques dans les systèmes mésoscopiques désordonnés. Nos méthodes théoriques sont développées sur la base de la technique de perturbation formulée avec les fonctions de Green hors d'équilibre. En utilisant l'hamiltonien de l'espace réel ainsi que des paramètres du réservoir thermique, nous cherchons à calculer la structure électronique et le courant de charge en tenant compte des différents effets quantiques. Les trois effets mésoscopiques désordonnés les plus importants et les plus répandus sont abordés, viz. la localisation faible, la relaxation d'énergie et l'effet de Altshuler-Aronov (AA), qui donnent lieu à des corrections de la description classique par Drude du transport électronique. Des méthodes théoriques spécialisées sont développées pour les effets physiques respectifs. Pour la localisation faible, nous développons un schéma de diagramme basé sur Cooperon en utilisant la technique dite du fermion dual (DF) afin de prendre en compte les processus d'interférence non locaux qui ont été négligés dans l'approximation du potentiel cohérent (CPA), qui prévaut. Des simulations numériques ont montré que, par rapport à la CPA, notre méthode de DF donne des résultats plus précis pour les propriétés de transport de fils quantiques désordonnés, et qu'elle est notamment capable de prédire l'effet de magnétorésistance négatif, ce qui est la signature de localisation faible. La relaxation d'énergie dans les fils en interaction est abordée avec un schéma auto-cohérent GW -CPA. À l'aide de cette méthode, nous étudions comment la distribution de l'énergie des électrons en interaction évolue sous l'effet de l'interaction croissante et de l'intensité du champ externe. De plus, le même schéma de calcul est également utilisé pour simuler l'effet de traînée de Coulomb entre des fils parallèles. On discute la dépendance intéressante du courant de traînée sur les potentiels chimiques des réservoirs. En ce qui concerne l'effet de AA, la formulation diagrammatique originale d'Altshuler et Aronov est généralisée au formalisme de Keldysh dans l'espace réel. Ensuite, les calculs théoriques et numériques montrent que pour un fil hors d'équilibre, l'effet AA conduit à des corrections de DOS anormales à ses énergies de Fermi respectives, et que l'ampleur de ces corrections (locales) dépend de la position. L'effet AA sur les propriétés de transport est également analysé, ce qui mène à des comportements non triviaux aux tailles de système et tensions.

Statement of Originality

This thesis is aimed to extend the existing simulation framework for electronic transport to incorporate the quantum effects in disordered mesoscopic systems. The main contributions include:

- Formulation of the general diagrammatic scheme to calculate disorder-averaged Green's function correlators (Section 2.2.2). The theoretical framework was published in Ref.[1].
- The real-space Keldysh version of the dual fermion formalism, and the associated Cooperon-based diagrammatic scheme (Section 3.3.2). This was published in Ref.[2].
- The self-consistent GW-CPA numerical scheme to study energy relaxation effects (Chapter 4). This, together with its application to Coulomb drag between quantum wires, was reported in Ref.[3]. Besides, the electron-hole relation in the linear response Coulomb drag has been generalized to the nonlinear transport regime (Appendix C).
- Diagrammatic formalism and its numerical implementation for Altshuler-Aronov effects in short nonequilibrium wires (Chapter 5). The main results were reported in Ref.[4].

Apart from the above contributions focused by this thesis, during the course of my PhD study I have also studied the transient transport of disordered quantum dots. The associated work was published in Ref.[5].

Acknowledgements

I gratefully thank my supervisor Prof. Hong Guo for giving me this precious opportunity to do research on the doctoral level. This thesis, along with other research works, could not have been completed without his constant guidance and encouragement. Yet, what I have benefited the most from him is his refreshing ideas and insights in the physical problems. I should also thank him for establishing such a nice amazing research group. My studies in the domain of quantum transport had a very smooth start owing to the help from Prof. Lei Zhang and Prof. Xiao-Bin Chen. I owe thanks to Dr. Eric Zhu, Dr. Qing Shi, and Dr. Jia-Wei Yan for valuable discussions on disordered electronic transport, and to Dr. Ying-Chih Chen for the same reason on the GW method. I thank Prof. Xiao-Hong Zheng, Dr. Vincent Michaud-Rioux, and Dr. Mohammed Harb for advices on numerical computation techniques. Besides, many of my colleagues helped me understand the interesting subjects of their own research projects. Although not directly related to my thesis, those discussions have been just equally valuable, for they are basic elements of my student life. In particular, Prof. Hao-Ran Chang introduced to me the elementary quantum field theory. Dr. Chen Hu and Dr. Mao-Yuan Wang taught me many things about topological matters. I benefited from discussions with Raphaël Prentki on device physics. Prof. Zhong-Li Liu and Dr. Peng Kang introduced to me the techniques of materials informatics. I thank Dr. Xiang-Hua Kong for sharing experience on semiconductor simulations, and especially for her efforts in fighting for computational resources for the group.

Notation and abbreviations

$C^{(n)}$	disorder-averaged product of n Green's functions
d	dimension
D	diffusion constant
e	electron charge
f	Fermi-Dirac distribution
G	Green's function
$\mathcal{G}$	conductance
H	Hamiltonian
I	charge current
J	energy current
k_{B}	Boltzmann constant
$K^{(n)}$	diagrammatic kernel
L	wire length, diagrammatic ladder
P	electronic polarization
$\mathcal{P}$	propagator of particle density
T	temperature
U	bare Coulomb potential
V	bias voltage
v	impurity potential
W	screened e-e interaction, wire width
γ	cumulant of impurity potential
σ	electrical conductivity
Σ	self-energy
AA	Altshuler-Aronov
CPA	coherent potential approximation
DF	dual-fermion
DOS	density of states

Contents

1 Introduction **1**

2 Green's function formalism **7**

- 2.1 Keldysh formalism . . . 8
  - 2.1.1 Complex-time contour . . . 9
  - 2.1.2 Real-time formalism . . . 10
- 2.2 Impurity scattering and disorder-average . . . 13
  - 2.2.1 One-particle Green's function . . . 14
  - 2.2.2 General Green's function correlators . . . 16
- 2.3 Electron-electron interaction . . . 21
  - 2.3.1 Hedin equations . . . 21
  - 2.3.2 Diagrammatic formalism . . . 23
- 2.4 Conserving approximation . . . 26
  - 2.4.1 Kadanoff-Baym scheme . . . 26
  - 2.4.2 Ward identity . . . 28
- 2.5 Transport model . . . 30
  - 2.5.1 System partition . . . 30
  - 2.5.2 Block Green's functions . . . 32
  - 2.5.3 Charge current calculation . . . 33
  - 2.5.4 Discretization . . . 35
- 2.6 Summary . . . 37

3 Quantum diffusion and localization **38**

- 3.1 General picture . . . 39
- 3.2 Propagator formalism . . . 41
- 3.3 Locator formalism . . . 46
  - 3.3.1 Coherent potential approximation . . . 48

3.3.2 Dual fermion method 51
3.4 Numerical studies 55
3.5 Summary 59

4 Energy relaxation due to e-e interaction 61
4.1 The *GW* method 63
4.2 Applications 67
4.2.1 Nonequilibrium energy distribution 68
4.2.2 Coulomb drag 69
4.3 Summary 75

5 Altshuler-Aronov effects 76
5.1 Theoretical analyses 78
5.1.1 Density of states 79
5.1.2 Charge current 85
5.2 Numerical implementation 90
5.3 Numerical studies 95
5.4 Summary 100

6 Conclusions 101

A Fourier transforms 104

B Diffusive approximation 107

C Electron-hole symmetry in nonequilibrium Coulomb drag 111

Chapter 1

Introduction

A generic transport system is composed of (at least) two particle reservoirs sandwiching a device sample in the middle, as schematically illustrated in Fig.1.1. The reservoirs have their respective temperatures and chemical potentials that are well defined at thermal equilibrium. In a real-life experimental setup, these reservoirs typically correspond to electric leads or electrodes that bridge between the device and the outer circuit. The device structure at the center is where our interest lies; it can be any material ranging from single molecules to macroscopic chunks. Electrons enter and exit the central device region via particle exchange with the reservoirs. The central task of a transport experiment is to characterize the electric response of the given system, and the objective of theoretical modeling consists in identifying the dominant physical processes which lead to such transport behaviors and thence making further predictions.

In theoretical analyses, the reservoirs can be simply treated as noninteracting quasiparticles, as admitted by the celebrated Fermi liquid theory [6] of metals, while in the central region electrons

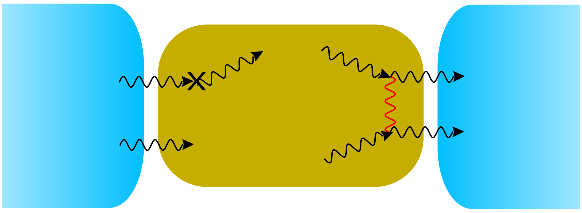

Figure 1.1: Schematic of a generic transport structure. The blue areas represent electronic reservoirs, and the yellow block represents the mesoscopic sample of interest. Note that such a system division is purely conceptual: the interfaces between the device and reservoirs may not coincide with those of real materials. In the central area, electrons (black wavy lines) may interact with impurities (cross) or themselves via Coulomb potential (red wavy line).

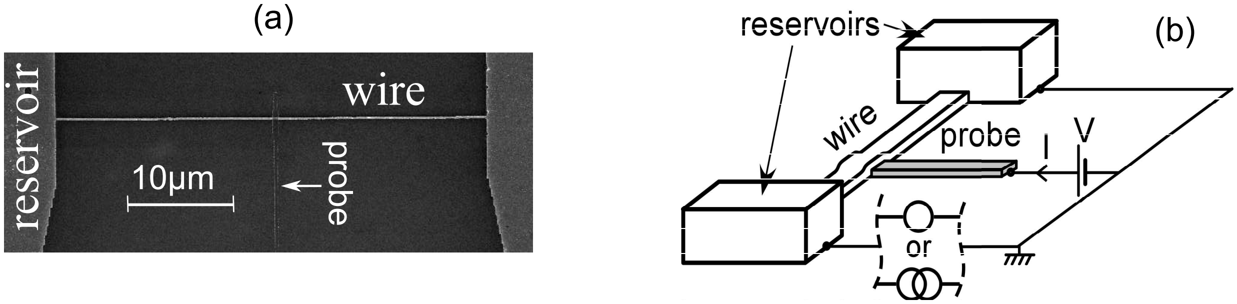

Figure 1.2: (a) Scanning electron microscope image of a silver wire fabricated using electron-beam lithography and deposition techniques. The wire is connected to external reservoirs made of large metallic pads. The probe, made of aluminum and connected to the wire through a tunnel contact, serves to investigate the local electronic structure of the wire. (b) Schematic of the transport system. Figure courtesy of Refs.[10, 11].

may encounter much messier situations such as materials imperfections, many-body interaction, and scattering off other quasiparticles (e.g. phonons). Phenomenologically, the effectiveness of certain elementary scattering process can be characterized by its associated length scale (i.e. mean free path), and the relative magnitudes of these length scales with respect to the sample-specific parameters determine the overall features of the manifested transport physics, as well as the suitable theoretical formalism in order to describe them. For example, in macroscopic materials the electronic transport typically exhibits a diffusive behavior as classical particles. This is because the electron-phonon mean free path is by orders smaller than the sample size. Local equilibriums are established under continuous dissipation of electronic energy into the phonon reservoir through the Joule heating process, and as such the kinetics of the electronic system is well described by the semiclassical Boltzmann equation [7]. In the other extremity that the device is made of a small molecule, its transport should be instead addressed within the quantum scattering formalism [8, 9] where electrons are rather pictured as wave beams transmitted along leads subject to scattering off the molecule.

The notion of *mesoscopic* transport applies to the generic regime where the wave nature of electrons plays an important role in determining the transport properties, and their dynamics must be accounted for through the quantum equation of motion. Although mesoscopic physics is not tied with any particular geometric length scales, preparing a mesoscopic sample does often require downsizing the sample size (L). As an example, Fig.1.2(a) shows a scanning electron microscope image of a μm-scale silver wire operated in the mesoscopic regime [11]. The wire is connected to two electronic reservoirs made of large metallic pads. Its transport response can be directly measured by applying a voltage difference between the reservoirs. Besides, to investigate the electronic structure in the wire, a probe is added on the side, which forms a tunnel junction with the wire. The local electronic structure at the junction can be thus probed with the differential tunnel conductance dI/dV (see illustration in Fig.1.2b), which is approximately proportional to the local density of states (DOS) of the wire [12]. Using the same apparatus as in Fig.1.2(b) but with a superconducting probe, one is able to infer the one-electron energy distribution function by deconvoluting dI/dV with the known superconductor DOS [13–15]. For nanoscale mesoscopic structures, the on-chip probe is usually replaced with a scanning tunneling microscope, which offers an atomic level resolution of DOS measurement [16, 17].

Apart from a small sample dimension, mesoscopic devices are often operated at sufficiently low temperatures so as to freeze most collective excitations, especially to suppress phonon modes that may severely destruct the phase coherence of electrons. Therefore, the remaining pertinent scattering processes are often associated with the ubiquitous electron-electron (e-e) and electron-impurity interactions.

This thesis is focused on mesoscopic systems which contain disordered impurities in the atomistic structure. In contrast to e-e scattering, the restriction of momentum conservation is lifted for the e-impurity scattering, and therefore the latter can deflect electrons more effectively. An important parameter that measures the effectiveness of e-impurity scattering is the ratio λ_{F}/l_0 between the Fermi wavelength and the elastic mean free path. In the weakly disordered limit $\lambda_{\mathrm{F}}/l_0 \ll 1$, impurities are far apart and thus the scattering events could be regarded *nearly* independent, rendering electronic motion diffusive from a local point of view. Nevertheless, static impurities without internal degrees of freedom deflect electrons elastically, so that the electronic phase coherence is preserved, and interferences between scattered waves amount to additional contributions to the transport process. They turn out to be not so negligible even if $\lambda_{\mathrm{F}} \ll l_0 \ll L$, because interferences can extend across the entire sample in the mesoscopic regime and somehow do not cancel out. For nonmagnetic impurities in normal metals, the interference induced quantum correction to the diffusive conductivity,[1] so called weak localization, can be estimated to the leading order [12]:

$$\delta\sigma = \begin{cases} -e^2 h^{-1}(L_\phi - l_0) & d=1 \\ -\pi^{-1} e^2 h^{-1} \ln L_\phi / l_0 & d=2 \end{cases} \tag{1.1}$$

where L_ϕ (typically $l_0 \ll L_\phi$) denotes the dephasing length due to a weak magnetic field, the intrinsic e-e interaction, or e-phonon scattering. The effect of weak localization can typically be characterized by the phenomenon of negative magnetoresistance in mesoscopic conductors, as illustrated in Fig.1.3(a). The plot shows the magnetoconductance curve for a short one-dimensional

---

[1] For non-interacting Fermi-gas, the conductivity is given by the classical formula $\sigma_{\mathrm{d}} = e^2 D \nu_0$, where D is diffusion coefficient and ν_0 is electronic density of states at the Fermi energy.

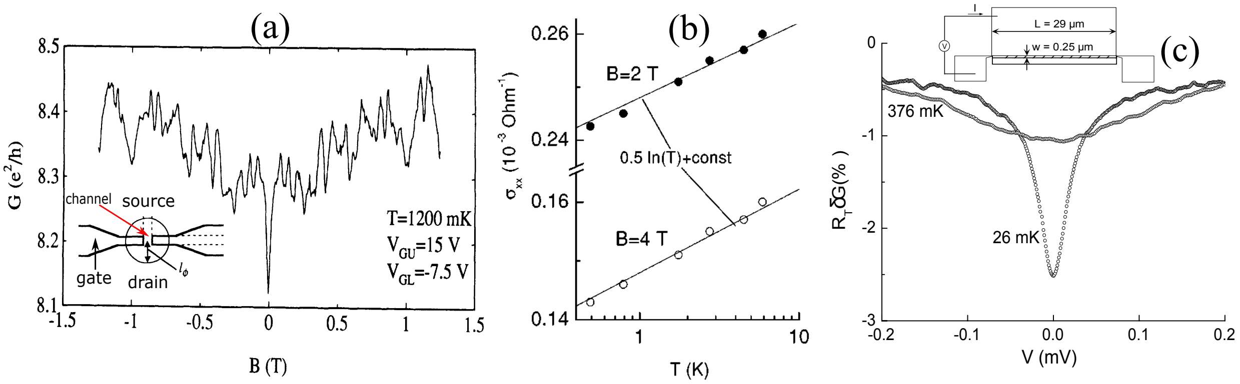

Figure 1.3: (a) Magnetoconductance curve for a short (~1μm) one-dimensional channel fabricated in silicon MOSFET [18]. Inset: device schematic. (b) Temperature dependence of longitudinal conductivity for a doped quantum well formed by GaAs-In$_{0.15}$Ga$_{0.85}$As heterostructures [19]. (c) Suppression of tunnel conductance between a 29μm-long aluminum wire and a thick film [20]. Inset: device schematic. Figure courtesy of Refs.[18–20].

channel fabricated in a silicon MOSFET [18]. The conductance is lowest at zero magnetic field due to impurity induced localization; it increases with an increasing field because of the increasing dephasing rate (corresponding to decreasing L_ϕ) which suppresses the interferences contributing to localization.

Going beyond the single-particle formalism, we next discuss the impacts of e-e scattering on electronic transport. In Fermi liquid based systems, major effects of e-e interaction have already been removed through the renormalization procedure, and the residual part can thus be tackled perturbatively. Under the weak interaction assumption, three particular many-body effects are usually considered for mesoscopic transport, viz. energy relaxation, many-body dephasing, and the Altshuler-Aronov (AA) effect [21]. Because of the low temperature setting and the quasiparticle basis, energy relaxation is often considered ineffective in the mesoscopic regime, except under a nonlinear condition. In this case the existence of separate Fermi surfaces would largely drive the relaxation process and thus distorts the electronic structure [14]. Compared to energy relaxation, dephasing is believed to be more ubiquitous since it does not necessitate a considerable amount of energy transfer [22, 23]. Rather, dephasing arises from the interaction between an electron and the fluctuating electric field in the background formed by other electrons: part of the phase information becomes intractable when ensemble average is taken over this fluctuating field [24]. This effect often serves as an upper bound for certain physical processes to which interferences are important, such as the weak localization discussed in Eq.(1.1). Whereas energy relaxation and phase decoherence exist in many-electron systems with or without disordered impurities, the AA effect is specific to disordered systems. As first elucidated by Altshuler and Aronov [21], due to e-e interaction, the nonuniform potential formed by impurities can reshape the charge distribution in the system, which acts as extra scatterers to individual electrons. The thus scattered waves interfere with those from static impurities, leading to additional conductivity suppression to the same order as Eq.(1.1). In particular, AA showed that this conductivity suppression can be written in the same form as Eq.(1.1) (up to a numeric prefactor), with L_ϕ replaced by the thermal diffusion length $L_T = \sqrt{\hbar D/k_B T}$. One thus immediately sees that the AA effect should induce a conductivity correction dependent on temperatures. This has indeed been confirmed by experiments [19, 25–27], as illustrated in Fig.1.3(b) [19], which shows a logarithmic temperature dependence for a two-dimensional quantum well. Apart from its impact on electric conductivity, at low temperatures the AA mechanism also leads to drastic changes in the electronic structure around the Fermi surface [21]. Figure 1.3(c) displays the differential tunnel conductance of a disordered aluminum wire placed over a thick electrode [20]. As can be seen, with decreasing temperature, states at the Fermi energy tend to get depleted. Such phenomenon, so-called “zero bias anomaly”, has also been observed in other low-temperature disordered systems [28–31].

The two theoretical formalisms that serve as workhorses in mesoscopic physics are the Kubo formula and the nonequilibrium Green’s functions [32, 33]. The Kubo formula is based on the equilibrium fluctuation-dissipation theorem which relates the linear response coefficients (i.e. dissipation) to the noises in corresponding observables. Many basic understandings about mesoscopic transport were originally derived from the Kubo formula, including the conductivity correction aforementioned in Eq.(1.1) [21, 34]. The Kubo formalism is most conveniently implemented in the reciprocal space with virtually infinite systems, namely the system size is presumed to be greater than any other length scales in the problem, whereby many-body diagram calculations can be much simplified. Recent advances in nanotechnology have shrunk electronic devices down to a scale where the material structures, including those of the reservoirs, can be engineered at an atomistic level [35–37]. This constantly growing field therefore calls for modeling methods which function directly in the real space. However, naively applying the Fourier transform to existent diagrammatic schemes formulated in reciprocal space does not necessarily permit meaningful results in the real space; in particular, additional diagrams are often needed in order to ensure the most basic conservation laws [38, 39]. Most importantly, nanodevices can be easily driven into the nonlinear regime, to which the Kubo formalism is just inapplicable. In order to address these problems, we shall employ the nonequilibrium Green’s function technique, which offers a unified approach to systems both in and out of equilibrium. What’s more, its numerical compatibility makes it by far the most promising framework for *ab initio* device simulations [40, 41].

The central spirit of this thesis is adapting already existent concepts of mesoscopic transport to the nonequilibrium Green's function formalism, devising simulation methods in conjunction with numerical models, and studying what would become of those many-body quantum effects when the finiteness of sample size becomes relevant (e.g. $L_\phi, L_T > L$) or when the system enters a nonlinear transport regime. Throughout the course, we shall constantly accentuate the importance of charge conservation, which should be used as a guideline to construct our theoretical formalism and also to serve as a sanity check for our numerical results.

The organization of the thesis is as follows.

In Chapter 2, we review the general nonequilibrium Green's function theory for systems in the presence of e-e interaction and disordered impurities. Diagram rules are given under the framework of many-body perturbation. The general theoretical formalism is adapted to the mesoscopic transport problem by noticing that the effect of electronic reservoirs simply amounts to a self-energy term in the finite central region, and thus the charge current can be calculated from nonequilibrium Green's functions within a finite dimension.

Chapter 3 specializes in disordered systems where e-e interaction is neglected. Two subjects are addressed there: quantum diffusion and (weak) localization. We start heuristically by reviewing the basic physical pictures underlying these processes using the notion of quantum paths. We then introduce the numerical methods of the coherent potential approximation (CPA) and the dual fermion (DF) theory, which respectively deal with the diffusion and localization processes. CPA is essentially an effective mean field theory, and DF can be regarded as a diagrammatic extension to CPA that takes nonlocal interferences into account. The two methods are implemented on a discrete lattice model, and their performances are evaluated.

In Chapter 4, we formulate the self-consistent GW-CPA scheme which captures the energy relaxation effect of nonlinear transport in systems containing both e-e interaction and disordered impurities. The numerical formalism is applied to studying the electronic energy distribution [14] and the Coulomb drag effect [42] in quantum wire systems.

In Chapter 5, the AA effect due to coupling between e-e interaction and impurity scattering is investigated using Keldysh diagram techniques. In particular, we analyze its impact on the conductance and the local DOS of nonequilibrium short wires. Theoretical and numerical calculations in this chapter are performed at zero temperature, so that the system size L, instead of L_T, becomes the dominant cutoff length scale for long-ranged correlations.

We relegate a few technical details to the appendices, which cover the topics of numeric Fourier transform, the Green's function techniques under weak disorder, and the electron-hole symmetry in nonequilibrium Coulomb drag.

Chapter 2

Green's function formalism

The theoretical formulation of this chapter is based on the following Hamiltonian:

$$H(t) = \int d\mathbf{r}d\mathbf{r}'\hat{\psi}^\dagger(\mathbf{r})H_0(\mathbf{r},\mathbf{r}',t)\hat{\psi}(\mathbf{r}') + \int d\mathbf{r}v(\mathbf{r},t)\hat{n}(\mathbf{r}) + \frac{1}{2}\int d\mathbf{r}d\mathbf{r}'U(\mathbf{r},\mathbf{r}',t)\hat{n}(\mathbf{r})\hat{n}(\mathbf{r}'), \quad (2.1)$$

where $\hat{\psi}$ denotes the field operator, $\hat{n}$ is the density operator, U denotes the two-body e-e interaction, v is some external scalar potential, and H_0 represents the kinetic energy:

$$H_0(\mathbf{r}_1,\mathbf{r}_2,t) = \frac{1}{2m}\Big(\mathrm{i}\nabla_{\mathbf{r}_1} + \frac{q}{c}\mathbf{A}(\mathbf{r}_1 t)\Big)^2\delta(\mathbf{r}_1-\mathbf{r}_2), \quad (2.2)$$

$\mathbf{A}$ being the vector potential. Although in this thesis only steady states will be studied, for the convenience of theoretical formulation we have assigned a time dependency to the Hamiltonian (2.1). We say that a system is noninteracting when $U = 0$, and that it is disordered if the functional form of $v(\mathbf{r})$ is drawn from a statistical ensemble.

The theoretical complexity implicated in the Hamiltonian (2.1) is on two aspects. First, the presence of two-body interaction renders the Hamiltonian non-quadratic, and thus its eigenstates cannot be expressed as a Slater determinant [6] of single-particle states. In order to diagonalize the Hamiltonian and obtain the many-body eigenstates, one needs its expression on a basis of Fock states, whose dimension however grows exponentially with system size. The quest for exact many-body eigenstates becomes even less feasible in a transport system since it technically contains infinite degrees of freedom: the many-body wavefunctions extend into the reservoirs even though the projected Hamiltonian is quadratic therein. The second complexity comes from the uncertainty of the potential distribution $v(\mathbf{r})$ when the system is disordered. Extra efforts are needed in this case to average the targeted physical property over an ensemble of $v(\mathbf{r})$, since there is no *a priori* justification whether a few selected configurations would be representative enough, especially for mesoscopic samples which often lack the so-called self-averaging property [6]. Of course, one may follow the brute-force approach that repeats the calculations under different $v(\mathbf{r})$-configurations and take average at the end. However, it is usually not sensible to do so, simply because of the huge disorder-ensemble size.

In this thesis, we use the Green's function method [33, 43] to deal with these difficulties. This method exploits the fact that most experimental observables can be naturally expressed with Green's functions and that computing exact many-body eigenstates is often unnecessary. However, this does not grant any easiness to computing the Green's functions. To alleviate the problem, in this thesis we shall only focus on the physical scenario where the many-body electronic structure is still dominated by the quadratic Hamiltonian and the possible $v(\mathbf{r})$-configurations are not too far from a certain reference. Under these conditions the Green's functions can be computed in a perturbative manner, and we know how to exactly evaluate each individual term in the series.

In this chapter, we wish to keep our theoretical formulation at a generic level. We shall review the general Green's function framework and walk through the derivations of the perturbation series for generic systems containing disorder and e-e interaction. Nevertheless, we note that any perturbation series is subject to a truncation in practice. A general principle is that the specific truncation scheme should be associated with the specified physical effect under investigation. This amounts to the subjects of later chapters.

2.1 Keldysh formalism

The Keldysh formalism is a commonly used theoretical framework to deal with quantum systems driven out of equilibrium, and it serves as the basis for Green's functions to be properly defined. In this formalism, it is assumed that the system was initially prepared in a thermodynamically equilibrium state (specified by a temperature T and a chemical potential μ) in the remote past, and then undergoes an evolution governed by the Hamiltonian $H(t)$. During the evolution the system is kept from exchanging particles with its environment. According to the basic quantum mechanics, the expectation value of an observable can hence be expressed as $O(t) = \mathrm{Tr}\left[\hat{\rho}\hat{O}_{\mathrm{H}}(t)\right]$, where $\hat{\rho}$ is the density matrix $e^{-\beta H^{\mathrm{M}}}/\mathrm{Tr}\left[e^{-\beta H^{\mathrm{M}}}\right]$ with $\beta = \frac{1}{k_B T}$ and $H^M \equiv H(t=-\infty) - \mu N$. $\hat{O}_{\mathrm{H}}(t)$ denotes the corresponding operator in the Heisenberg picture, which is related to its Schrödinger counterpart through $\hat{O}_{\mathrm{H}}(t) = \hat{U}(-\infty, t)\hat{O}(t)\hat{U}(t, -\infty)$. The evolution operator $\hat{U}$ is defined as

$$\hat{U}(t_2, t_1) = \begin{cases} T_t\left\{e^{-\mathrm{i}\int_{t_1}^{t_2} dt' H(t')}\right\}, \; t_2 > t_1 \\ \bar{T}_t\left\{e^{-\mathrm{i}\int_{t_1}^{t_2} dt' H(t')}\right\}, \; t_2 < t_1 \end{cases} \tag{2.3}$$

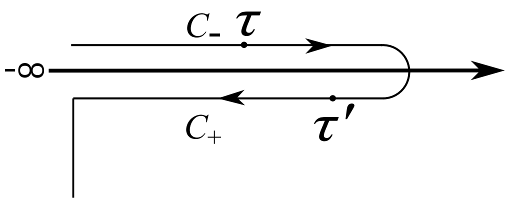

Figure 2.1: Keldysh contour [44].

where T_t ($\bar{T}_t$) is the chronological (anti-chronological) ordering operator which moves quantities with later (earlier) time arguments to the left.[1]

2.1.1 Complex-time contour

To facilitate further theoretical formulations, Keldysh introduced the idea of complex-time contour in his seminal paper [45]. The Keldysh contour (see Fig.2.1) consists of two counter-directional lines along the real-time axis plus a vertical line which runs between $-\infty$ and $-\infty - \mathrm{i}\beta$ [44]. The contour version of the Hamiltonian is defined as

$$H(\tau) = \begin{cases} H(t), \ \tau = t \pm i0^+ \\ H^{\mathrm{M}}, \ \tau \in [-\infty - i\beta, -\infty] \end{cases}$$

and accordingly, the evolution operator on the contour is defined as

$$\hat{U}(\tau_2, \tau_1) = \begin{cases} T_\tau \left\{ e^{-\mathrm{i}\int_{\tau_1}^{\tau_2} d\tau' H(\tau')} \right\}, \ \tau_2 > \tau_1 \\ \bar{T}_\tau \left\{ e^{+\mathrm{i}\int_{\tau_2}^{\tau_1} d\tau' H(\tau')} \right\}, \ \tau_2 < \tau_1 \end{cases} \tag{2.4}$$

where $\tau_2 > \tau_1$ ($\tau_2 < \tau_1$) means that τ_2 is later (earlier) than τ_1 along the direction specified on the contour. As such, the time-evolution of operators within the Heisenberg picture can be readily generalized to the contour framework:

$$\hat{O}_{\mathrm{H}}(\tau) = \hat{U}(-\infty, \tau)\hat{O}(\tau)\hat{U}(\tau, -\infty). \tag{2.5}$$

Hence one can re-express the expectation value of $\hat{O}(t)$ using the contour formula:

$$O(t) \equiv \left\langle \hat{O}_{\mathrm{H}}(\tau = t \pm \mathrm{i}0^+) \right\rangle = \frac{\mathrm{Tr}\ T_\tau \left\{ e^{-\mathrm{i}\int_C d\tau' H(\tau')} \hat{O}(\tau) \right\}}{\mathrm{Tr}\ T_\tau \left\{ e^{-\mathrm{i}\int_C d\tau' H(\tau')} \right\}}, \tag{2.6}$$

where T_τ is the chronological ordering operator defined on the contour, its order being specified by the arrows in Fig.2.1. The concise form of Eq.(2.6) shows the virtue of using the Keldysh contour.

---

[1] For fermion field operators, every swap of two adjacent operators yields a factor of -1.

Using the from of Eq.(2.6), the contour version of the general nth-order Green's function is defined as [33]

$$G^{(n)}(1,\ldots,n;1',\ldots,n') \equiv \mathrm{i}^{-n}\left\langle T_\tau\left\{\hat{\psi}_{\mathrm{H}}(1)\ldots\hat{\psi}_{\mathrm{H}}(n)\hat{\psi}^\dagger_{\mathrm{H}}(n')\ldots\hat{\psi}^\dagger_{\mathrm{H}}(1')\right\}\right\rangle, \tag{2.7}$$

where the shorthand notation $1\equiv \mathbf{r}_1\tau_1$ is used. Technically $G^{(n)}$ is encoded with all the n-particle correlations in a many-body system, and thus many physical quantities and observables can be directly extracted from it. For example, the particle density is equal to $-\mathrm{i}G(\mathbf{r}\tau,\mathbf{r}\tau^+)$ and the current density [33]

$$\mathbf{j}(\mathbf{r}t) = \lim_{\mathbf{r}\to\mathbf{r}'}\frac{e\hbar(\nabla_{\mathbf{r}'}-\nabla_{\mathbf{r}})}{2m}G(\mathbf{r}\tau,\mathbf{r}'\tau^+) + \frac{\mathrm{i}e^2}{m}\mathbf{A}(\mathbf{r}t)G(\mathbf{r}\tau,\mathbf{r}\tau^+). \tag{2.8}$$

The two-particle Green's function $G^{(2)}$ is often related to linear-response coefficients such as the dielectric polarizability and the electrical conductivity [32, 33]. Higher-order Green's functions can be used to calculate nonlinear susceptibilities [46] and sample-to-sample fluctuations in disordered systems [12, 47]. Using the equation of motion of the field operator:

$$\begin{aligned}\mathrm{i}\frac{d\hat{\psi}_{\mathrm{H}}(\mathbf{r}\tau)}{d\tau} &= \left[\hat{\psi}_{\mathrm{H}}(\mathbf{r}\tau), H(\tau)\right] \qquad (2.9)\\ &= \int d\mathbf{r}' H_0(\mathbf{r},\mathbf{r}',\tau)\hat{\psi}_{\mathrm{H}}(\mathbf{r}'\tau) + v(\mathbf{r}\tau)\hat{\psi}_{\mathrm{H}}(\mathbf{r}\tau) + \int d\mathbf{r}' U(\mathbf{r},\mathbf{r}',\tau)\hat{n}_{\mathrm{H}}(\mathbf{r}'\tau)\hat{\psi}_{\mathrm{H}}(\mathbf{r}\tau)\end{aligned}$$

in conjunction with the definition (2.7), one gets the following relation between G and $G^{(2)}$:

$$\begin{aligned}\mathrm{i}\frac{d}{d\tau_1}G(\mathbf{r}_1\tau_1,\mathbf{r}_2\tau_2) &= \delta(\mathbf{r}_1-\mathbf{r}_2)\delta(\tau_1-\tau_2) + \int d\mathbf{r}' H_0(\mathbf{r}_1,\mathbf{r}',\tau_1)G(\mathbf{r}'\tau_1,\mathbf{r}_2\tau_2)\\ &+ v(\mathbf{r}_1\tau_1)G(\mathbf{r}_1\tau_1,\mathbf{r}_2\tau_2) - \mathrm{i}\int d\tau' d\mathbf{r}' U(\mathbf{r}_1,\mathbf{r}',\tau')G^{(2)}(\mathbf{r}_1\tau_1,\mathbf{r}'\tau';\mathbf{r}_2\tau_2,\mathbf{r}'\tau'^+).\end{aligned} \tag{2.10}$$

We notice that this equation becomes closed for G when $U=0$. In this case it is possible to get an exact solution given the potential $v(\mathbf{r})$. Nevertheless, in the presence of e-e interaction the yet intangible $G^{(2)}$ gets involved. In fact all the Green's functions $G^{(n)}$ satisfy a hierarchy of equations of motions [33], which become closed only if a truncation is imposed at certain level. We shall review one of the most popular truncation schemes in Sec.2.3.1 below.

2.1.2 Real-time formalism

The complex-time formalism often leads to concise forms in theoretical formulations, but for actual calculations it is more convenient to work with real-time variables, especially for systems in steady states since the real-times can then be transformed into the Fourier space.

Depending on how the two complex-time arguments are arranged on the contour, one can introduce the following real-time one-particle Green's functions under the analytic continuation $\tau \to t \pm \mathrm{i}0^+$:

$$G(1,2) \to \begin{cases} G^{\mathrm{T}}(1,2) \equiv -\mathrm{i}\left\langle T_t\left\{\hat{\psi}_{\mathrm{H}}(1)\hat{\psi}^{\dagger}_{\mathrm{H}}(2)\right\}\right\rangle & \tau_1,\tau_2 \in C_- \\ G^{>}(1,2) \equiv -\mathrm{i}\left\langle \hat{\psi}_{\mathrm{H}}(1)\hat{\psi}^{\dagger}_{\mathrm{H}}(2)\right\rangle & \tau_1 \in C_+, \tau_2 \in C_- \\ G^{<}(1,2) \equiv +\mathrm{i}\left\langle \hat{\psi}^{\dagger}_{\mathrm{H}}(2)\hat{\psi}_{\mathrm{H}}(1)\right\rangle & \tau_1 \in C_-, \tau_2 \in C_+ \\ G^{\bar{\mathrm{T}}}(1,2) \equiv -\mathrm{i}\left\langle \bar{T}_t\left\{\hat{\psi}_{\mathrm{H}}(1)\hat{\psi}^{\dagger}_{\mathrm{H}}(2)\right\}\right\rangle & \tau_1,\tau_2 \in C_+ \end{cases} \tag{2.11}$$

where C_- (C_+) denotes the forward (backward) branch. The time-ordered (G^{T}) and anti-time-ordered ($G^{\bar{\mathrm{T}}}$) Green's functions have a causal structure and satisfy the same equation of motion as for the contour Green's function [33]. In particular, G^{T} plays a central role in the zero-temperature formalism of many-body theory [32], as it is encoded with information on virtual quantum excitations. On the other hand, the lesser ($G^{<}$) and greater ($G^{>}$) Green's functions respectively represent the correlations of electrons and holes. Their Fourier transforms with respect to the time difference $(t_1 - t_2)$ in a steady state are energy distributions of particle occupation. Assuming the exact eigenstates of the many-body Hamiltonian (denoted as $|m,n\rangle$ below) are known, the equilibrium $G^{<}$ can be expressed as

$$\begin{aligned} G^{<}(\mathbf{r}_1,\mathbf{r}_2,\omega) &= \mathrm{i}\int dt\; e^{i\omega(t_1-t_2)}\left\langle \hat{\psi}^{\dagger}_{\mathrm{H}}(\mathbf{r}_2 t_2)\hat{\psi}_{\mathrm{H}}(\mathbf{r}_1 t_1)\right\rangle \\ &= \mathrm{i}\int dt\; e^{i\omega t}\sum_{mn}\langle n|\rho\hat{\psi}^{\dagger}(\mathbf{r}_2,0)|m\rangle\langle m|e^{iHt}\hat{\psi}(\mathbf{r}_1,0)e^{-iHt}|n\rangle \\ &= \frac{2\pi\mathrm{i}}{Z}\sum_{mn}\langle n|\hat{\psi}^{\dagger}(\mathbf{r}_2,0)|m\rangle\langle m|\hat{\psi}(\mathbf{r}_1,0)|n\rangle\,\delta(\omega+E_m-E_n)e^{-\beta(E_n-\mu N_n)}, \end{aligned} \tag{2.12}$$

and $G^{>}$ has a similar expression:

$$G^{>}(\mathbf{r}_1,\mathbf{r}_2,\omega) = -\frac{2\pi\mathrm{i}}{Z}\sum_{mn}\langle n|\hat{\psi}^{\dagger}(\mathbf{r}_2,0)|m\rangle\langle m|\hat{\psi}(\mathbf{r}_1,0)|n\rangle\,\delta(\omega+E_m-E_n)e^{-\beta(E_m-\mu N_m)}. \tag{2.13}$$

It can be seen that the summands in Eqs.(2.12) and (2.13) vanish unless $N_m = N_n - 1$ and $E_m = E_n - \omega$. This leads to an important relation at equilibrium:

$$G^{>}(\omega) = -e^{\beta(\omega-\mu)}G^{<}(\omega). \tag{2.14}$$

Making use of the Fermi-Dirac distribution $f(\omega,T,\mu) = [e^{\beta(\omega-\mu)}+1]^{-1}$, one obtains from Eq.(2.14):

$$G^{<}(\omega) = \mathrm{i}f(\omega)A(\omega), \tag{2.15a}$$

$$G^{>}(\omega) = -\mathrm{i}[1 - f(\omega)]A(\omega), \tag{2.15b}$$

where $A(\omega) \equiv \mathrm{i}[G^{>}(\omega) - G^{<}(\omega)]$ is a Hermitian matrix termed the spectral function in the literature [44].

To further analyze their mathematical relations, we organize the four real-time Green's functions in a matrix form:

$$\overset{\supset}{\mathbf{G}}_{s_1 s_2}(\mathbf{r}_1\tau_1, \mathbf{r}_2\tau_2) = \left[\begin{array}{cc} G^{\mathrm{T}}(\mathbf{r}_1 t_1, \mathbf{r}_2 t_2) & G^{<}(\mathbf{r}_1 t_1, \mathbf{r}_2 t_2) \\ G^{>}(\mathbf{r}_1 t_1, \mathbf{r}_2 t_2) & G^{\bar{\mathrm{T}}}(\mathbf{r}_1 t_1, \mathbf{r}_2 t_2) \end{array} \right], \tag{2.16}$$

where the subscript s denotes an extra degree of freedom which tracks the branch of the corresponding time variable. Invoking the definition (2.11), one can easily verify that the four Green's functions are in fact linear dependant: $G^{>}(1,2) + G^{<}(1,2) = G^{\mathrm{T}}(1,2) + G^{\bar{\mathrm{T}}}(1,2)$. The extra degree of freedom can be removed by introducing the retarded (R), advanced (A), and Keldysh (K) Green's functions defined as follows:

$$G^{\mathrm{R}}(1,2) = \theta(t_1 - t_2)\left[G^{>}(1,2) - G^{<}(1,2)\right], \tag{2.17a}$$

$$G^{\mathrm{A}}(1,2) = \theta(t_2 - t_1)\left[G^{<}(1,2) - G^{>}(1,2)\right], \tag{2.17b}$$

$$G^{\mathrm{K}}(1,2) = G^{>}(1,2) + G^{<}(1,2). \tag{2.17c}$$

To reveal the mathematical structure underlying these Green's functions, we organize them in a triangular matrix:

$$\overset{\triangle}{\mathbf{G}}(1,2) = \left[\begin{array}{cc} G^{\mathrm{R}}(1,2) & 2G^{<}(1,2) \\ 0 & G^{\mathrm{A}}(1,2) \end{array} \right] \tag{2.18}$$

By definitions, the two representations $\overset{\triangle}{\mathbf{G}}$ and $\overset{\supset}{\mathbf{G}}$ are related through the rotation

$$\overset{\triangle}{\mathbf{G}} = \mathbf{R_1}\sigma_z \overset{\supset}{\mathbf{G}}\,\mathbf{R}_2, \tag{2.19}$$

where

$$\mathbf{R}_1 = \frac{1}{\sqrt{2}} \left[\begin{array}{cc} 2 & 0 \\ 1 & 1 \end{array} \right], \mathbf{R}_2 = \frac{1}{\sqrt{2}} \left[\begin{array}{cc} 1 & 0 \\ -1 & 2 \end{array} \right], \sigma_z = \left[\begin{array}{cc} 1 & 0 \\ 0 & -1 \end{array} \right] \tag{2.20}$$

The triangular form of Eq.(2.18) is especially useful when one deals with convolutional integrals between complex-time functions. To see this, consider the integral

$$D(\tau, \tau') = \int_C d\tau_1 d\tau_2 A(\tau, \tau_1) B(\tau_1, \tau_2) C(\tau_2, \tau') \tag{2.21}$$

along the Keldysh contour. This can be converted to real-time integrals by means of the matrix representation:[2]

$$\overset{\supset}{\mathbf{D}} = \overset{\supset}{\mathbf{A}}(\sigma_z \overset{\supset}{\mathbf{B}})(\sigma_z \overset{\supset}{\mathbf{C}}), \tag{2.22}$$

---

[2] The time convolutions are implied in the matrix multiplications.

where σ_z is inserted because the integral direction on C_+ is backward. Upon inserting the identity $\mathbf{R_1 R_2}$= $\mathbf{I}$, we arrive at $\overset{\triangle}{\mathbf{D}} = \overset{\triangle}{\mathbf{A}}\overset{\triangle}{\mathbf{B}}\overset{\triangle}{\mathbf{C}}$. Then, exploiting the properties of triangular matrix multiplication, we get

$$D^{\mathrm{R}} = A^{\mathrm{R}} B^{\mathrm{R}} C^{\mathrm{R}}, \tag{2.23a}$$

$$D^{\mathrm{A}} = A^{\mathrm{A}} B^{\mathrm{A}} C^{\mathrm{A}}, \tag{2.23b}$$

$$D^{<} = A^{<} B^{\mathrm{A}} C^{\mathrm{A}} + A^{\mathrm{R}} B^{<} C^{\mathrm{A}} + A^{\mathrm{R}} B^{\mathrm{R}} C^{<}. \tag{2.23c}$$

It is easy to verify that Eq.(2.23c) also holds if the $<$ superscript is replaced with $>$ or K. The generalization of Eqs.(2.23) to a serial convolution of any number of functions should be straightforward. The general rule is that, for retarded or advanced functions, one simply carries out the convolutions on the real-axis such as in Eq.(2.23a), whereas for the lesser functions one multiplies them following the sequence $\mathrm{R}...\mathrm{R} < \mathrm{A}...\mathrm{A}$ and moves $<$ from left to right for each term. This procedure is often termed "analytic continuation" in the literature [44].

2.2 Impurity scattering and disorder-average

In this section, we study the Green's functions of non-interacting electrons subject to an external potential $v(\mathbf{r})$. Without this potential and in absence of e-e interaction, a reference Green's function (G_0) can be introduced via the simplified equation of motion:

$$\mathrm{i}\frac{d}{d\tau_1} G_0(\mathbf{r}_1\tau_1, \mathbf{r}_2\tau_2) = \delta(\mathbf{r}_1 - \mathbf{r}_2)\delta(\tau_1 - \tau_2) + \int d\mathbf{r}' H_0(\mathbf{r}_1, \mathbf{r}', \tau_1) G_0(\mathbf{r}'\tau_1, \mathbf{r}_2\tau_2). \tag{2.24}$$

The solution to Eq.(2.10) with $v \neq 0, U = 0$ can hence be written as:

$$G_v(1,2) = G_0(1,2) + \int d\mathbf{r}_3\tau_3 G_0(1,3) v(3) G_v(3,2), \tag{2.25}$$

where the subscript v is used to remind that the solution G_v is dependent on $v(\mathbf{r})$. Thinking of the objects in Eq.(2.25) as matrices expressed in the time-space ($\mathbf{r}\tau$) basis, we can formally write G_v as

$$G_v = \frac{1}{G_0^{-1} - v}. \tag{2.26}$$

This gives the formal solution to the one-particle Green's function under a given $v(\mathbf{r})$. In this case, knowing G_v is also adequate for calculating $G_v^{(n)}$ at any n. However, in many situations $v(\mathbf{r})$ is not specified in the physical problem, but is rather stochastically drawn from a statistical ensemble described by some probability distributions. A concrete example is the electric potential induced by impurities in a material.[3] These impurities can be dopants, vacancies, or surface roughness, which are usually not controllable in experiments, and whose distributions vary from sample to sample. In this case computing Green's functions under one single $v(\mathbf{r})$ is not very meaningful, and rather we seek to calculate the disorder-average of $G^{(n)}$. Nevertheless, it is not so easy to calculate the disorder-average in a compact and analytic form. This is already implicated by Eq.(2.26) since the potential $v(\mathbf{r})$ appears in the denominator. One could imagine that things would only get more complicated for higher-order Green's functions $G_v^{(n)}$ since it consists of products of G_v. Therefore, this section is devoted to deriving a tractable yet approximate approach to the disorder-average problem, using the diagrammatic technique.

2.2.1 One-particle Green's function

Our approach starts with the serial form of G_v, i.e. $G_v = G_0 + G_0 v G_0 + G_0 v G_0 v G_0 + \cdots$, and thence the disorder-average of G_v equals the sum of disorder-averages of individual terms in the series. Whereas the average of the first two terms is trivial, starting from the third term, *products* of random variables get involved. Assuming $v(\mathbf{r})$ is spatially uncorrelated, the averages of these products read

$$\overline{v(\mathbf{r}_1)v(\mathbf{r}_2)} = \overline{v(\mathbf{r}_1)} \cdot \overline{v(\mathbf{r}_2)} + \underbrace{\left[\overline{v(\mathbf{r}_1)^2} - \overline{v(\mathbf{r}_1)}^2\right]}_{\gamma^{(2)}(\mathbf{r}_1)} \delta(\mathbf{r}_1 - \mathbf{r}_2) \tag{2.27a}$$

$$\begin{aligned}\overline{v(\mathbf{r}_1)v(\mathbf{r}_2)v(\mathbf{r}_3)} &= \overline{v(\mathbf{r}_1)} \cdot \overline{v(\mathbf{r}_2)} \cdot \overline{v(\mathbf{r}_3)} + \delta(\mathbf{r}_1 - \mathbf{r}_2)\gamma^{(2)}(\mathbf{r}_1)\overline{v(\mathbf{r}_3)} \\ &+ \delta(\mathbf{r}_2 - \mathbf{r}_3)\gamma^{(2)}(\mathbf{r}_2)\overline{v(\mathbf{r}_1)} + \delta(\mathbf{r}_1 - \mathbf{r}_3)\gamma^{(2)}(\mathbf{r}_1)\overline{v(\mathbf{r}_2)} \\ &+ \delta(\mathbf{r}_1 - \mathbf{r}_2)\delta(\mathbf{r}_2 - \mathbf{r}_3) \underbrace{\left[\overline{v(\mathbf{r}_1)^3} - 3\overline{v(\mathbf{r}_1)^2} \cdot \overline{v(\mathbf{r}_1)} + 2\overline{v(\mathbf{r}_1)}^3\right]}_{\gamma^{(3)}(\mathbf{r}_1)}\end{aligned} \tag{2.27b}$$

$$\overline{v(\mathbf{r}_1)v(\mathbf{r}_2)v(\mathbf{r}_3)v(\mathbf{r}_4)} = \cdots , \tag{2.27c}$$

where $\gamma^{(n)}$ is the nth cumulant of the probability distribution of $v(\mathbf{r})$.

The averaging procedure for G_v can be visualized diagrammatically by Fig.2.2, where each diagram consists of a number of solid lines representing G_0 and dashed lines representing $v(\mathbf{r})$. Upon disorder-average the dashed lines are contracted forming multi-terminal vertices whose values are one of the cumulants $\gamma^{(n)}$. Diagrams are formed by arranging these building blocks in ways that are topologically different. Note that for conciseness we have set $\overline{v(\mathbf{r})} = 0$ since the expectation

---

[3] In this thesis we only consider impurities that are static and do not have internal degrees of freedom. Thus they interact with electrons only elastically.

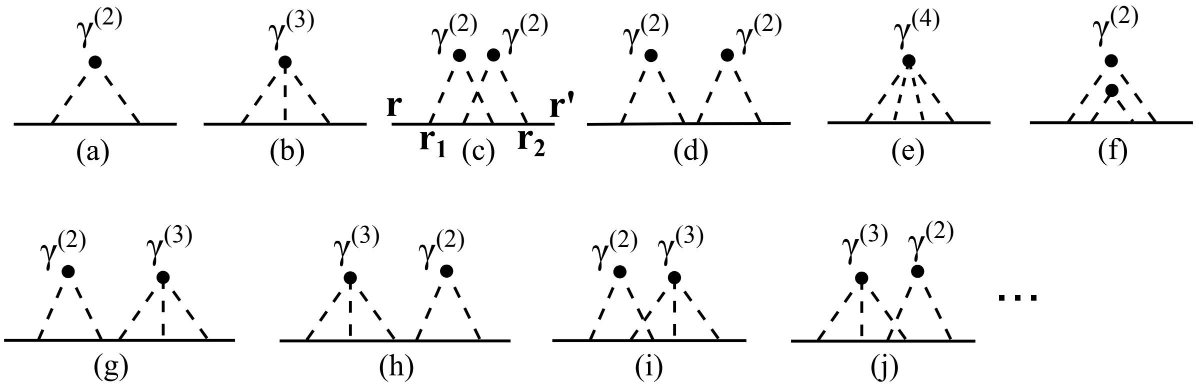

Figure 2.2: Diagrammatic representation of the perturbation series of disorder-averaged Green's function. Solid lines represent the reference Green's function G_0, and dashed lines represent cumulants of the disorder potential.

value $\overline{v(\mathbf{r})}$ can always be taken into the reference Hamiltonian. The resultant diagrams in Fig.2.2 thus do not contain "dangling" $v(\mathbf{r})$-lines. The evaluation of a diagram requires integrating over all the spatial and time arguments at the intersections. For example, Fig.2.2(c) represents

$$\begin{aligned}&\int d\mathbf{r}_1 d\mathbf{r}_2 d\tau_1 d\tau_2 d\tau_1' d\tau_2' G_0(\mathbf{r}\tau, \mathbf{r}_1\tau_1) G_0(\mathbf{r}_1\tau_1, \mathbf{r}_2\tau_2) G_0(\mathbf{r}_2\tau_2, \mathbf{r}_1{\tau_1}')\\ &\times G_0(\mathbf{r}_1{\tau_1}', \mathbf{r}_2{\tau_2}') G_0(\mathbf{r}_2{\tau_2}', \mathbf{r}'\tau')\gamma^{(2)}(\mathbf{r}_1)\gamma^{(2)}(\mathbf{r}_2).\end{aligned} \tag{2.28}$$

We notice in Fig.2.2 that there are two types of diagrams which appear redundant, as represented by Fig.2.2(d) and (f). Indeed, both Fig.2.2(d) and (f) are composed of two copies of (a): in Fig.2.2(d) the two (a)-diagrams are placed side by side, and in Fig.2.2(f) one is nested in the other. Diagrams having these two features are respectively termed reducible and non-skeleton diagrams in the literature [48]. The other diagrams, which are irreducible and skeleton, can be grouped together and formally written as $G_0\Sigma_{G_0}G_0$, where Σ is called self-energy. Note that we think of Σ as a function of the Green's function to be inserted in the diagrams. Hence the series of Fig.2.2, including reducible and non-skeleton diagrams, can be produced by iterating the following (Dyson) equation:

$$G(1,2) = G_0(1,2) + \int d3d4 G_0(1,3)\Sigma_G(3,4)G(4,2), \tag{2.29}$$

where the notation Σ_G indicates that the Σ-diagrams are now constructed with the *full* Green's function, thereby producing all the nesting diagrams such as in Fig.2.2(f). In some sense Eq.(2.29) can be viewed as a self-consistent equation for the *exact* disorder-averaged Green's function G consisting of all the terms in Fig.2.2(f), but Σ itself represents an infinite series of diagrams. Therefore, Eq.(2.29) is unsolvable unless Σ is truncated or only partially summed. Possible yet

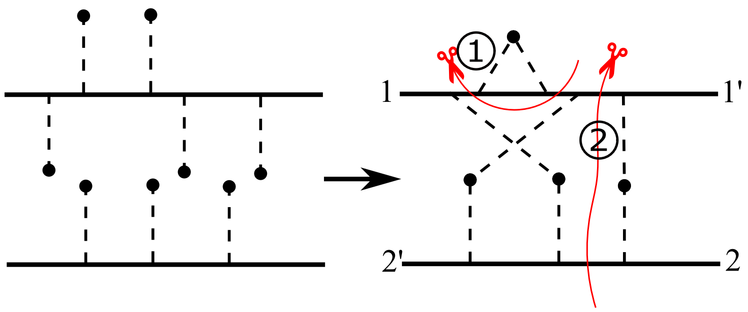

Figure 2.3: A diagram for the disorder-average product of two Green's functions. Impurity potentials (dashed lines) are connected upon disorder-average. Certain connection schemes generate reducible diagrams which can be split by cutting through two solid lines (Green's functions) without touching any dashed lines.

approximate solutions to Eq.(2.29) will be the topic of Chapter 3, where we shall consider some specific physical effects and devise our approximation schemes for the self-energy accordingly.

2.2.2 General Green's function correlators

As mentioned above, many physical quantities are related with higher-order Green's functions $G^{(n)}$, or more elementary, the disorder-average of products of one-particle Green's functions:

$$C^{(n)}(11', 22', \cdots, nn') = \langle G_v(11')G_v(22') \cdots G_v(nn') \rangle \, , \tag{2.30}$$

where $\langle \cdots \rangle$ denotes averaging over the ensemble of $v(\mathbf{r})$. Note that, since every G_v on the right-hand side explicitly depends on a common $v(\mathbf{r})$, the correlator $C^{(n)}$ cannot be simply decoupled as $\langle G_v(11')\rangle \cdot \langle G_v(22')\rangle \cdots \langle G_v(nn')\rangle$. Instead we need to apply the same diagrammatic strategy as used in Sec.2.2.1, i.e. expanding G_v with respect to v and then contracting v to form cumulant vertices. This procedure is illustrated in Fig.2.3 using the $C^{(2)}$ correlator. We notice that, in the particular contraction scheme shown on the right hand side of Fig.2.3, there is a self-energy diagram at the top which can be absorbed into the Green's function line; this part is automatically removed once the self-consistent Green's function [see Eq.(2.29)] is used in the diagrammatic construction. Another notable thing is that, if we cut along the line labeled by "2" without touching any dashed lines, the diagram can be simply split in two. Diagrams having this particular feature is said to be two-particle reducible. With this observation one can write down a general expression for $C^{(2)}$:

$$C^{(2)}(11', 22') = G(11')G(22') + G(1\bar{3})G(\bar{4}2')K^{(2)}(\bar{3}\bar{6}\bar{5}\bar{4})C^{(2)}(\bar{6}1', 2\bar{5}) \, , \tag{2.31}$$

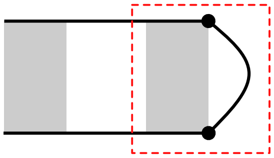

Figure 2.4: This diagram shows that adding a G-line to a reducible $C^{(2)}$-diagram cannot yield a self-energy diagram. In the figure, each grey area represents a bundle of dashed impurity-lines. The upper and lower G-lines are joined on the right side through an additional line. The resulting diagram has a nesting part as marked by the red frame, resembling Fig.2.2(f) which is excluded from the self-energy.

where G is the self-consistent Green's function and the repeated indices in the last term are integrated over. In fact, Eq.(2.31) would become exact if the kernel function $K^{(2)}$ included all the two-particle *irreducible* diagrams. Nevertheless, similar to the situation of the self-energy Σ, it is impossible to enumerate every $K^{(2)}$ diagram.

Equation (2.31), termed Bethe-Salpeter equation in the literature [33], can be regarded as the generalization of the Dyson equation (2.29) to $C^{(2)}$. Their recursive kernels, i.e. Σ and $K^{(2)}$, in fact have the following relation: each $K^{(2)}$-diagram can be generated by removing a Green's function line from a certain Σ-diagram. This procedure can be mathematically denoted as $K^{(2)} = \delta\Sigma/\delta G$. To see this relation, consider a two-particle reducible diagram as shown in Fig.2.4, where the two grey blocks represent certain arrangement of intersecting impurity lines. The two Green's functions are then connected by adding another on the right side. We thus obtain a diagram for the one-particle Green's function. This diagram is apparently non-skeleton (and hence not a self-energy diagram) since the block marked in the dashed frame can be absorbed into the Green's function. This observation implicates that diagrams generated from $\delta\Sigma/\delta G$ must be two-particle irreducible and hence belongs to $K^{(2)}$ by definition. For example, removing one of the three G-lines of the second Σ-diagram in Fig.2.5(a) respectively leads to the $K^{(2)}$-diagrams in the red dashed frame of Fig.2.5(b). In the other way around, connecting the two Green's functions in a $K^{(2)}$-diagram leads to a Σ-diagram. However, note that this procedure might map several $K^{(2)}$-diagrams to a single Σ-diagram.

The concept of diagrammatic reducibility can be generalized to diagrams containing more Green's functions. In Fig.2.6 a few reducible diagrams of higher-order $C^{(n)}$ are displayed. All of them can be split in two by cutting only two Green's function lines without touching any dashed lines. We hence define $K^{(n)}$ as the irreducible diagrams which have n edges (n G-lines). Apparently, any nth order reducible diagram can be constructed by assembling a number of $K^{(n')}(n' \leq n)$ diagrams. Moreover, akin to the relation between Σ and $K^{(2)}$, a $K^{(n)}$-diagram can be generated by removing a Green's function from certain $K^{(n-1)}$-diagram. This procedure is

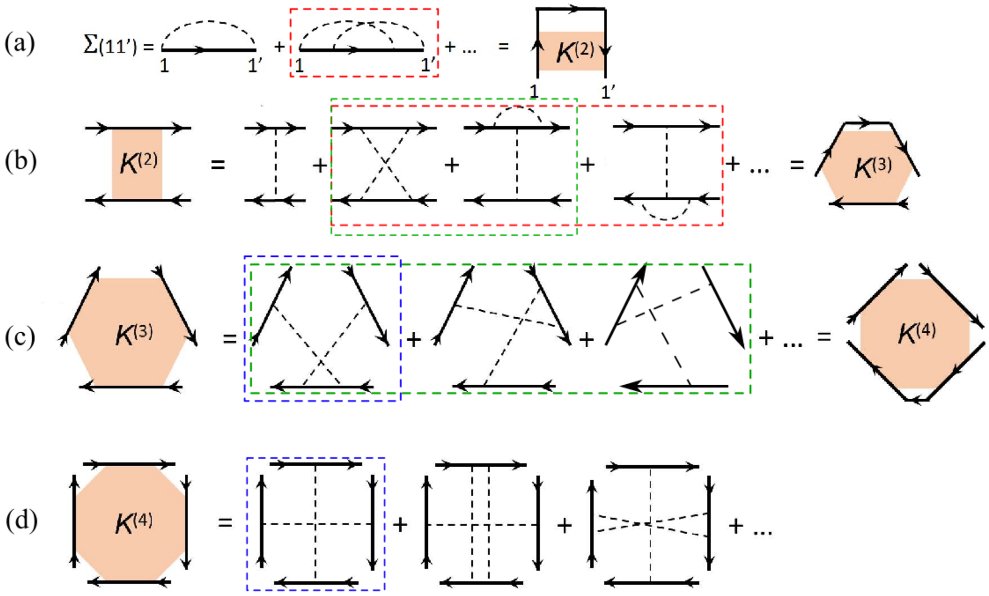

Figure 2.5: The hierarchy of irreducible $K^{(n)}$ diagrams. Diagrams enclosed in dashed frames of the same color are related via the Green's function removal procedure as described in the text. Note that the second equality in each line is only for illustration purpose and is *not* exact. For instance, all the three diagrams in the red frame would be mapped to the second Σ diagram upon linking the two solid lines, and thus that Σ diagram is triple counted.

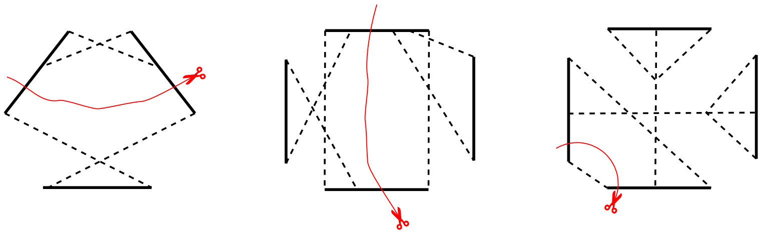

Figure 2.6: More examples of reducible diagrams, which can be split by cutting two solid lines (Green's functions) without touching dashed lines (impurity vertices).

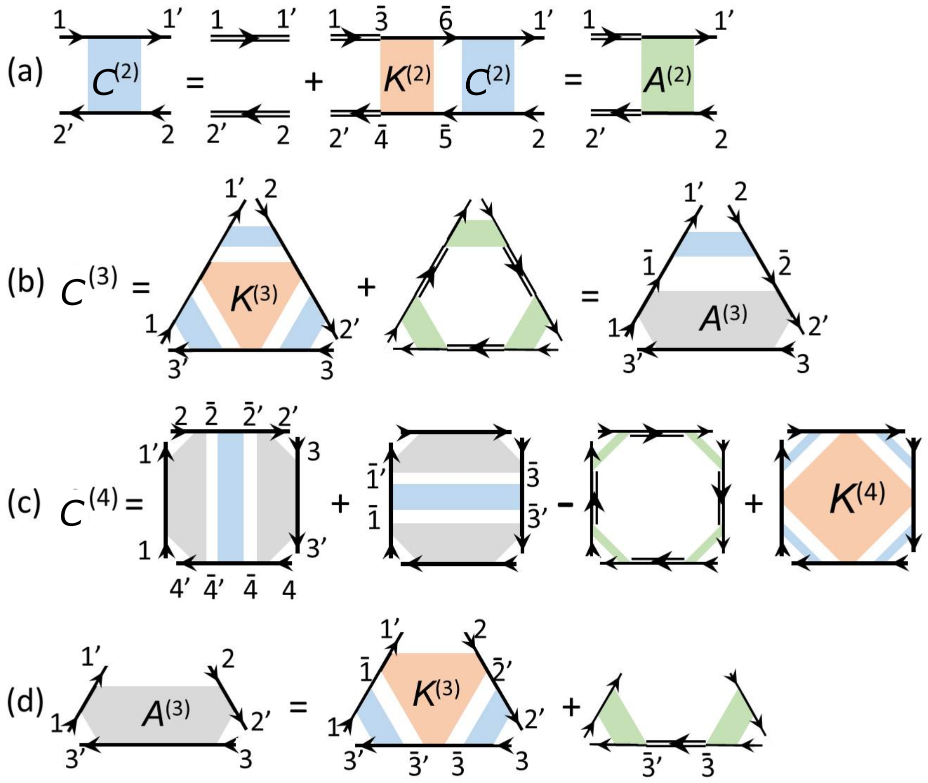

Figure 2.7: Diagrammatic schemes for disorder-averaged correlators defined by Eq.(2.30), up to $n = 4$. Same diagram blocks are marked by same colors.

illustrated in Fig.2.5. Diagrams enclosed in dashed frames of the same color are related via the Green's function removal procedure. Those in a same frame are called sibling diagrams below, in that they are derived from a same (parent) diagram.

With these understandings, we can formulate a hierarchy of diagrams that correspond to $C^{(n)}$ of different n (see Fig.2.7), which involves all $K^{(n')}$-diagrams up to $n' \leq n$. As illustrated in Fig.2.8, a $C^{(n+1)}$-diagram can be generated by replacing a G-line in a $C^{(n)}$-diagram with the $C^{(2)}$-correlator. One can easily check that applying this procedure to each $C^{(n)}$-diagram yields all the $C^{(n+1)}$-diagrams, which cover all possible connection patterns of impurity lines that are topologically different. To write down the mathematical expressions of $C^{(n)}$, we first introduce the following two auxiliary diagram blocks:

$$A^{(2)}(11'22') = \delta(11')\delta(22') + K^{(2)}(1\bar{1}\bar{2}2')C^{(2)}(\bar{1}1'2\bar{2}) \tag{2.32}$$

$$A^{(3)}(11',22',33') = A^{(2)}(\bar{3}'3'11')G(\bar{3}\bar{3}')A^{(2)}(22'3\bar{3}) + C^{(2)}(\bar{3}'3'1\bar{1})K^{(3)}(\bar{1}1',2\bar{2}',\bar{3}\bar{3}')C^{(2)}(\bar{2}'2'3\bar{3}) \tag{2.33}$$

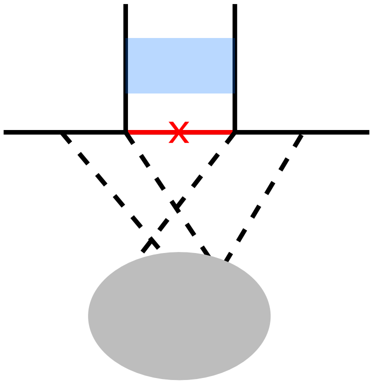

Figure 2.8: Remove a Green's function (red) from an edge of a $C^{(n)}$-diagram, and attach $C^{(2)}$ to the opening. This procedure yields a $C^{(n+1)}$-diagram.

as illustrated in Fig.2.7(a) and (d) respectively. Using $A^{(2)}$ and $A^{(3)}$ we then write down the expressions for $C^{(3)}$ and $C^{(4)}$:

$$C^{(3)}(11', 22', 33') = A^{(3)}(1\bar{1}, \bar{2}2', 33')C^{(2)}(\bar{1}1'2\bar{2}), \tag{2.34}$$

$$\begin{aligned}
C^{(4)}(11', 22', 33', 44') = {} & A^{(3)}(2\bar{2}, \bar{4}'4', 11')C^{(2)}(\bar{2}\bar{2}'\bar{4}\bar{4}')A^{(3)}(4\bar{4}, \bar{2}'2', 33') \\
& + A^{(3)}(3\bar{3}, \bar{1}'1', 22')C^{(2)}(\bar{1}\bar{1}'\bar{3}\bar{3}')A^{(3)}(1\bar{1}, \bar{3}'3', 44') \\
& - G(\bar{4}\bar{4}')A^{(2)}(\bar{4}'4'1\bar{1})G(\bar{1}\bar{1}')A^{(2)}(\bar{1}'1'2\bar{2})G(\bar{2}\bar{2}')A^{(2)}(\bar{2}'2'3\bar{3})G(\bar{3}\bar{3}')A^{(2)}(\bar{3}'3'4\bar{4}) \\
& + K^{(4)}(\bar{1}\bar{1}', \bar{2}\bar{2}', \bar{3}\bar{3}', \bar{4}\bar{4}')C^{(2)}(\bar{4}'4'1\bar{1})C^{(2)}(\bar{1}'1'2\bar{2})C^{(2)}(\bar{2}'2'3\bar{3})C^{(2)}(\bar{3}'3'4\bar{4}).
\end{aligned} \tag{2.35}$$

In principle one could continue going upward along the hierarchy, but the expressions for $C^{(n)}$ would become increasingly more complicated. Here we have only listed the expressions up to $C^{(4)}$: these should suffice for most quantum transport applications.

In practice the real difficulty of calculating $C^{(n)}$ lies in the fact that one cannot enumerate all the irreducible kernels on any level. One thus resorts to certain truncation schemes on the infinite diagram series, which leads to an approximation of $C^{(n)}$. It needs to be pointed out that such truncation schemes are not arbitrary; they need to follow certain rules. First of all, if a certain kernel is taken into account for a calculation, so should be its siblings [1]. That is to say, kernel diagrams in Fig.2.5 that are grouped in a same frame should be taken or discarded simultaneously. This rule is especially important if the computed quantity is associated with certain conservation laws [33, 49]. This point will be further discussed in Sec.2.4.2. The second rule is that, if a theoretical formalism involves $C^{(n)}$ of different n, the proper kernels used to construct $C^{(n)}$-diagrams of larger n are the descendants of those selected for lower n [1]. Thus a diagrammatic scheme is totally determined by the self-energy diagrams being selected. To illustrate this rule we consider linear transport calculations which typically involve the $C^{(2)}$-correlator. Suppose the two diagrams as presented in Fig.2.5(a) are selected for the self-energy. Then $K^{(2)}$ should accordingly consist of the four diagrams listed in Fig.2.5(b) (no more, no less). Another concrete example is the calculation of conductance fluctuation in disordered quantum dots, which can be expressed in the form of either $\langle G^{<}G^{<}\rangle$ ($C^{(2)}$) [50] or $\left\langle G^{\mathrm{R}}G^{\mathrm{A}}G^{\mathrm{R}}G^{\mathrm{A}}\right\rangle$ ($C^{(4)}$) [47]. Therefore one can use either the diagram series of Fig.2.7(a) or those in Fig.2.7(c) to compute the same quantity. It was shown in Ref.[1] that results from these two approaches would be consistent only if the approximate kernels used in the respective diagrammatic schemes are related through the second rule aforesaid.

2.3 Electron-electron interaction

In the same spirit as how impurity scattering was addressed in the last section, we also seek to calculate the e-e interaction effects using a tractable perturbation series. In this section we shall first present the theory of Hedin equations [51] which serves to systematically generate the diagrammatic series to an arbitrary order with respect to the interaction strength. We will also demonstrate how to compute the diagrams by means of the real-time Green's functions introduced in Sec.2.1.2.

2.3.1 Hedin equations

The starting point is again the equation of motion Eq.(2.10). Note that, in the presence of electron-electron interaction, Eq.(2.10) is not a closed equation for the one-particle Green's function G in that $G^{(2)}$ is also involved. The latter can be expressed on a formal level with only one-particle quantities by employing the functional derivative technique [49, 52]. To be specific, we take derivative of the Green's function with respect to the external potential v, which only couples to the electron density in the Hamiltonian. Using the definition (2.7) and the identity $\frac{\delta}{\delta v(1)}T_C\left\{e^{-\mathrm{i}\int_C d\tau' H(\tau')}\cdots\right\} = -\mathrm{i}T_C\left\{e^{-\mathrm{i}\int_C d\tau' H(\tau')}n(1)\cdots\right\}$, we get

$$G^{(2)}(1,3;2,3^{+}) = G(1,2)G(3,3^{+}) - \frac{\delta G(1,2)}{\delta v(3)}, \tag{2.36}$$

which is then used to replace the $G^{(2)}$ in Eq.(2.10). To further simplify Eq.(2.10) we introduce the interaction self-energy:

$$\Sigma_{\mathrm{ee}}(1,2) = \mathrm{i}\int d3d4\; U(1,3)\frac{\delta G(1,4)}{\delta v(3)}G^{-1}(4,2), \tag{2.37}$$

where G^{-1} should be understood as an operator such that $GG^{-1} = 1$, or more explicitly

$$\int d3\; G(1,3)G^{-1}(3,2) = \delta(1,2). \tag{2.38}$$

Using Eqs.(2.36) and (2.37), we then rewrite Eq.(2.10) as

$$\begin{aligned}\mathrm{i}\frac{d}{d\tau_1}G(\mathbf{r}_1\tau_1,\mathbf{r}_2\tau_2) &= \delta(\mathbf{r}_1-\mathbf{r}_2)\delta(\tau_1-\tau_2)+\int d\mathbf{r}' H_0(\mathbf{r}_1,\mathbf{r}',\tau_1)G(\mathbf{r}'\tau_1,\mathbf{r}_2\tau_2)\\ &+[V_{\mathrm{H}}+v](\mathbf{r}_1\tau_1)G(\mathbf{r}_1\tau_1,\mathbf{r}_2\tau_2)+\int d\tau' d\mathbf{r}'\Sigma_{\mathrm{ee}}(\mathbf{r}_1\tau_1,\mathbf{r}'\tau')G(\mathbf{r}'\tau',\mathbf{r}_2\tau_2),\end{aligned} \tag{2.39}$$

where the Hartree potential $V_{\mathrm{H}}(1)\equiv -\mathrm{i}\int d3\, U(1,3)G(3,3^+)$. To proceed we utilize Eq.(2.38) and replace the derivative in Eq.(2.37) with

$$\frac{\delta G(1,2)}{\delta v(3)} = -\int d5d4\, G(1,4)\frac{\delta G^{-1}(4,5)}{\delta v(3)}G(5,2). \tag{2.40}$$

Then, by using the chain rule, we get

$$\begin{aligned}\Sigma_{\mathrm{ee}}(1,2) &= -\mathrm{i}\int d3d4\, U(1,3)G(1,4)\frac{\delta G^{-1}(4,2)}{\delta v(3)} \qquad (2.41)\\ &= -\mathrm{i}\int d3d4d5\, U(1,3)G(1,4)\frac{\delta G^{-1}(4,2)}{\delta\tilde{V}(5)}\frac{\delta\tilde{V}(5)}{\delta v(3)} = \mathrm{i}\int d4d5\, W(1,5)G(1,4)\frac{-\delta G^{-1}(4,2)}{\delta\tilde{V}(5)},\end{aligned}$$

where $\tilde{V}=V_{\mathrm{H}}+v$ and

$$W(1,2)=\int d3U(1,3)\frac{\delta\tilde{V}(2)}{\delta v(3)}. \tag{2.42}$$

The quantity $\delta\tilde{V}/\delta v$ represents the total potential change in response to the external potential, and thus it equals the inverse dielectric function ε^{-1} of the system. In this sense, W represents an effective two-body interaction which takes into account the dielectric environment comprised of surrounding electrons. This effective interaction can be further expressed in a recursive form if we continue to unfold $\delta\tilde{V}/\delta v$:

$$\begin{aligned}W(1,2) &= \int d3\, U(1,3)\left[\delta(2,3)+\frac{\delta V_{\mathrm{H}}(2)}{\delta v(3)}\right]\\ &= U(1,2)+\int d3\, U(1,3)\left[\int d4d5\frac{\delta n(4)}{\delta\tilde{V}(5)}\frac{\delta\tilde{V}(5)}{\delta v(3)}U(4,2)\right]\\ &= U(1,2)+\int d4d5\, W(1,5)P(5,4)U(4,2),\end{aligned} \tag{2.43}$$

where

$$P(1,2)=\frac{\delta n(1)}{\delta\tilde{V}(2)} = -\mathrm{i}\frac{\delta G(1,1^+)}{\delta\tilde{V}(5)} = \mathrm{i}\int d3d4\, G(1,3)\frac{\delta G^{-1}(3,4)}{\delta\tilde{V}(2)}G(4,1^+) \tag{2.44}$$

is the polarization. The quantity $-\delta G^{-1}/\delta\tilde{V}$, which shows up in both Eq.(2.41) and (2.44), is termed the vertex function, denoted as Λ_{ee} in the following. Using Eq.(2.39) we can express Λ_{ee} as

$$\Lambda_{\mathrm{ee}} = -\frac{\delta G^{-1}(1,2)}{\delta\tilde{V}(3)} = \delta(1,2)\delta(1,3)+\frac{\delta\Sigma_{\mathrm{ee}}(1,2)}{\delta\tilde{V}(3)}. \tag{2.45}$$

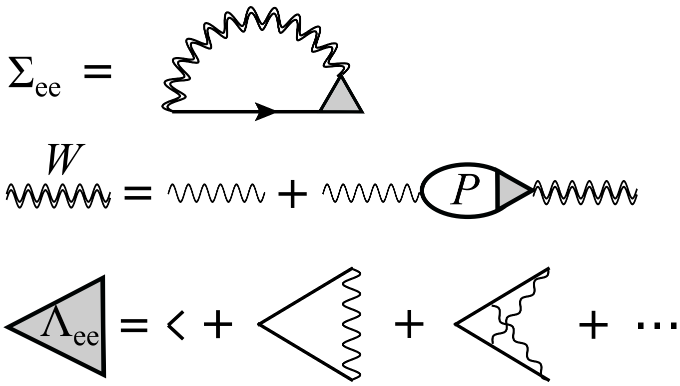

Figure 2.9: Diagrammatic form of the Hedin equations (see the main text). Solid lines represent Green's functions and single wiggle lines represent the bare e-e interaction.

By further using the chain rule $\delta\Sigma_{\rm ee}/\delta\tilde{V} = (\delta\Sigma_{\rm ee}/\delta G)(\delta G/\delta\tilde{V})$ and Eq.(2.40), we get a recursive relation (the Bethe-Salpeter equation) for $\Lambda_{\rm ee}$:

$$\Lambda_{\rm ee}(1,2,3) = \delta(1,2)\delta(1,3) + \int d4d5d6d7\, \frac{\delta\Sigma_{\rm ee}(1,2)}{\delta G(4,5)} G(4,6)G(7,5)\Lambda_{\rm ee}(6,7,3). \tag{2.46}$$

Equations (2.41), (2.43), (2.44), and (2.46) as a whole are termed the self-consistent Hedin equations in the literature [51]. Their diagrammatic representation is shown in Fig.2.9. Although every object in these equations is essentially a functional of the Green's function, this formally exact equation system cannot be solved in a closed form. The reason is that the functional form of $\Sigma_{\rm ee}[G]$, which lies in the heart of Eq.(2.46), cannot be known *a priori*, and in fact the functional itself is to be determined by the outcome (if ever accessible) of the Hedin equations. Naively one might think of using a numerical approach to solve the Hedin equations iteratively. However, this is again impractical because the terms generated by the iteration would grow rapidly in amount and soon be out of control. Even worse is that the generated series is not guaranteed to have a convergent behavior [53]. Therefore, in practical applications of the Hedin equations, one often truncates the $\Lambda_{\rm ee}$ series by hand or selectively sums up its subset using certain advanced techniques (e.g. Parquet scheme [54])

2.3.2 Diagrammatic formalism

Figure 2.10 displays the self-energy series expanded from the Hedin equations with respect to the bare e-e interaction, sorted by the number of interaction lines. Figure 2.10(a) and (b) correspond to the Hartree-Fock approximation [33], (c) comes from expanding the screened potential W, and (d),(e) both arise from the vertex correction. The rules to translate these diagrams into mathematical expressions can be easily deduced from the Hedin equations: Each solid line represents G, a

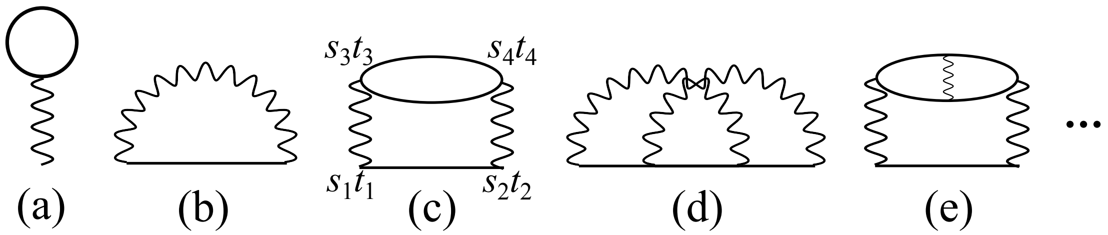

Figure 2.10: Perturbation series of the self-energy ($\Sigma_{\rm ee}$) generated from the Hedin equations (cf. Fig.2.9).

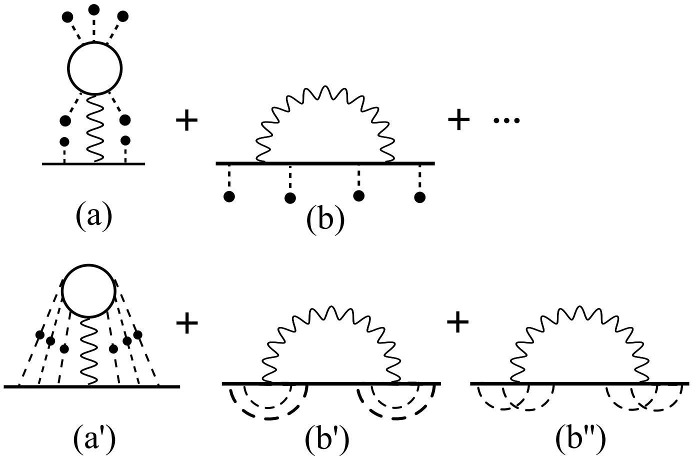

Figure 2.11: Self-energy diagrams in the presence of both interaction and impurity scattering. Those in the second row are obtained after disorder-average. Note that, due to different combinations of the impurity lines, after disorder-average there could exist multiple diagrams having the same structure on the interaction part, e.g. (b') and (b").

wiggle line represents $\mathrm{i}U$, and each closed G-loop [e.g. in Fig.2.10(a,c,e)] yields a factor of -1 [33].

In the situation where the physical system is subject to both interaction and impurity scattering, we need to combine the diagrammatic scheme for disorder-average with that of Fig.2.10. To this end, we regard the external potential $v(\mathbf{r})$ as a perturbation and thus expand the Green's function with respect to it. This adds new diagrammatic elements on top of Fig.2.10, as illustrated in Fig.2.11 (first row). Disorder-average amounts to contracting the impurity lines by their cumulants, just as demonstrated in Sec.2.2.1. Diagrams yielded from this procedure are illustrated in the second row of Fig.2.11. In particular, we will see in Chapter 5 that Figs.2.11(a',b') play an important role in the so-called Altshuler-Aronov effects [21].

A diagram is computed by integrating over all internal variables. Special attention should be paid to the time variables as they lie on the Keldysh contour, where the two branches have opposite integration directions. To alleviate the inconvenience that the time variables run on opposite branches, we utilize the matrix representation Eq.(2.16) and assign a branch index $s(-/+)$ together with a *real*-time variable to each diagrammatic vertex (see Fig.2.10c). As such the integration direction can now be tracked by the sign of s. Accordingly, the interaction line now reads -isU and the impurity line (before contraction) reads $-sv$ in this representation. Cautions should be taken in that one cannot draw a direct correspondence from the thus computed diagrams to the self-energy under the contour representation ($\overset{\supset}{\mathbf{\Sigma}}$). To see this we consider a self-energy diagram attached to two external Green's functions. Such a diagram is supposed to give $\overset{\supset}{\mathbf{G}}\,\sigma_z\,\overset{\supset}{\mathbf{\Sigma}}\,\sigma_z\,\overset{\supset}{\mathbf{G}}$ according to Eq.(2.22). However, the σ_z matrices at the two terminals of the self-energy diagram are not included in the diagrammatic rule formulated above. Therefore the diagram being computed actually corresponds to

$$\Sigma^{ss'} = \sigma_z\,\overset{\supset}{\mathbf{\Sigma}}\,\sigma_z = \begin{bmatrix} \Sigma^{\mathrm{R}} + \Sigma^{<} & -\Sigma^{<} \\ -\Sigma^{>} & \Sigma^{>} - \Sigma^{\mathrm{R}} \end{bmatrix} \tag{2.47}$$

For the similar reason the wiggle line represents

$$W^{ss'} = \sigma_z \begin{bmatrix} W^{\mathrm{R}} + W^{<} & W^{<} \\ W^{>} & W^{>} - W^{\mathrm{R}} \end{bmatrix} \sigma_z = \begin{bmatrix} W^{\mathrm{R}} + W^{<} & -W^{<} \\ -W^{>} & W^{>} - W^{\mathrm{R}} \end{bmatrix} \tag{2.48}$$

which bears the same form as Eq.(2.47). In practice it is more convenient to compute $W^{\mathrm{R},<,>}$, since Eq.(2.43) consists of only convolutional integrals of the form Eq.(2.21), and then transform to Eq.(2.48) for further calculations.

To be concrete, a calculation example on Fig.2.10(c) is given in the following. This diagram is evaluated as (without showing the spatial variables explicitly):

$$\begin{aligned} &\sum_{s_3,s_4} \int dt_3 dt_4 \left[-\mathrm{i}s_1 U(s_1t_1, s_3t_3)\delta(s_1, s_3)\delta(t_1 - t_3)\right] \left[-\mathrm{i}s_2 U(s_2t_2, s_4t_4)\delta(s_2, s_4)\delta(t_4 - t_2)\right] \\ &\times G(s_1t_1, s_2t_2)\left[-2G(s_3t_3, s_4t_4)G(s_4t_4, s_3t_3)\right], \end{aligned} \tag{2.49}$$

where the factor 2 comes from the spin degeneracy. As an example, we show the derivation of its lesser component $\Sigma^{<}_{(c)}$ from the above expression. To this end we set $s_1 = -$, $s_2 = +$ and take into account the minus sign as indicated in Eq.(2.47) (top right corner). This leads to

$$\Sigma^{<}_{(c)}(\mathbf{r}_1t_1, \mathbf{r}_2t_2) = 2\int d\mathbf{r}_3 d\mathbf{r}_4 U(\mathbf{r}_1 - \mathbf{r}_3)U(\mathbf{r}_2 - \mathbf{r}_4)G^{<}(\mathbf{r}_1t_1, \mathbf{r}_2t_2)G^{<}(\mathbf{r}_3t_1, \mathbf{r}_4t_2)G^{>}(\mathbf{r}_4t_2, \mathbf{r}_3t_1), \tag{2.50}$$

which agrees with the expression derived from the Langreth rules [55]. The reason why we bother reformulating the diagrams with the s indices instead of using the Langreth rules [33, 44] directly is that the former approach turns out more feasible for numerical programming, especially for complex diagrams such as Figs.2.11(a',b').

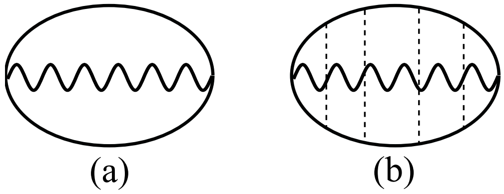

Figure 2.12: A first-order diagram of Luttinger-Ward functional ($\Phi[G]$) with (a) only e-e interaction, (b) coexistence of disorder-average.

2.4 Conserving approximation

As can be seen from previous sections, the accuracy of a diagrammatic scheme, either for the disorder-average problem or for the e-e interaction, largely depends on the selection of self-energy diagrams. On the one hand, the selected Σ-diagrams should at least incorporates the concerned physical process, which varies among different systems and problems. On the other hand, as a general rule, quantities computed in an approximate approach should yet satisfy certain exact relations on a fundamental level. For quantum transport problems it is most important that the computed currents or coefficients fulfil the conservation laws [32, 33]. In this section we present the Kadanoff-Baym scheme [49, 52] which offers a tractable approach to generating sets of Σ-diagrams such that the computed transport currents at the one-particle level are guaranteed to be continuous. We also formulate a set of Ward identities to be used to check the conserving property of general n-particle correlators [see Eq.(2.30)], which are closely related to transport coefficients not addressed within the Kadanoff-Baym theory.

2.4.1 Kadanoff-Baym scheme

The Kadanoff-Baym scheme starts by constructing the Luttinger-Ward functional [33] which is often denoted as $\Phi[G]$. In its diagrammatic visualization (see Fig.2.12) $\Phi[G]$ consists of closed Green's function loops with connections of interaction vertices. Whereas the original paper by Baym and Kadanoff [49] only considered the e-e interaction effect, their theory can be readily generalized to the coexistence of disorder-average [34] (e.g. Fig.2.12b). Having specified a set of Φ-diagrams, one then derives the self-energy by individually removing G-lines from each Φ-diagram in the set. For example, the diagram of Fig.2.11(b') is generated from Fig.2.12(b). This process is much similar to how the disorder-average kernels are derived from the self-energy (see Sec.2.2.2). In mathematical form it can be expressed as

$$\Sigma(1,2) = \frac{\delta\Phi[G]}{\delta G(2,1^{+})}. \tag{2.51}$$

To see this scheme indeed lead to the conservation of charge current, we start with a reformulation of the equation of motion (2.39). In Eq.(2.39) we notice that the time derivative is applied to the first time argument τ_1. Alternatively, it can be applied to τ_2 as well, and as such one obtains an equivalent pair of equations of motion:

$$\mathrm{i}\frac{d}{d\tau_1}G(1,2) - \int d3\ [H_0(1,3) + \Sigma(1,3)]G(3,2) = \delta(1,2), \tag{2.52a}$$

$$-\mathrm{i}\frac{d}{d\tau_2}G(1,2) - \int d3\ G(1,3)[H_0(3,2) + \Sigma(3,2)] = \delta(1,2). \tag{2.52b}$$

Note that the equations of motion must be understood as self-consistent equations for G in that Σ is implicitly a functional of G. Subtracting Eq.(2.52b) from Eq.(2.52a) and utilizing the definition of H_0 [see Eq.(2.2)], one gets

$$\begin{aligned}&\left[\mathrm{i}\frac{d}{d\tau_1} + \mathrm{i}\frac{d}{d\tau_2}\right] G(1,2) + (\nabla_1 + \nabla_2)\cdot\frac{\nabla_1 - \nabla_2}{2m}G(1,2) - \frac{\mathrm{i}q}{2mc}[\nabla_1\cdot\mathbf{A}(1)\\ &+ \nabla_2\cdot\mathbf{A}(2) + 2\mathbf{A}(1)\cdot\nabla_1 + 2\mathbf{A}(2)\cdot\nabla_2]G(1,2) - \frac{q^2}{2mc^2}[A(1)^2 - A(2)^2]G(1,2)\\ &= \int d3\ [\Sigma(1,3)G(3,2) - G(1,3)\Sigma(3,2)].\end{aligned} \tag{2.53}$$

Setting $\mathbf{r}_2\tau_2 \to \mathbf{r}_1{\tau_1}^+$ and making use of the relation (2.8), one can rewrite the left hand side as

$$-\frac{dn(1)}{d\tau_1} + \nabla_1\cdot\left[\left(\frac{\nabla_1 - \nabla_2}{2m}G(1,2)\right)_{2=1^+} - \frac{\mathrm{i}q}{mc}\mathbf{A}(1)G(1,1^+)\right] = -\frac{dn(\mathbf{r}_1t_1)}{dt_1} - \nabla_{\mathbf{r}_1}\cdot\mathbf{j}(\mathbf{r}_1t_1). \tag{2.54}$$

Hence one gets a sufficient condition for the particle number to conserve:

$$\int d2\ [\Sigma(1,2)G(2,1^+) - G(1,2)\Sigma(2,1^+)] = 0. \tag{2.55}$$

In the Kadanoff-Baym scheme, this condition is automatically satisfied. This can be seen by performing a gauge transformation $G(1,2) \to e^{\mathrm{i}\phi(1)}G(1,2)e^{-\mathrm{i}\phi(2)}$. Since the Green's functions in a Φ-diagram form closed loops, the Φ-functional is invariant under this gauge transformation. Taking ϕ infinitesimal, one gets

$$\begin{aligned}0 = \delta\Phi[G] &= \mathrm{i}\int d1d2\ \Sigma(1,2)G(2,1^+)[\phi(2) - \phi(1)]\\ &= -\mathrm{i}\int d1d2\ [\Sigma(1,2)G(2,1^+) - G(1,2)\Sigma(2,1^+)]\phi(1)\end{aligned} \tag{2.56}$$

Finally, because of the arbitrary choice of ϕ, Eq.(2.55) must hold. In fact, the Kadanoff-Baym scheme also ensures the continuity of other quantities, such as momentum, angular momentum, and energy. For a comprehensive discussion on this topic, the reader is referred to Ref.[33].

2.4.2 Ward identity

Whereas the Kadanoff-Baym theory concerns the conservation properties of direct observables that are encoded in the one-particle Green's function, some quantities measured in experiments, such as response functions, are rather associated with higher-order Green's functions and are thus subject to more sophisticated conservation criteria other than the Φ-functional derivablility. A common method to check whether conservation laws are respected in calculations of response functions consists in using the Ward identity. As a relation between different correlation functions the Ward identity was originally formulated in the context of quantum electrodynamics [56]. Akin to Eq.(2.55), the Ward identity can also be derived from the gauge invariance of the underlying quantum field [56]; thus it implicates conservation laws. The machinery of this theory was later transferred to the condensed matter physics, with several variations depending on the physical problems [32]. In the following, we restrict ourselves to the disorder-average problem of noninteracting systems. We shall show that the formalism developed in Sec.2.2.2 for Green's function products satisfies a particular type of Ward identity and thus meets conservation requirements.

To formulate the Ward identity we first define a function

$$\Upsilon(\mathbf{r}_1, \mathbf{r}_2; z_1, z_2) \equiv [G_0(\mathbf{r}_1, \mathbf{r}_2; z_2)]^{-1} - [G_0(\mathbf{r}_1, \mathbf{r}_2; z_1)]^{-1}, \tag{2.57}$$

where G_0 is the Matsubara Green's function [32] of the disorder-free medium (assuming a steady state): the analytic continuation of $z \to \omega \pm \mathrm{i}0^+$ leads to $G_0^{\mathrm{R}}(\omega)$ and $G_0^{\mathrm{A}}(\omega)$ respectively. It is easy to see that for a closed system $\Upsilon(z_1, z_2)$ simply reduces to $(z_2 - z_1)\delta(\mathbf{r}_1 - \mathbf{r}_2)$. However, for systems subject to open boundary conditions (e.g. connected to electrodes), $\Upsilon(z_1, z_2) = z_2 - z_1 + \Sigma_{\text{lead}}(z_1) - \Sigma_{\text{lead}}(z_2)$ where Σ_{lead} is the lead self-energy (see below in Sec.2.5.2). Assuming the impurity scattering is elastic, $\Upsilon(z_1, z_2)$ also equals to $G_v(z_2) - G_v(z_1)$ where G_v is the Green's function under a given disorder configuration. Thus Eq.(2.57) can be rearranged as

$$G_v(z_1)\Upsilon(z_1, z_2)G_v(z_2) = G_v(z_1) - G_v(z_2). \tag{2.58}$$

One is then free to continue multiplying G_v on both sides of Eq.(2.58), and after taking disorder-average over v and invoking the definition Eq.(2.30), one arrives at a Ward identity:[4]

$$\begin{aligned}
&\int d\mathbf{r}_m{}' d\mathbf{r}_{m+1} C^{(n)}(\mathbf{r}_1, \mathbf{r}_1{}', z_1;\ \mathbf{r}_2, \mathbf{r}_2{}', z_2 \cdots \mathbf{r}_n, \mathbf{r}_n{}', z_n)\Upsilon(\mathbf{r}_m{}', \mathbf{r}_{m+1}; z_m, z_{m+1}) \\
&= C^{(n-1)}(\cdots \mathbf{r}_{m-1}, \mathbf{r}_{m-1}{}', z_{m-1};\ \mathbf{r}_m, \mathbf{r}_{m+1}{}', z_m;\ \mathbf{r}_{m+2}, \mathbf{r}_{m+2}{}', z_{m+2} \cdots) \\
&- C^{(n-1)}(\cdots \mathbf{r}_{m-1}, \mathbf{r}_{m-1}{}', z_{m-1};\ \mathbf{r}_m, \mathbf{r}_{m+1}{}', z_{m+1};\ \mathbf{r}_{m+2}, \mathbf{r}_{m+2}{}', z_{m+2} \cdots).
\end{aligned} \tag{2.59}$$

---

[4] This identity under $n = 2, 3$ has been previously discussed in Refs.[46, 57] in the context of the coherent potential approximation.

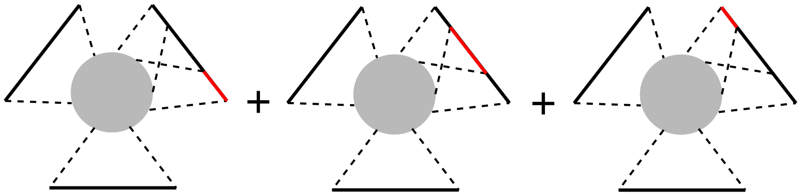

Figure 2.13: Illustration for Eq.(2.60) .

Notice that on the right hand side the two $C^{(n-1)}$ differ only by one z-argument. This identity needs be satisfied no matter what approximation scheme is used. A similar relation holds for the irreducible kernels:

$$\begin{aligned}&\int d\mathbf{r}_m{}'d\mathbf{r}_{m+1}K^{(n)}(\mathbf{r}_1,\mathbf{r}_1{}',z_1;\ \mathbf{r}_2,\mathbf{r}_2{}',z_2\cdots\mathbf{r}_n,\mathbf{r}_n{}',z_n)\left[G(\mathbf{r}_m{}',\mathbf{r}_{m+1};z_m)-G(\mathbf{r}_m{}',\mathbf{r}_{m+1};z_{m+1})\right]\\&=K^{(n-1)}(\cdots\mathbf{r}_{m-1},\mathbf{r}_{m-1}{}',z_{m-1};\ \mathbf{r}_m,\mathbf{r}_{m+1}{}',z_m;\ \mathbf{r}_{m+2},\mathbf{r}_{m+2}{}',z_{m+2}\cdots)\\&-K^{(n-1)}(\cdots\mathbf{r}_{m-1},\mathbf{r}_{m-1}{}',z_{m-1};\ \mathbf{r}_m,\mathbf{r}_{m+1}{}',z_{m+1};\ \mathbf{r}_{m+2},\mathbf{r}_{m+2}{}',z_{m+2}\cdots).\end{aligned}\tag{2.60}$$

This relation follows from the fact that $K^{(n)}$ can be generated by removing a Green's function from $K^{(n-1)}$. More clearly, we visualize the right-hand side of Eq.(2.60) by Fig.2.13, where a $K^{(3)}$-diagram is used for illustration. The red line represents $[G(\mathbf{r}_m{}',\mathbf{r}_{m+1};z_m)-G(\mathbf{r}_m{}',\mathbf{r}_{m+1};z_{m+1})]$; its migration from one end of the m-th edge to the other end follows from the identity

$$\begin{aligned}X_1X_2\cdots X_n-Y_1Y_2\cdots Y_n&=[(X_1-Y_1)Y_2\cdots Y_n]+[X_1(X_2-Y_2)Y_3\cdots Y_n]\\&+\cdots+[X_1X_2\cdots(X_n-Y_n)]\,.\end{aligned}\tag{2.61}$$

We notice that, once these red lines are removed respectively, one gets the corresponding $K^{(n=4)}$-diagrams. Hence Eq.(2.60) is proved.

The same logic can as well apply to Eq.(2.59) since a $C^{(n)}$-diagram can be obtained by replacing a Green's function in $C^{(n-1)}$ with $C^{(2)}$ (see Fig.2.8). Therefore it only remains to show

$$\int d\mathbf{r}_1{}'d\mathbf{r}_2C^{(2)}(\mathbf{r}_1,\mathbf{r}_1{}',z_1;\ \mathbf{r}_2,\mathbf{r}_2{}',z_2)\Upsilon(\mathbf{r}_1{}',\mathbf{r}_2;z_1,z_2)=G(\mathbf{r}_1,\mathbf{r}_2{}',z_1)-G(\mathbf{r}_1,\mathbf{r}_2{}',z_2),\tag{2.62}$$

i.e. the Ward identity for $n=2$, in order to verify that any approximation constructed with the scheme of Fig.2.5 indeed satisfies the identity (2.59) for all n. To this end, we start by rewriting the left hand side of Eq.(2.62) as

$$\int d\mathbf{r}_1{}'d\mathbf{r}_2G(\mathbf{r}_1,\mathbf{r}_1{}',z_1)\left[\Upsilon(\mathbf{r}_1{}',\mathbf{r}_2;z_1,z_2)+\Lambda(\mathbf{r}_1{}',\mathbf{r}_2;z_1,z_2)\right]G(\mathbf{r}_2,\mathbf{r}_2{}',z_2).\tag{2.63}$$

Using the recursive structure of Eq.(2.31), we obtain an equation for the Λ object defined in (2.63):

$$\Lambda(\mathbf{r}_0,\mathbf{r}_0{}';z_1,z_2)=\int d\mathbf{r}_1d\mathbf{r}_2{}'K^{(2)}(\mathbf{r}_0,\mathbf{r}_1,z_1;\ \mathbf{r}_2{}',\mathbf{r}_0{}',z_2)\int d\mathbf{r}_1{}'d\mathbf{r}_2G(\mathbf{r}_1,\mathbf{r}_1{}',z_1)$$

$$\times \left[\Upsilon(\mathbf{r}_1{}', \mathbf{r}_2; z_1, z_2) + \Lambda(\mathbf{r}_1{}', \mathbf{r}_2; z_1, z_2)\right] G(\mathbf{r}_2, \mathbf{r}_2{}', z_2). \tag{2.64}$$

Since $G^{-1} = G_0^{-1} - \Sigma$ (Σ being the self-energy from disorder-average), we replace the Υ in Eq.(2.64) by $G^{-1}(z_2) - G^{-1}(z_1) + \Sigma(z_2) - \Sigma(z_1)$. Then, making use of Eq.(2.60) at $n = 2$ (noticing $K^{(1)} \equiv \Sigma$), we obtain from Eq.(2.64): $\Lambda(z_1, z_2) = \Sigma(z_1) - \Sigma(z_2)$. Finally, expressing the Υ and Λ in (2.63) with G and Σ, we find that (2.63) yields $G(z_1) - G(z_2)$, which is the right hand side of Eq.(2.62). Hence Eq.(2.62) is proved, along with Eq.(2.59) for all n.

In the following we use the linear-response polarization P^{R} [see Eq.(2.44)] as an example to illustrate how the Ward identity is related with charge conservation. Given a disorder configuration v and in the absence of e-e interaction, the polarization is written as

$$\begin{aligned} P^{\mathrm{R}}(\mathbf{r}, \mathbf{r}', \omega) = \int \frac{d\varepsilon}{2\pi \mathrm{i}} &[f(\varepsilon) - f(\varepsilon+\omega)] G_v^{\mathrm{A}}(\mathbf{r}', \mathbf{r}, \varepsilon) G_v^{\mathrm{R}}(\mathbf{r}, \mathbf{r}', \varepsilon+\omega) \\ &+ f(\varepsilon+\omega) G_v^{\mathrm{A}}(\mathbf{r}', \mathbf{r}, \varepsilon) G_v^{\mathrm{A}}(\mathbf{r}, \mathbf{r}', \varepsilon+\omega) - f(\varepsilon) G_v^{\mathrm{R}}(\mathbf{r}', \mathbf{r}, \varepsilon) G_v^{\mathrm{R}}(\mathbf{r}, \mathbf{r}', \varepsilon+\omega), \end{aligned} \tag{2.65}$$

where we have made use of the equilibrium relation $G^{<}(\varepsilon) = f(\varepsilon)[G^{\mathrm{A}}(\varepsilon) - G^{\mathrm{R}}(\varepsilon)]$. Integrating $\mathbf{r}$ over the *whole* space and applying Eq.(2.58) with $\Upsilon = z_2 - z_1$, we find $\int d\mathbf{r} P^{\mathrm{R}}(\mathbf{r}, \mathbf{r}', \omega) = 0$. This indicates that the total density variation in response to an arbitrary perturbation of external field should always be zero, thereby complying with the charge conservation law. Apparently applying disorder-average to Eq.(2.65) should preserve this conservation property; this is guaranteed by the identity Eq.(2.62). Applications of higher-order Ward identities are less common but do exist in some cases: they are related with some nonlinear-response coefficients [46] or cross-device fluctuations [47].

2.5 Transport model

This section demonstrates the implementation of the Green's function framework on finite transport systems which exchange particles and energy with the environment. The overall goal is to use the Green's functions to compute the charge current in such systems given the steady status of their environment.

2.5.1 System partition

A theoretical model for calculating transport properties needs to respect the fact that electronic transport is a physical process which depends both on the sample size and on the time scale of experimental measurements. In this thesis we consider ergodic transport systems in the sense that a particle injected into the sample (or device) will traverse its entire space during the time period of

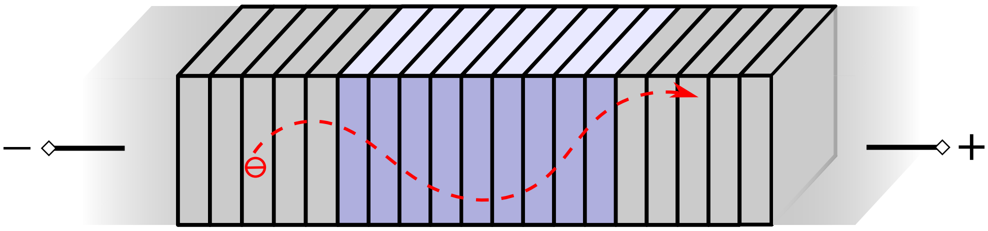

Figure 2.14: Schematic of the transport model. The simulation box is divided into three regions: left lead, device, and right lead. The mesoscopic structure of interest is placed in the device region, and the leads are assumed to have certain periodic structures that extend to infinity. The chemical potential and temperature in leads are given by the respective electrodes to which they are connected. The system is further sliced into "principal layers" such that the underlying non-interacting Hamiltonian does not couple nonadjacent layers.

measurement and fully explore its boundaries. This is a valid assumption since the systems to be studied are assumed to be mesoscopic and at a steady state (corresponding to long time periods). In this scenario, it is thus necessary to include in the model not only the device itself but also a careful treatment of its environment. A common practice is to put in the simulation box the device structure of interest together with the metallic leads connected at the two ends (see Fig.2.14) [40]. The leads are assumed to have a strict periodic structure that extends to infinity. As the leads are eventually linked with the respective electrodes, they are set at equilibrium with given chemical potentials and temperatures, and hence serve as electronic reservoirs for the device. Furthermore, electrons in the leads are assumed to form a Fermi liquid such that the electronic structure therein can be described by a quadratic Hamiltonian. For practical reasons the system is also sliced into "principal layers" stacked along the transport direction such that the underlying non-interacting Hamiltonian does not couple nonadjacent layers [58].

Under these considerations, the total Hamiltonian hence takes the following form in real-space:

$$\begin{bmatrix} H_{\mathrm{LL}} & H_{\mathrm{LD}} & 0 \\ H_{\mathrm{DL}} & H_{\mathrm{DD}} & H_{\mathrm{DR}} \\ 0 & H_{\mathrm{RD}} & H_{\mathrm{RR}} \end{bmatrix}$$

where the subscripts L/D/R denote left/device/right respectively. Note that the off-diagonal blocks have zero entries except at the lead-device contacts, and that both H_{LL} and H_{RR} have a tridiagonal form

$$H_{\mathrm{LL}} = \begin{bmatrix} \ddots & \ddots & & \\ \ddots & H_{00} & H_{01} & \\ & H_{10} & H_{00} & H_{01} \\ & & H_{10} & H_{00} \end{bmatrix}, \quad H_{\mathrm{RR}} = \begin{bmatrix} H_{00} & H_{01} & & \\ H_{10} & H_{00} & H_{01} & \\ & H_{10} & H_{00} & \ddots \\ & & \ddots & \ddots \end{bmatrix}$$

due to the principal layer scheme.

2.5.2 Block Green's functions

Similar to the Hamiltonian, the Green's function can also be viewed as a block matrix in the real-space:

$$G = \begin{bmatrix} G_{\mathrm{LL}} & G_{\mathrm{LD}} & G_{\mathrm{LR}} \\ G_{\mathrm{DL}} & G_{\mathrm{DD}} & G_{\mathrm{DR}} \\ G_{\mathrm{RL}} & G_{\mathrm{RD}} & G_{\mathrm{RR}} \end{bmatrix}$$

As will be clear later, the central quantities in a quantum transport problem are the block Green's functions G_{LD}, G_{RD}, and G_{DD}: G_{LD} and G_{RD} turn out to be associated with the currents through the leads, and G_{DD} contains the statistical information about the device region of our interest. In this subsection, we follow the equation of motion technique [44] to obtain the compact expressions of these Green's functions.

We first seek to write down the equation of motion for G_{LD}. To this end, we utilize Eq.(2.39) with the restriction that the spatial coordinate $\mathbf{r}_1$ is placed in the left lead and $\mathbf{r}_2$ in the device region. After some straightforward algebra on the matrix product $H_0 G$, we get[5]

$$\mathrm{i}\frac{d}{d\tau_1} G_{\mathrm{LD}}(1,2) = \int d3 \left[H_{\mathrm{LL}}(1,3) G_{\mathrm{LD}}(3,2) + H_{\mathrm{LD}}(1,3) G_{\mathrm{DD}}(3,2) \right]. \tag{2.66}$$

Note that, in writing down this equation, we have invoked the presumption that the leads are free of disorder or interaction. To solve this equation of motion, we use again the strategy which was employed as in Eq.(2.25): namely we express G_{LD} as

$$G_{\mathrm{LD}}(1,2) = \int d3 d4 G_{0\mathrm{LL}}(1,3) H_{\mathrm{LD}}(3,4) G_{\mathrm{DD}}(4,2), \tag{2.67}$$

where $G_{0\mathrm{LL}}$ is a reference Green's function satisfying

$$\mathrm{i}\frac{d}{d\tau_1} G_{0\mathrm{LL}}(1,2) = \delta(1,2) + \int_{\mathrm{L}} d3 H_{\mathrm{LL}}(1,3) G_{0\mathrm{LL}}(3,2). \tag{2.68}$$

Physically speaking, $G_{0\mathrm{LL}}$ represents the solution of the *equilibrium* semi-infinite lead when it is detached from the rest of the system. The retarded component $G^{\mathrm{R}}_{0\mathrm{LL}}$ is solved by applying Eq.(2.23a) to Eq.(2.68), and after performing a time-frequency Fourier transform, we obtain the matrix solution $G^{\mathrm{R}}_{0\mathrm{LL}}(\omega) = [\omega + \mathrm{i}0^+ - H_{\mathrm{LL}}]^{-1}$. As H_{LL} is tridiagonal in the principal layer representation, this matrix inversion can be computed exactly using the standard recursive algorithm [59],

---

[5] The other block G_{RD} satisfies the same set of equations with L replaced with R.

or by using the eigen-spectral representation [60] $G^{\mathrm{R}}_{0\mathrm{LL}}(\mathbf{r}_1, \mathbf{r}_2, \omega) = \sum_{\mathbf{k}\in\mathrm{L}} \psi_{\mathbf{k}}(\mathbf{r}_1)\psi^*_{\mathbf{k}}(\mathbf{r}_2)/(\omega - \varepsilon_{\mathbf{k}} + \mathrm{i}0^+)$. Once $G^{\mathrm{R}}_{0\mathrm{LL}}$ is solved, $G^{<}_{0\mathrm{LL}}$ and $G^{>}_{0\mathrm{LL}}$ can be calculated readily using Eq.(2.15).

Next, we place the spatial coordinates $\mathbf{r}_1$ and $\mathbf{r}_2$ of Eq.(2.39) both inside the device region. As such, only the central block of H_0G is involved: $H_0G \to H_{\mathrm{DL}}G_{\mathrm{LD}} + H_{\mathrm{DD}}G_{\mathrm{DD}} + H_{\mathrm{DR}}G_{\mathrm{RD}}$, which can be brought to a more compact form by defining $\Sigma_{\mathrm{L}} = H_{\mathrm{DL}}G_{0\mathrm{LL}}H_{\mathrm{LD}}$ and $\Sigma_{\mathrm{R}} = H_{\mathrm{DR}}G_{0\mathrm{RR}}H_{\mathrm{RD}}$. These two quantities are often termed the lead self-energies [44, 60]. Note that these self-energies have the same size as H_{DD} and, in order to calculate them, we only need the $G_{0\mathrm{LL}}$ or $G_{0\mathrm{RR}}$ matrix blocks at the first principal layer of the lead. Hence $H_0G \to (\Sigma_{\mathrm{R}} + \Sigma_{\mathrm{L}} + H_{\mathrm{DD}})G_{\mathrm{DD}}$, and we obtain a closed-form equation of motion for G_{DD}:

$$\mathrm{i}\frac{d}{d\tau_1}G_{\mathrm{DD}}(1,2) = \delta(1,2) + \int_{\mathrm{D}} d3 \left[H_{\mathrm{DD}}(1,3) + \Sigma_{\mathrm{tot}}(1,3)\right] G_{\mathrm{DD}}(3,2), \tag{2.69}$$

where Σ_{tot} also includes the effects from disorder-average and e-e interaction, i.e. $\Sigma_{\mathrm{tot}} = \Sigma_{\mathrm{L}} + \Sigma_{\mathrm{R}} + \Sigma_{\mathrm{dis}} + \Sigma_{\mathrm{ee}}$. Following the analytic continuation procedure as in Eq.(2.23), we get[6]

$$G^{\mathrm{R}}_{\mathrm{DD}}(\omega) = \left[\omega - H_{\mathrm{DD}} - \Sigma^{\mathrm{R}}_{\mathrm{tot}}(\omega)\right]^{-1}, \tag{2.70a}$$

$$G^{<}_{\mathrm{DD}}(\omega) = (1 + G^{\mathrm{R}}_{\mathrm{DD}}\Sigma^{\mathrm{R}}_{\mathrm{tot}})G^{<}_{0\mathrm{DD}}(1 + \Sigma^{\mathrm{A}}_{\mathrm{tot}}G^{\mathrm{A}}_{\mathrm{DD}}) + G^{\mathrm{R}}_{\mathrm{DD}}(\omega)\Sigma^{<}_{\mathrm{tot}}(\omega)G^{\mathrm{A}}_{\mathrm{DD}}(\omega). \tag{2.70b}$$

2.5.3 Charge current calculation

The charge current (per spin) flowing out of the left lead is defined by

$$I_{\mathrm{L}} = -e\frac{dN_{\mathrm{L}}}{dt} = -\frac{\mathrm{i}e}{\hbar}[H, N_{\mathrm{L}}],$$

where $N_{\mathrm{L}} = \int_{\mathrm{L}} d\mathbf{r}\hat{\psi}^\dagger(\mathbf{r})\hat{\psi}(\mathbf{r})$ is the total number operator of the left lead. Since interaction is assumed confined within the central device region, N_{L} commutes with all parts of the total Hamiltonian except for H_{DL} and H_{LD}. Hence the current can be expressed as

$$\begin{aligned} I_{\mathrm{L}} &= \frac{\mathrm{i}e}{\hbar}\int_{\mathrm{L}} d\mathbf{r}_1 \int_{\mathrm{D}} d\mathbf{r}_2 \left[H_{\mathrm{LD}}(\mathbf{r}_1, \mathbf{r}_2)\left\langle\hat{\psi}^\dagger(\mathbf{r}_1)\hat{\psi}(\mathbf{r}_2)\right\rangle - H_{\mathrm{DL}}(\mathbf{r}_2, \mathbf{r}_1)\left\langle\hat{\psi}^\dagger(\mathbf{r}_2)\hat{\psi}(\mathbf{r}_1)\right\rangle\right] \\ &= \frac{2e}{\hbar}\mathrm{Re}\left[\mathrm{Tr}\ H_{\mathrm{DL}}G^{<}_{\mathrm{LD}}(t,t)\right] = \frac{2e}{h}\int d\omega \mathrm{Re}\left[\mathrm{Tr}\ H_{\mathrm{DL}}G^{<}_{\mathrm{LD}}(\omega)\right], \end{aligned} \tag{2.71}$$

---

[6] The first term on the right hand side of Eq.(2.70b) usually vanishes in real calculations. Using the relation $G^{<}_{0\mathrm{DD}} = -f(\omega - \mu_{\mathrm{D}})(G^{\mathrm{R}}_{0\mathrm{DD}} - G^{\mathrm{A}}_{0\mathrm{DD}})$ together with Eq.(2.70a), this term can be rearranged to $2\mathrm{i}\eta f(\omega - \mu_{\mathrm{D}})G^{\mathrm{R}}_{\mathrm{DD}}G^{\mathrm{A}}_{\mathrm{DD}}$, where $\eta(\to 0^+)$ is the regularization factor introduced from time casuality. Assuming all states have a finite life-time due to either interaction or coupling to the reservoirs, the product $G^{\mathrm{R}}_{\mathrm{DD}}G^{\mathrm{A}}_{\mathrm{DD}}$ should not depend on η, and hence this term should vanish [55].

where the trace operates over the real-space. In obtaining the second line, we have used the original definition of $G^<$ and its anti-Hermitian feature. Applying the rules of Eq.(2.23c) to Eq.(2.67), we get $H_{\mathrm{DL}}G^<_{\mathrm{LD}} = G^<_{0\mathrm{LL}}H_{\mathrm{LD}}G^{\mathrm{A}}_{\mathrm{DD}} + G^{\mathrm{R}}_{0\mathrm{LL}}H_{\mathrm{LD}}G^<_{\mathrm{DD}}$. Substituting this relation into Eq.(2.71) and using the definition of $\Sigma_{\mathrm{L}} = H_{\mathrm{DL}}G_{0\mathrm{LL}}H_{\mathrm{LD}}$, we obtain

$$I_{\mathrm{L}} = \frac{2e}{h}\int d\omega \mathrm{Re\ Tr}\left[\Sigma^<_{\mathrm{L}}(\omega)G^{\mathrm{A}}_{\mathrm{DD}}(\omega) + \Sigma^{\mathrm{R}}_{\mathrm{L}}(\omega)G^<_{\mathrm{DD}}(\omega)\right]. \tag{2.72}$$

This formula signifies that, in order to calculate the current, one only needs to compute some real-space integrals confined in the device region. The impact from other degrees of freedom in the lead is encoded in the Σ_{L} self-energy, which has the same size as H_{DD} and has no dependence on the interaction or disorder within the central device.

It is possible to cast Eq.(2.72) into a physically more transparent form. To this end, we apply the identity $\mathrm{Re\ Tr}[M] = \frac{1}{2}\mathrm{Tr}[M + M^\dagger]$ to the integrand of Eq.(2.72) and use the fact $G^> - G^< = G^{\mathrm{R}} - G^{\mathrm{A}}$:

$$\begin{aligned}\mathrm{Re\ Tr}\left[\Sigma^<_{\mathrm{L}}G^{\mathrm{A}}_{\mathrm{DD}} + \Sigma^{\mathrm{R}}_{\mathrm{L}}G^<_{\mathrm{DD}}\right] &= \frac{1}{2}\mathrm{Tr}\left[\Sigma^<_{\mathrm{L}}(G^{\mathrm{A}}_{\mathrm{DD}} - G^{\mathrm{R}}_{\mathrm{DD}}) + (\Sigma^{\mathrm{R}}_{\mathrm{L}} - \Sigma^{\mathrm{A}}_{\mathrm{L}})G^<_{\mathrm{DD}}\right] \\ &= \frac{1}{2}\mathrm{Tr}\left[-\Sigma^<_{\mathrm{L}}G^>_{\mathrm{DD}} + \Sigma^>_{\mathrm{L}}G^<_{\mathrm{DD}}\right]. \end{aligned} \tag{2.73}$$

Hence we obtain an equivalent formula for calculating the current:

$$I_{\mathrm{L}} = \frac{e}{h}\int d\omega \mathrm{Tr}\left[\Sigma^<_{\mathrm{L}}(\omega)G^>_{\mathrm{DD}}(\omega) - \Sigma^>_{\mathrm{L}}(\omega)G^<_{\mathrm{DD}}(\omega)\right]. \tag{2.74}$$

The physical picture implied by Eq.(2.74) is quite clear: The second (first) term in the integrand represents the hole (electron) current as $\Sigma^>_{\mathrm{L}}$ ($\Sigma^<_{\mathrm{L}}$) represents the hole (electron) transfer rate from the lead to the device and $G^<_{\mathrm{DD}}$ ($G^>_{\mathrm{DD}}$) represents the available hole (electron) states in the device. The current through the right lead I_{R} can be derived in exactly the same way.

Suppose the temperature is set at zero and $\mu_L > \mu_R$. In the energy window $\mu_L > \omega > \mu_R$, $\Sigma^>_{\mathrm{L}}$ must vanish, and hence only the first term in Eq.(2.74) retains, which equals $(2\mathrm{iIm}\Sigma^{\mathrm{R}}_{\mathrm{L}})G^>_{\mathrm{DD}}$. When interaction is omitted, $G^>_{\mathrm{DD}} = G^{\mathrm{R}}_{\mathrm{DD}}(-2\mathrm{iIm}\Sigma^{\mathrm{R}}_{\mathrm{R}})G^{\mathrm{A}}_{\mathrm{DD}}$. Thus the integrand of Eq.(2.74) becomes

$$\mathcal{G}(\omega) = 4\frac{e}{h}\mathrm{Tr}\left[\mathrm{Im}\Sigma^{\mathrm{R}}_{\mathrm{L}}(\omega)G^{\mathrm{R}}_{\mathrm{DD}}(\omega)\mathrm{Im}\Sigma^{\mathrm{R}}_{\mathrm{R}}(\omega)G^{\mathrm{A}}_{\mathrm{DD}}(\omega)\right], \tag{2.75}$$

i.e. the conductance of the system. More generally, the conductivity of a noninteracting system reads

$$\sigma_{xx} = -\frac{e^2\hbar^3}{2\pi m^2\Omega}\int d\mathbf{r}d\mathbf{r}'\mathrm{Re}\left[\frac{\partial}{\partial x}G^{\mathrm{R}}(\mathbf{r},\mathbf{r}',\varepsilon_{\mathrm{F}})\frac{\partial}{\partial x'}G^{\mathrm{A}}(\mathbf{r}',\mathbf{r},\varepsilon_{\mathrm{F}})\right]. \tag{2.76}$$

The derivation of Eq.(2.76) involves the linear response Kubo formalism, for which the reader is referred to Refs.[12, 60].

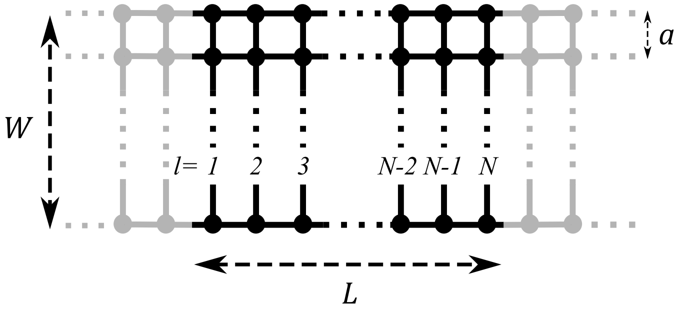

Figure 2.15: A discrete ribbon-shaped lattice which simulates a quantum wire. The grey areas denote the electrodes. l denotes the principal layer index. L and W denote the numbers of sites in the longitudinal and transverse directions respectively. Note that disorder and e-e interaction are restricted in the central region (black).

Apart from the currents through the leads, the current at the interface between adjacent principal layers can also be calculated. To this end, we take time derivative of $N_l = \int_l d\mathbf{r}\hat{\psi}^\dagger(\mathbf{r})\hat{\psi}(\mathbf{r})$, i.e. the total number operator of the lth principal layer. Since N_l commutes with the total Hamiltonian except for $H_{l\pm1,l}$ and $H_{l,l\pm1}$, similar to the case in Eq.(2.71), we get

$$\frac{d\langle N_l\rangle}{dt} = \frac{2e}{h}\int d\omega \mathrm{Re}\left[\mathrm{Tr}\ H_{l-1,l}G^<_{l,l-1}(\omega) - \mathrm{Tr}\ H_{l,l+1}G^<_{l+1,l}(\omega)\right]. \tag{2.77}$$

The first term on the right hand side is identified as the current flowing into the lth layer from the $(l-1)$th layer, while the second term represents the outgoing current on the other side. This leads to another useful formula for calculating the current:

$$I_l = \frac{2e}{h}\int d\omega \mathrm{Re}\left[\mathrm{Tr}\ H_{l-1,l}G^<_{l,l-1}(\omega)\right]. \tag{2.78}$$

For a theoretical calculation which respects conservation laws, the value of I_l should be independent of l; besides the relation $I_l = I_\mathrm{L} = -I_\mathrm{R}$ must hold.

2.5.4 Discretization

In this subsection we construct a necessary numerical model in order to implement the theories we develop in this thesis. To this end we discretize the real-space with an orthogonal grid (see Fig.2.15). The Coulomb interaction is thus written as $U_{ij} = ua/|\mathbf{r}_i - \mathbf{r}_j|$, where a is the lattice constant, u is a scale parameter, and $i(j)$ is a site label. To regularize U_{ij} at $i = j$, we note that for a spinless fermionic system the Hartree and Fock contributions exactly cancel each other at $i = j$, and thus we can simply set $U_{ii} = 0$. For electrons on the other hand, the interaction between opposite spin components could retain at $i = j$. In this case we parameterize the onsite interaction as $U_0\hat{n}_{i\uparrow}\hat{n}_{i\downarrow}$, which replaces the ill defined Coulomb interaction at $i = j$.

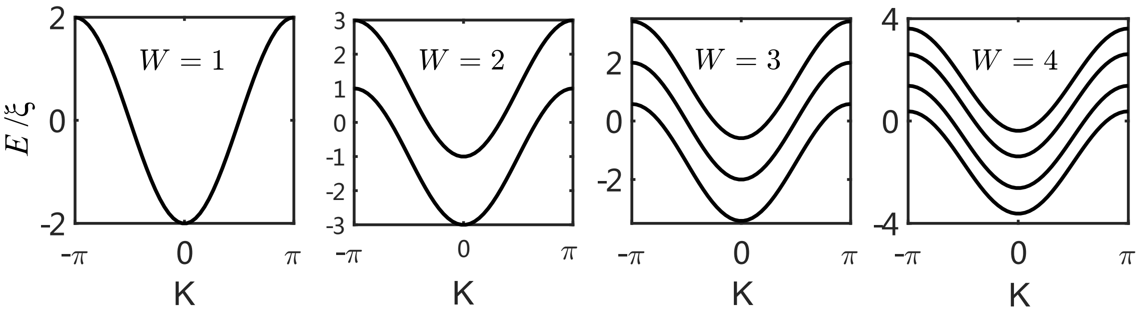

Figure 2.16: Band structures of the lattice systems defined in Fig.2.15 under the perfect condition, i.e. without disorder or interaction. Note that we have shifted the band centers to the energy zero point.

The kinetic energy is associated with the Laplacian $\nabla^2 = \partial_x^2 + \partial_y^2 + \partial_z^2$ which, if restricted in one-dimension, is discretized as [60]

$$\left[\frac{\partial^2 F}{\partial x^2}\right]_{x=ja} \approx \frac{F_{j+1} - 2F_j + F_{j-1}}{a^2} + O(a^2). \tag{2.79}$$

We notice that at this level of finite difference approximation the kinetic energy only couples the lattice sites which are nearest neighbors, with a coupling coefficient $\xi = \hbar^2/2ma^2$. In the absence of disorder and interactions, the band structures of thus defined lattice are illustrated in Fig.2.16 with different W. In the presence of magnetic field, the coupling needs to be modified by multiplying an additional phase factor [60]:

$$\xi_{ij} = \frac{\hbar^2}{2ma^2} \exp\left[\frac{\mathrm{i}e}{\hbar}\mathbf{A}\cdot(\mathbf{r}_i - \mathbf{r}_i)\right], \tag{2.80}$$

where $\mathbf{A}$ is vector potential.

To sum up, we obtain the following Hamiltonian for the discrete lattice [cf. Eq.(2.1)]:

$$\mathcal{H} = \sum_{i,j} \xi_{ij} c_i^\dagger c_j + \sum_i v_i \hat{n}_i + \frac{1}{2}\sum_{i\neq j} U_{ij}\hat{n}_i\hat{n}_j + \sum_i U_0 \hat{n}_{i\uparrow}\hat{n}_{i\downarrow}, \tag{2.81}$$

which is also known as the Anderson-Hubbard model in the literature [32].[7] This model is widely studied in the condensed matter physics as it serves as a prototypical platform for the studies of a broad spectrum of quantum phases. In particular, in chapter 3 we shall neglect the e-e interaction terms in Eq.(2.81) and study the most elementary scattering processes off the random potential v_i. The interaction associated effects will be discussed later on in chapters 4 and 5.

The Feynman diagrams formulated in this chapter using the continuum model can be translated into the discrete representation in a straightforward manner: one simply replaces the continuous variables $\mathbf{r}$ with the discrete site indices i, and integration $\int d\mathbf{r}$ with summation $\sum_i$ [33].

---

[7] The model reduces to the Anderson or the Hubbard model respectively in absence of e-e interaction or disorder.

2.6 Summary

In this chapter, we have reviewed the nonequilibrium Green's function formalism based on the Keldysh complex-time contour. Whereas the Green's functions are exactly solvable under a quadratic Hamiltonian, they do not have a closed-form solution in general systems that contain a disordered potential or subject to the e-e interaction. In order to address these two effects, perturbation series have been formulated with the aid of the diagram technique. We have also demonstrated how to compute the diagrams in these series using the real-time Green's functions which are numerically more advantageous. Care needs to be taken in the selection of diagrams as they need to meet certain requirements. Here we have focused on the requirements associated with the conservation laws. In particular the Kadanoff-Baym theory was reviewed, which ensures the thus constructed diagrams to be conserving at the one-particle level. We have also formulated a set of Ward identities for the disorder-averaged Green's function products. These identities are implicitly related to the conservation laws and are useful for checking the theoretical consistency of a diagrammatic scheme. Finally, to connect with the modeling of real-world mesoscopic devices, we demonstrated how to use the Green's function to calculate the steady-state currents in finite systems subject to an open boundary condition.

Chapter 3

Quantum diffusion and localization

From a microscopic point of view, a large class of transport phenomena are essentially a higher-level reflection of the underlying carrier distribution in the momentum space. Neglecting interactions between the carrier, a system with translational invariance in the real-space must hence be trivial in the context of transport physics, because of momentum conservation. The translational invariance can be broken by inducing randomly distributed impurities, each producing a localized potential in its vicinity. For a classical particle travelling in such a disordered medium, its momentum would be randomized after a series of scattering events, and hence its probability migration can be well described by the Drude (drift-diffusion) formula [7] at the macroscopic level. The same picture remains valid for a quantum particle as long as it stays in the classical regime, namely when its wavelength λ is much smaller than the mean separation l_0 between impurities ($\lambda \ll l_0$). However in mesoscopic samples which are typically semiconducting materials, λ could be relativley large so that the condition $\lambda \ll l_0$ is not necessarily met. Therefore in this regime the particle should rather be treated as a wave. The major difference between a classical particle and a wave when they are scattered off a series of impurities is that the wave interferes with itself. It turns out that this interference can usually lead to an enhanced backscattering counteracting on the diffusive flow, also known as the localization effect in the context of electronic transport.[1] As a result, the measured conductance of a disordered mesoscopic sample is typically lower than according to the Drude theory.

This chapter is devoted to reviewing the mesoscopic transport theory of weakly disordered systems where the transport is dominated by the diffusive process. The (weak) localization effect is taken into account as a perturbation correction to the diffusion. We shall demonstrate how to

---

[1] For certain exotic materials having an unconventional band structure, the interference due to multiple scattering may instead lead to a suppressed back scattering, i.e. anti-localization [61].

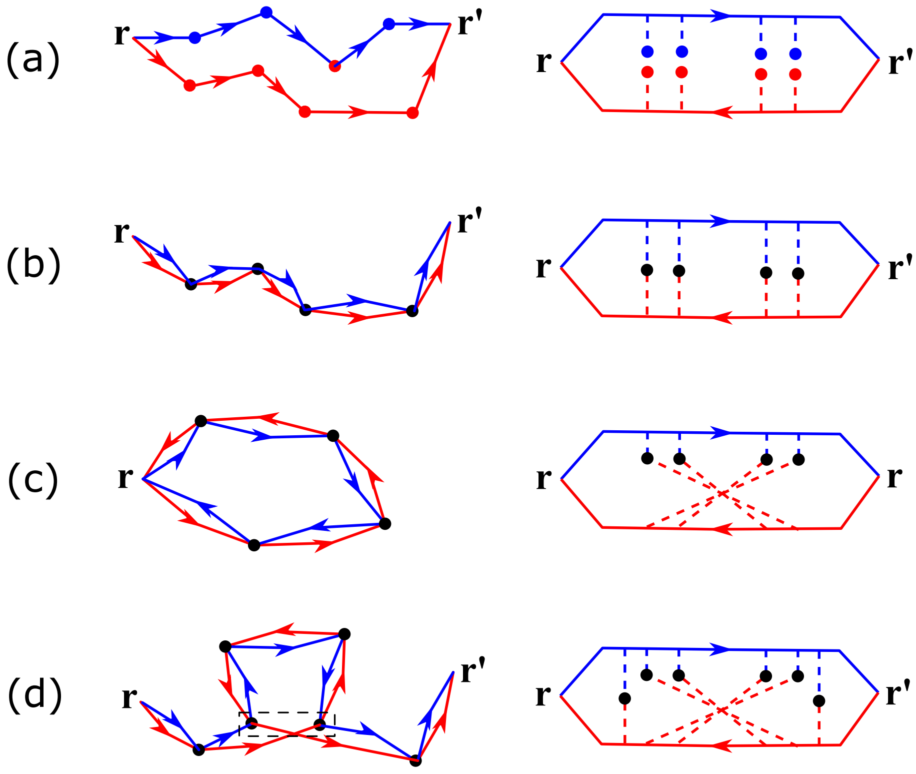

Figure 3.1: Diagrams for different trajectories contributing to the propagation probability. Arrowed lines represent the propagators G^{R} and dots are scatterers. (a) a general pair of trajectories with no alignment. (b) a pair of identical trajectories. (c) a loop trajectory and its time-reversal counterpart. (d) a trajectory with a loop insertion.

describe these physical effects using the diagrammatic language developed in Chapter 2. Moreover, noticing that most understandings on mesoscopic diffusion and localization are derived within the linear response Kubo formalism [12], a central task of this chapter is therefore to reformulate these theories in the more general Keldysh formalism applicable in nonequilibrium. The reformulation enables us to adapt the coherent potential approximation [58, 62] and the dual fermion method [2] to addressing diffusion and localization in finite open structures modeled in real space.

3.1 General picture

Heuristically, the wavefunction of a particle propagating from $\mathbf{r}$ to $\mathbf{r}'$ is written as the following superposition of path-integrals:

$$\Psi(\mathbf{r},\mathbf{r}') = \sum_{N=1}^{\infty} \int d\mathbf{r}_1 \cdots d\mathbf{r}_N G^{\mathrm{R}}(\mathbf{r},\mathbf{r}_1) v(\mathbf{r}_1) G^{\mathrm{R}}(\mathbf{r}_1,\mathbf{r}_2) v(\mathbf{r}_2)$$

$$\times \cdots v(\mathbf{r}_{N-1}) G^{\mathrm{R}}(\mathbf{r}_{N-1}, \mathbf{r}_N) v(\mathbf{r}_N) G^{\mathrm{R}}(\mathbf{r}_N, \mathbf{r}'), \tag{3.1}$$

where $v(\mathbf{r})$ denotes the randomly distributed static potential, and $G^{\mathrm{R}}(\mathbf{r}, \mathbf{r}')$ is the propagator free of scattering. The propagation probability is hence $|\Psi(\mathbf{r}, \mathbf{r}')|^2$ which consists of a sum over all the pairs of paths connecting $\mathbf{r}$ to $\mathbf{r}'$.

Since it is impossible to enumerate every path pair, we wish to be able to pick out those of major contribution to $|\Psi(\mathbf{r}, \mathbf{r}')|^2$. To this end, we first rule out those pairs with a large part of misalignment in the real-space, as illustrated in Fig.3.1(a). The reason is that such a pair carries a dephasing factor $e^{\mathrm{i}k(L_2 - L_1)}$, where k is the wavenumber and $L_{1,2}$ are the trajectory lengths; this factor varies randomly from path to path and sample to sample, thus making no net contribution. What's more, trajectories made of differing scatters cannot survive disorder-average whatsoever, because at any noncommon scatter we get $\overline{v(\mathbf{r})} = 0$ (see Sec.2.2.1). With these considerations we can therefore focus only on those pairs of trajectories that overlap in the real-space. Such a pair can be simply realized by putting together two identical trajectories, as shown in Fig.3.1(b). This group of trajectories amount to the following quantity, termed the "diffuson" in the literature [12]:

$$\sum_{N=1}^{\infty} \int d\mathbf{r}_1 \cdots d\mathbf{r}_N |G^{\mathrm{R}}(\mathbf{r}, \mathbf{r}_1)|^2 v(\mathbf{r}_1) |G^{\mathrm{R}}(\mathbf{r}_1, \mathbf{r}_2)|^2 v(\mathbf{r}_2) \cdots |G^{\mathrm{R}}(\mathbf{r}_N, \mathbf{r}')|^2 \equiv \mathcal{P}(\mathbf{r}, \mathbf{r}'), \tag{3.2}$$

which clearly shows a structure describing sequential scatterings that are independent on each other. Therefore $\mathcal{P}(\mathbf{r}, \mathbf{r}')$ corresponds to the classical diffusion. Using its diagrammatic representation (right panel of Fig.3.1b), we see that $\mathcal{P}(\mathbf{r}, \mathbf{r}')$ is closely related to the $C^{(2)}$ correlator, when its kernel $K^{(2)}$ is approximated to the lowest order.

Notice that pairing up identical trajectories is not the only way to eliminate the phase misalignment. For any path that intersects itself, one can reverse the scattering order around the loop, and the thus generated trajectories are phase aligned. This procedure is illustrated in Fig.3.1(c). Now consider the return probability $|\Psi(\mathbf{r}, \mathbf{r})|^2$ under time-reversal symmetry, i.e. $G^{\mathrm{R}}(\mathbf{r}_1, \mathbf{r}_2) = G^{\mathrm{R}}(\mathbf{r}_2, \mathbf{r}_1)$. One can see that $|\Psi(\mathbf{r}, \mathbf{r})|^2$ becomes twice as much as $\mathcal{P}(\mathbf{r}, \mathbf{r})$ when the reversal trajectories such as Fig.3.1(c) are taken into account. In other words, due to the interference of time-reversal paths which comes from the cross terms in $|\Psi|^2$, the return probability of a quantum particle gets enhanced. This is precisely the origin of the weak localization effect. Diagrammatically the interference between time-reversal paths is usually represented by a maximal cross as shown in Fig.3.1(c), also known as the "Cooperon" in the literature [12]. The cross can be untangled by reversing one of the G^{R}-lines, and the result would be identical to the diffuson $\mathcal{P}$ under time-reversal symmetry.

There is one thing we need to clarify before closing this section: that the return probability of particle propagation gets doubled by the Cooperon process does not contradict the fact that

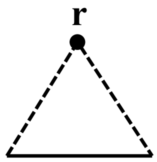

Figure 3.2: First-order disorder self-energy. The dashed object represents the cumulant $\gamma^{(2)}$.

the weak localization might only amount to a subleading correction to the diffusion-dominated electrical conductance. The reason is that the conductance is essentially a nonlocal quantity and is thus not directly associated with $|\Psi(\mathbf{r},\mathbf{r})|^2$. We illustrate in Fig.3.1(d) a diagram pertaining to the weak localization correction to the *nonlocal* $|\Psi(\mathbf{r},\mathbf{r}')|^2$. The Cooperon is located at the middle of the path way and is linked with two diffusons. As shown in the dashed box, in general some degree of trajectory misalignment could occur at the intersection, thereby lowering the return probability at that point effectively.

3.2 Propagator formalism

In this section we put the qualitative pictures described above into some real calculations. We shall continue thinking of the particles as propagating waves extending in the disordered medium. In comparison to the locator formalism to be shortly introduced in Sec.3.3, the propagator picture used here may not be ideal for computations of numerical models, but it is useful for analytical discussions. Specifically we shall derive the energy distribution function of electrons in a diffusive conductor, which will be invoked in subsequent chapters, and the semiclassical Drude conductivity using only the lowest-order approximation. On top of that, the Cooperon contribution to the electrical conductivity will be calculated and analyzed using the diagram technique.

Throughout the calculations we shall limit ourselves to the weak disorder scenario, i.e. $\lambda \ll l_0$. Under this assumption the diagram series of Fig.2.2 becomes perturbative, and hence we can start with the lowest-order diagram Fig.3.2, which is written as

$$\Sigma^{\mathrm{R}}(\mathbf{r},\mathbf{r}',\varepsilon) = \delta(\mathbf{r}-\mathbf{r}')\gamma^{(2)}(\mathbf{r})G^{\mathrm{R}}(\mathbf{r},\mathbf{r},\varepsilon), \tag{3.3}$$

i.e. the first Born approximation. We notice that the diagonal of $-\mathrm{Im}G^{\mathrm{R}}/\pi$ is just the local density of states $\nu_0(\mathbf{r},\varepsilon)$. Therefore, when transformed into the momentum space, Eq.(3.3) gives

$$\mathrm{Im}\Sigma^{\mathrm{R}}(\mathbf{k},\varepsilon) = -\pi\nu_0(\varepsilon)\gamma \equiv -\frac{1}{2\tau_0(\varepsilon)}. \tag{3.4}$$

The quantity τ_0 introduced above has the physical meaning of (momentum) relaxation time. In writing down the above equation, we have assumed a uniformly disordered system such that the

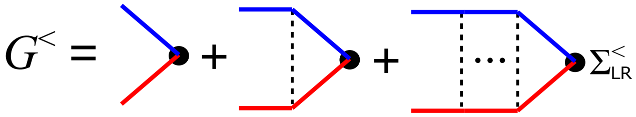

Figure 3.3: Recursive relation for the lesser Green's function $G^<$. Each dashed line represents a factor of $\gamma^{(2)}$ which measures the scattering rate. Solid lines represent either retarded (blue) or advanced (red) Green's functions. Black dots represent the lesser lead self-energy $\Sigma^<_{\rm LR}$.

density of states (ν_0), as well as the cumulant (γ), is position independent. Plugging Eq.(3.4) into Eq.(2.29), we get

$$G^{\rm R,A}(\mathbf{k},\varepsilon) = \frac{1}{\varepsilon - E(\mathbf{k}) \pm \frac{\rm i}{2\tau_0(\varepsilon)}}, \tag{3.5}$$

where ${\rm Re}\Sigma^{\rm R}$ has been absorbed into the band dispersion $E(\mathbf{k})$. Since $\hbar/\tau_0$ represents an energy scale much smaller than the Fermi energy in the weak scattering limit, Eq.(3.5) yields a quasi-particle spectrum sharply peaked at $\varepsilon = E(\mathbf{k})$ where the peak width $\sim \tau_0^{-1}$.

Since in the presence of impurities the particle propagation is subject to random scattering, invoking the classical picture we would imagine the nonequilibrium transport being diffusive. It turns out that, within the first order approximation, quantum particles are predicted to also follow this diffusive behavior, i.e. quantum diffusion. To see this we shall calculate the distribution function in a disordered conductor. To this end we utilize Eq.(2.70b), i.e.

$$G^<(\mathbf{r}_1,\mathbf{r}_2,\varepsilon) = \int G^{\rm R}(\mathbf{r}_1,\mathbf{r},\varepsilon)\left[\Sigma^<_{\rm LR}(\mathbf{r},\varepsilon) + \Sigma^<_{\rm dis}(\mathbf{r},\varepsilon)\right] G^{\rm A}(\mathbf{r},\mathbf{r}_2,\varepsilon)d\mathbf{r}, \tag{3.6}$$

where $\Sigma^<_{\rm LR}$ is the lead self-energy and $\Sigma^<_{\rm dis}(\mathbf{r},\varepsilon) = \gamma G^<(\mathbf{r},\mathbf{r},\varepsilon)$ is the lesser self-energy under the lowest-order approximation. A recursive relation for $G^<$ is implied in Eq.(3.6), as can be visualized by the diagram shown in Fig.3.3. One then immediately notices the diffuson (ladder) structure which we introduced in Sec.3.1.

Assuming the diagonal $G^<(\mathbf{r},\mathbf{r},\varepsilon)$ can be written in the form $2\pi{\rm i}f(\mathbf{r},\varepsilon)\nu_0(\varepsilon)$, we obtain from Eq.(3.6)

$${\rm i}f(\mathbf{r}) = \int_S \mathcal{P}(\mathbf{r},\mathbf{r}',\omega=0)\Sigma^<_{\rm LR}(\mathbf{r}')d\mathbf{r}', \tag{3.7}$$

where the integral is limited at the interfaces between the device and the reservoirs since lead self-energies vanish elsewhere. In Appendix B it is shown that the diffuson $\mathcal{P}$ is the Green's function of the classical diffusion equation (B.12). Therefore the distribution function f should satisfy[2]

$$D\nabla^2 f(\mathbf{r},\varepsilon) = {\rm i}\Sigma^<_{\rm L}(\mathbf{r},\varepsilon)\delta(x) + {\rm i}\Sigma^<_{\rm R}(\mathbf{r},\varepsilon)\delta(x-L), \tag{3.8}$$

---

[2] The device-reservoir interfaces are placed at $x = 0, L$ respectively.

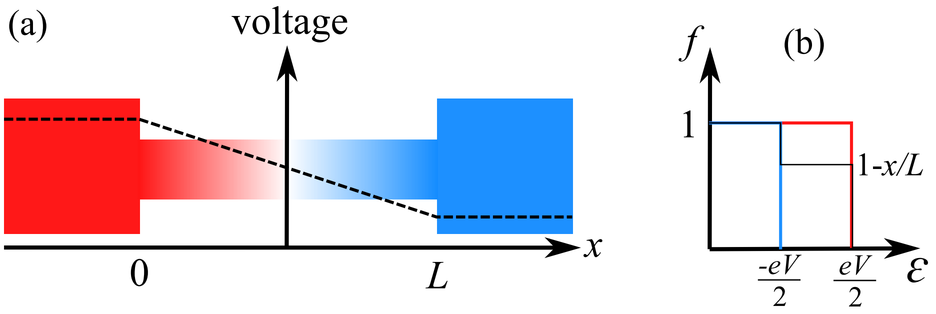

Figure 3.4: (a) Schematic of a disordered conductor sandwiched between electric leads (reservoirs). The voltage drops linearly across the wire, corresponding to the classical Drude transport. (b) Electronic energy distribution in the conductor [see Eq.(3.9)]. The blue and the red curves represent the distributions in the right and the left leads respectively, and the black curve represents that at the position x.

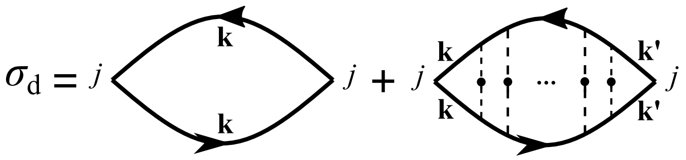

Figure 3.5: Diagram expansion for the linear conductivity formulated under the first-order approximation. The recursive kernel here, obtained by differentiating the self-energy (see Fig.3.2) over Green's function, is simply the lowest-order cumulant $\gamma^{(2)}$ (dashed line).

where D is diffusion coefficient. On the right hand side of Eq.(3.8), the lead self-energies serve as the particle source or drain, depending on the relative values of their chemical potentials to ε. This is consistent with the physical interpretation which we gave to $\Sigma^{<}_{\mathrm{L/R}}$ in writing down the charge current formula (2.74): it represents the particle exchange rate between the device and the reservoirs. Since $\nabla^2 f(\mathbf{r},\varepsilon) = 0$ away from the interfaces, f varies linearly within the device. The boundary condition for f is such that it connects continuously with the respective equilibrium distributions in reservoirs. We hence obtain

$$f(\varepsilon,x) = f(\varepsilon,0) + \frac{x}{L}\left[f(\varepsilon,L) - f(\varepsilon,0)\right], \tag{3.9}$$

where $f(\varepsilon,0) = \left[\exp\frac{\varepsilon-\mu_{\mathrm{L}}}{k_{\mathrm{B}}T}+1\right]^{-1}$, $f(\varepsilon,L) = \left[\exp\frac{\varepsilon-\mu_{\mathrm{R}}}{k_{\mathrm{B}}T}+1\right]^{-1}$. The derived distribution function is illustrated in Fig.3.4.

The above analysis is based on a picture where the system consists of a finite structure sandwiched between non-equilibrated reservoirs (leads). For very large structures the leads can be dropped out of the picture and one should instead use the Kubo formula (2.76) to compute the linear response conductivity. Assuming translational invariance, it is then convenient to Fourier

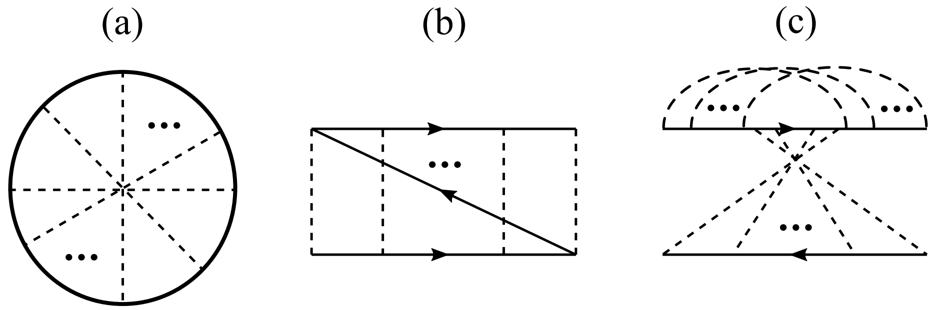

Figure 3.6: Cooperon diagrams for describing the localization effect. (a) Luttinger-Ward Φ-diagram. (b) Self-energy. (c) Two-particle kernel $K^{(2)}$. Note that the vertical flip of (c) should also be included in $K^{(2)}$, which we omit showing here.

transform Eq.(2.76):

$$\sigma_{xx} = \frac{e^2\hbar^3}{2\pi m^2 \Omega} \sum_{\mathbf{k},\mathbf{k}'} k_x {k_x}' \left\langle G^{\mathrm{R}}(\mathbf{k},\mathbf{k}',\varepsilon) G^{\mathrm{A}}(\mathbf{k}',\mathbf{k},\varepsilon) \right\rangle . \tag{3.10}$$

Under the first order approximation, the irreducible kernel $K^{(2)}$ for calculating the average product of two Green's functions is simply the lowest-order cumulant γ. Hence the conductivity can be formulated with the ladder diagram shown in Fig.3.5. It turns out that the second part of this diagram should be dropped out, because the momenta k_x and k'_x are summed over separately. The only contributing term is thus the one without ladder dressing, where $k_x = k'_x$. Therefore,

$$\sigma_{\mathrm{d}} = \frac{e^2\hbar^3}{2\pi m^2} \int \frac{d\mathbf{k}}{(2\pi)^d} {k_x}^2 G^{\mathrm{R}}(\mathbf{k},\varepsilon) G^{\mathrm{A}}(\mathbf{k},\varepsilon) = e^2 D \nu_0 . \tag{3.11}$$

The k-integration is performed with the aid of Eqs.(B.3) and (B.9). The result of Eq.(3.11) coincides with the classical Drude formula. We have thus confirmed that the lowest-order diagram Fig.3.2 indeed leads to a *diffusive* description of charge transport in disordered media.

As discussed in Sec.3.1, a full description of charge transport in disordered media needs to take into account the localization effect from Cooperon processes. To this end one has to go beyond the lowest-order approximation (Fig.3.2). Following the standard Kadanoff-Baym scheme, we start by drawing the Luttinger-Ward diagram of Cooperon, which is presented as the maximum crossing diagram in Fig.3.6(a). The self-energy and the two-particle kernel $K^{(2)}$ are hence derived from it by removing Green's function lines. The results are shown in Fig.3.6(b,c).

According to the general theory presented in Sec.2.2.2, the calculation of the Green's function product involved in the Kubo formula Eq.(3.10) requires iterating $K^{(2)}$ along the particle-hole channel. However, invoking the same argument as in getting to Eq.(3.11), one finds Fig.3.7(a) being the only diagram that contributes. Note that, for visual convenience, the maximum cross

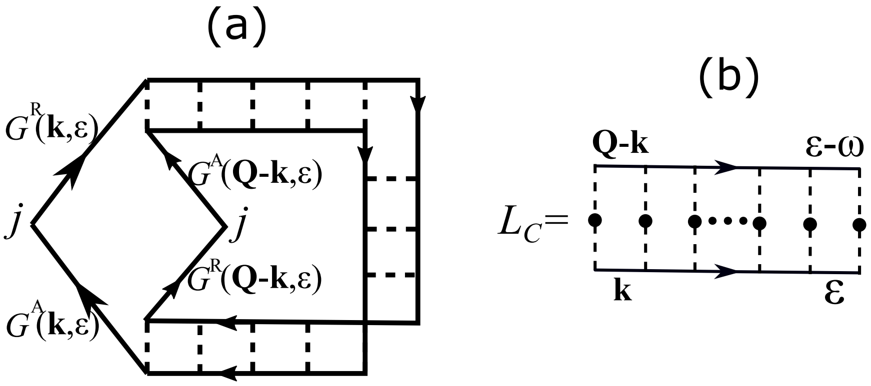

Figure 3.7: (a) Conductivity diagram associated with the Cooperon process. (b) Illustration of the internal (ladder) structure of the Cooperon.

is disentangled in Fig.3.7(a) by flipping the direction of one of the Green's function lines. The resulting Cooperon ladder Fig.3.7(b) has a similar structure as that of diffuson, except that for Cooperon the directions of the two Green's functions are parallel. Under time-reversal symmetry, $G^{\mathrm{R}}(\mathbf{k},\varepsilon) = G^{\mathrm{R}}(-\mathbf{k},\varepsilon)$, and therefore $\mathcal{L}_C$ simply equals the diffuson ladder in the limit $Ql_0 \ll 1$, i.e.

$$\mathcal{L}_C(\omega,\mathbf{Q}) = \frac{\gamma}{\tau_0}\frac{1}{-\mathrm{i}\omega + DQ^2}. \tag{3.12}$$

Note that here Q is the total momentum of the two particles instead of their difference [cf. Eq. (B.11)]. The fact that $\mathcal{L}_C$ is dominated by small Q signifies that the Cooperon is a measurement of the long-range correlation between antiparallel waves, i.e. $\mathbf{k} \approx -\mathbf{k}'$.

Using Eqs.(B.5) and (B.9), the diagram of Fig.3.7(a) is hence evaluated as

$$\sigma_C \approx \frac{e^2\hbar^3}{2\pi m^2}\int \frac{d\mathbf{k}}{(2\pi)^d}k_x^2\left[G^{\mathrm{R}}(\mathbf{k},\varepsilon)G^{\mathrm{A}}(\mathbf{k},\varepsilon)\right]^2\int \frac{d\mathbf{Q}}{(2\pi)^d}\mathcal{L}_C(\omega=0,\mathbf{Q}) = -\frac{e^2}{\pi\hbar}\int \frac{Q^{-2}d\mathbf{Q}}{(2\pi)^d}, \tag{3.13}$$

which amounts to a negative correction to the diffusive conductivity. It is important to notice that the last Q-integral in Eq.(3.13) diverges in lower limit for dimensions $d \le 2$ and in upper limit for all dimensions. The latter can be easily regularized by imposing the cutoff $Q < 1/l_0$, as required under the diffusive approximation. The lower cutoff can be naturally approximated by the inverse system size L^{-1}. We thus obtain

$$\sigma_C = \begin{cases} -e^2h^{-1}(L - l_0) & d = 1 \\ -\pi^{-1}e^2h^{-1}\ln L/l_0 & d = 2 \end{cases} \tag{3.14}$$

This result seems to suggest that the conductivity of a low-dimensional disordered system tend to vanish (or even go negative) as L grows. In fact this bizarre finding is not a nonsense: using scaling analysis, Abraham *et al.*[63] pointed out that in $d \leq 2$ no macroscopic transport is allowed in disordered systems with an arbitrary impurity concentration. This so-called “Anderson localization” phenomenon [64] is a general quantum effect due to long-range interferences. Nevertheless, in real materials the interference is always cut off by certain dephasing effects, such as density fluctuation, electron-phonon scattering, or external magnetic fields. In macroscopic samples the dephasing length L_ϕ is much smaller than the sample size, and thus the lower bound of the Cooperon wavevector (Q) should be replaced with L_ϕ^{-1}, which is usually invariant against increasing the sample size. We shall not further elaborate on the physical formalism for describing the intrinsic dephasing processes. The reader is referred to Refs.[12, 23] for detailed reviews on this topic.

3.3 Locator formalism

Whereas the above analyses based on the propagator formalism have succeeded in capturing the global features of quantum diffusion and weak localization, yet the propagator picture is not really practical for numerical computations. The reason is two twofold. First of all, the accuracy of the above formalism drops quickly as the disorder strength (i.e. $\gamma^{(2)}$) increases. Secondly, the numerical transport model (Fig.2.15) studied in this thesis does not even admit the $\mathbf{r} \to \mathbf{k}$ Fourier transform, due to the lack of translational invariance. In order to address these issues, we switch from the propagator view to a local perspective, which takes the Green’s function of an isolated single site, namely the locator [48, 65–67], as reference while treating the intersite hopping perturbatively. The motivation for the locator formalism is that, when disorder increases, electrons tend to localize more, and hence locators become more suitable for describing the electronic structures. In fact, for a binary alloy wherein the random onsite potential $v_i = \pm v$, the locator becomes the exact solution to the problem in the limit $v/\xi \gg 1$ [48], where ξ is the intersite hopping amplitude. In the other limit $v/\xi \ll 1$, as will be shortly seen, the locator formalism is also able to generate the exact global Green’s function for the disordered medium.

To formally develop the locator formalism, we start over from the v-dependent Green’s function as formulated in Eq.(2.26). Written in the upper-triangular form [see Eq.(2.18)],

$$\begin{bmatrix} G_v^{\mathrm{R}} & G_v^{<} \\ 0 & G_v^{\mathrm{A}} \end{bmatrix} = \begin{bmatrix} \omega - v - H_0^{\mathrm{R}} & -H_0^{<} \\ 0 & \omega - v - H_0^{\mathrm{A}} \end{bmatrix}^{-1} \tag{3.15}$$

Without loss of generality, H_0 denotes a disorder-independent matrix, including but not limited to the underlying Hamiltonian: for example H_0 could incorporate the lead self-energy. Trivially, one is allowed to introduce an arbitrary matrix $\Delta(\omega)$ such that $G_v(\omega) = [\omega - v - \Delta(\omega) + \Delta(\omega) - H_0]^{-1}$.

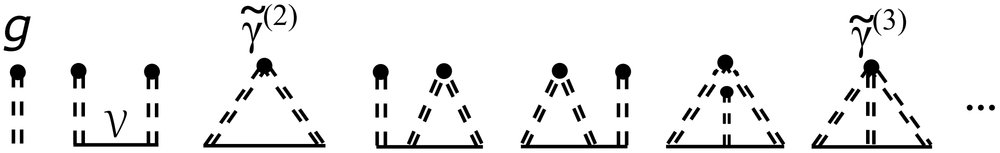

Figure 3.8: Diagrammatic series in the locator formalism for the disorder-averaged Green's function (cf. Fig.2.2). Doubly dashed lines represent locator cumulants $\tilde{\gamma}^{(n)}$, and solid lines represent the $\mathcal{V}$ matrix (defined in the main text).

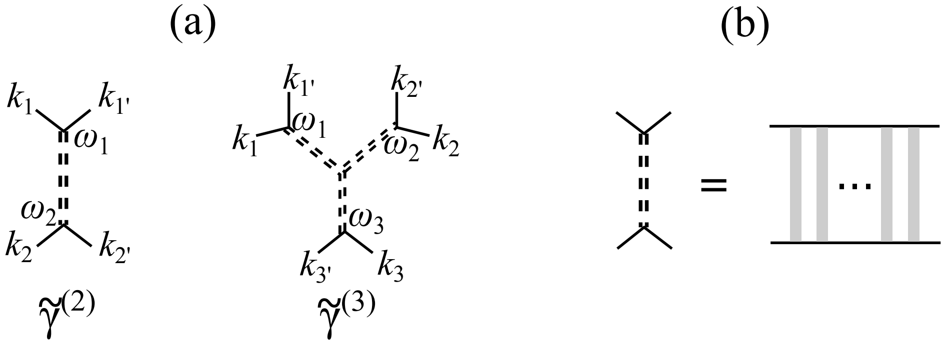

Figure 3.9: (a) Index layout in the locator cumulants. (b) $\tilde{\gamma}^{(2)}$ can be expanded as a local ladder series where the grey stripes are $K^{(2)}$-kernels for the Bethe-Salpeter equation.

Here we choose Δ to be diagonal in the real-space and to also adopt the upper-triangular form of Eq.(2.18). With notations $\mathcal{V} = H_0 - \Delta$ and $g_v = [\omega - \Delta - v]^{-1}$, G_v can be rewritten as $G_v = [g_v^{-1} - \mathcal{V}]^{-1}$. The quantity g_v is thus identified as the locator under a given onsite potential, and Δ_i can hence be interpreted as a self-energy that encodes the coupling between the ith site and its surrounding environment.

The disorder-average over G_v is carried out in a similar manner as in Sec.2.2.1: we first expand it as $G_v = g_v + g_v\mathcal{V}g_v + g_v\mathcal{V}g_v\mathcal{V}g_v + \cdots$, and then take averages on each individual term in the series. The result can be visualized by the diagrams of Fig.3.8 (cf. Fig.2.2). Similar to Eq.(2.27), here we make use of the locator cumulants, which are defined such as

$$\tilde{\gamma}^{(2)} : \ \tilde{\gamma}^{k_1k_{1'}k_2k_{2'}}_{i\omega_1\omega_2} = g^{k_1k_{1'}k_2k_{2'}}_{i\omega_1\omega_2} - g^{k_1k_{1'}}_{i\omega_1} g^{k_2k_{2'}}_{i\omega_2}, \tag{3.16a}$$

$$\begin{aligned}\tilde{\gamma}^{(3)} : \ \tilde{\gamma}^{k_1k_{1'}k_2k_{2'}k_3k_{3'}}_{i\omega_1\omega_2\omega_3} &= g^{k_1k_{1'}k_2k_{2'}k_3k_{3'}}_{i\omega_1\omega_2\omega_3} - g^{k_1k_{1'}}_{i\omega_1} g^{k_2k_{2'}k_3k_{3'}}_{i\omega_2\omega_3} - g^{k_2k_{2'}}_{i\omega_2} g^{k_1k_{1'}k_3k_{3'}}_{i\omega_1\omega_3} - g^{k_3k_{3'}}_{i\omega_3} g^{k_1k_{1'}k_2k_{2'}}_{i\omega_1\omega_2} \\ &+ 2g^{k_1k_{1'}}_{i\omega_1} g^{k_2k_{2'}}_{i\omega_2} g^{k_3k_{3'}}_{i\omega_3},\end{aligned} \tag{3.16b}$$

where k is a binary index corresponding to the two-by-two matrix structure of Eq.(2.18). Diagrammatically $\tilde{\gamma}^{(n)}$ can be represented by a vertex with n "legs"; each leg is attached with two k indices and one frequency, as illustrated in Fig.3.9. Given the value of Δ at the ith site, the disorder-averaged locators g_i are computed as follows:

$$g_{i\omega}^{k_1k_{1'}} = \overline{[\omega - v_i - \Delta_i(\omega)]^{-1}_{k_1k_{1'}}} = \begin{bmatrix} \overline{(\omega - v_i - \Delta_i^{\mathrm{R}})^{-1}} & \overline{(\omega - v_i - \Delta_i^{\mathrm{R}})^{-1}\Delta_i^{<}(\omega - v_i - \Delta_i^{\mathrm{A}})^{-1}} \\ 0 & \overline{(\omega - v_i - \Delta_i^{\mathrm{A}})^{-1}} \end{bmatrix}, \tag{3.17a}$$

$$g_{i\omega_1\omega_2}^{k_1k_1'k_2k_2'} = \overline{[\omega_1 - v_i - \Delta_i(\omega_1)]^{-1}_{k_1k_1'}\,[\omega_2 - v_i - \Delta_i(\omega_2)]^{-1}_{k_2k_2'}}, \tag{3.17b}$$

where the average is individually taken over the random potential v_i at each site.

Formally the exact disorder-averaged Green's function can be obtained by summing up the diagram series of Fig.3.8 under any Δ. However, since in practice the diagram series is always subject to truncations, the value of Δ needs be uniquely determined by the computational scheme, for otherwise the value of the incomplete diagrams would acquire a Δ-dependence. To address this problem, we notice that in the locator formalism one actually has two ways to obtain the Green's function at a single site: either using the locator g_i or taking the diagonal of the global Green's function G_{ii}. It would only make sense if $g_i = G_{ii}$. This condition will thus be used to determine Δ in both the coherent potential approximation (CPA) and the dual fermion (DF) method to be introduced below.

3.3.1 Coherent potential approximation

CPA was first introduced by Soven [68] and Taylor [69] in the propagator formalism using the T-matrix expansion technique. Its equivalent locator representation was later completed by Leath [70]. Whereas the original objective of CPA was to compute the equilibrium electronic structures of alloys, its underlying idea was leveraged by Velický [57] who formulated a theory to calculate the disorder-average two-particle Green's function so that the linear transport coefficients could be accessed. It turns out that Velický's single-site T-matrix approach and the diagrammatic approach of Sec.2.2.2 eventually lead to the same result under CPA [1]. CPA has continued attracting attentions along with the expanding applications of *ab initio* materials simulations [71–73]. The generalization of CPA to nonequilibrium mesoscopic transport was derived by Runge *et al.*[74] and Ke *et al.*[62] independently. In particular, Ke *et al.* integrated this nonequilibrium theory into an *ab initio* simulator applicable to arbitrary device structures. The parallel locator version of nonequilibrium CPA was later given by Zhu *et al.*[58].

Using the locator language, CPA consists in neglecting all the diagrams which involve cumulants. In other words, the only terms to retain in CPA are $g + g\mathcal{V}g + g\mathcal{V}g\mathcal{V}g + \cdots$, where g is the average locator defined in Eq.(3.17a). As such the global disorder-averaged Green's function is approximated by $G = [g^{-1} - \mathcal{V}]^{-1}$. The CPA algorithm can be summarized by the following equations:

$$g_i = \overline{(\omega - v_i - \Delta_i)^{-1}}, \tag{3.18a}$$

$$G = [g^{-1} - \mathcal{V}]^{-1}, \tag{3.18b}$$

$$G_{ii} = g_i, \tag{3.18c}$$

where every variable should be understood as a two-by-two matrix complying with Eq.(2.18). The difficulty in solving the above equations is two-fold. Firstly, due to their nonlinearity, in general it is impossible to write down a closed-form solution for this set of equations. Therefore, one often seeks a numeric solution by using an iterative algorithm. A second difficulty lies in the asymmetric relation between Δ and g, namely g can be readily computed given Δ but not the other way around. This is fatal to the iterative algorithm because it needs a map from g back to Δ in order to close the loop. To overcome this second difficulty, an intermediate variable Σ (diagonal) is introduced such that $\Sigma_i = \omega - \Delta_i - g_i^{-1}$, i.e.

$$\begin{bmatrix} \Sigma_i^{\mathrm{R}} & \Sigma_i^{<} \\ 0 & \Sigma_i^{\mathrm{A}} \end{bmatrix} = \begin{bmatrix} \omega - \Delta_i^{\mathrm{R}} - 1/g_i^{\mathrm{R}} & g_i^{<}/(g_i^{\mathrm{R}} g_i^{\mathrm{A}}) - \Delta_i^{<} \\ 0 & \omega - \Delta_i^{\mathrm{A}} - 1/g_i^{\mathrm{A}} \end{bmatrix} \tag{3.19}$$

Hence the CPA equations can be reformulated as [58]

$$\Delta_i^{\mathrm{R}} = \omega - \Sigma_i^{\mathrm{R}} - 1/G_{ii}^{\mathrm{R}}, \tag{3.20a}$$

$$\Sigma_i^{\mathrm{R}} = \omega - \Delta_i^{\mathrm{R}} - 1/\overline{(\omega - v_i - \Delta_i^{\mathrm{R}})^{-1}}, \tag{3.20b}$$

$$G^{\mathrm{R}} = [\omega - H_0^{\mathrm{R}} - \Sigma^{\mathrm{R}}]^{-1}, \tag{3.20c}$$

which concern the retarded part, together with

$$\Delta_i^{<} = G_{ii}^{<}/(G_{ii}^{\mathrm{R}} G_{ii}^{\mathrm{A}}) - \Sigma_i^{<}, \tag{3.21a}$$

$$\Sigma_i^{<} = \overline{(\omega - v_i - \Delta_i^{\mathrm{R}})^{-1} \Delta_i^{<} (\omega - v_i - \Delta_i^{\mathrm{A}})^{-1}}/(G_{ii}^{\mathrm{R}} G_{ii}^{\mathrm{A}}) - \Delta_i^{<}, \tag{3.21b}$$

$$G^{<} = G^{\mathrm{R}}(\Sigma^{<} + H_0^{<})G^{\mathrm{A}}, \tag{3.21c}$$

which concern the lesser part. The three equations concerning the retarded (lesser) part can be solved in an iterative fashion starting from an initial guess of Σ^{R} ($\Sigma^{<}$). The solution is obtained once a numeric convergence is reached.

Whereas the object Σ was introduced in Eq.(3.19) merely as an auxiliary variable, comparing Eqs. (3.20c) and (3.21c) to Eq.(2.70) we see that Σ seems to play a role of self-energy in the context of disorder-average. To justify this interpretation and to better understand CPA, we seek a diagrammatic representation of Σ in terms of the formalism established in Sec.2.2. To this end we expand the right-hand side of Eq.(3.17a) with respect to v_i taking $(\omega - \Delta_i)^{-1}$ as the reference Green's function. This yields visually the same series of diagrams as in Fig.2.2 when average is taken over v_i. However, here all the spatial indices should be restricted on the site i. This diagram series therefore amounts to the following self-consistent quantity:

$$g_i = (\omega - \Delta_i - \Sigma_{\text{loc}}(g_i))^{-1}, \tag{3.22}$$

where Σ_{loc} consists of all the irreducible diagrams of Fig.2.2 restricted on one single site. These diagrams are certainly derivable from the Luttinger-Ward Φ-diagrams as they share the same diagrammatic topologies with the exact ones.

Comparing Eq.(3.22) to Eq.(3.19), one easily identifies Σ_{loc} with Σ_i. Suppose Δ_i can be eliminated from Eq.(3.22) by using Eq.(3.17a); we are then left with a relation between g_i and Σ_{loc}, which basically defines the function $\Sigma_{\text{loc}}(g_i)$. Therefore, we not only have found the diagram series for the CPA self-energy, but also have established its functional relation to the local Green's function through the intermediate parameter Δ_i. Furthermore, since in CPA the Δ_i is tuned so that $g_i = G_{ii}$, one gets $G = [\omega - \Sigma_{\text{loc}}(G_{ii}) - H_0]^{-1}$ which fulfills the self-consistent condition of Eq.(2.29). Hence CPA complies with the Kadanoff-Baym theory and thus bears all the conserving properties.

As the CPA self-energy is exact for the one-particle locator, its derivative $\partial\Sigma/\partial g$ should yield the exact $K^{(2)}$-kernel for the two-particle locator when plugged into the Bethe-Salpeter equation Eq.(2.31). Here we study the case when $k_1 = k_{1'} = 1$ and $k_2 = k_{2'} = 2$ in Eq.(3.17b). The locator thus obtained is denoted by $g^{\text{RA}}_{i\omega} = \overline{(\omega - v_i - \Delta^{\text{R}}_i)^{-1}(\omega - v_i - \Delta^{\text{A}}_i)^{-1}}$. Inserting $g^{\text{RA}}_{i\omega}$ into Eq.(2.31), we obtain the kernel

$$K^{\text{RA}}_i = 1/(g^{\text{R}}_i g^{\text{A}}_i) - 1/g^{\text{RA}}_i. \tag{3.23}$$

In what follows we shall prove that the CPA self-energy and K^{RA}_i satisfy the identity (2.60), as required by theoretical consistency. To this end we use the definition of locators to get

$$\begin{aligned} g^{\text{R}}_i - g^{\text{A}}_i &= \overline{(\omega - v_i - \Delta^{\text{R}}_i)^{-1} - (\omega - v_i - \Delta^{\text{A}}_i)^{-1}} \\ &= (\Delta^{\text{R}}_i - \Delta^{\text{A}}_i)\overline{(\omega - v_i - \Delta^{\text{R}}_i)^{-1}(\omega - v_i - \Delta^{\text{A}}_i)^{-1}} = (\Delta^{\text{R}}_i - \Delta^{\text{A}}_i) g^{\text{RA}}_i. \end{aligned} \tag{3.24}$$

We then substitute $(\Sigma^{\text{A}}_i + 1/g^{\text{A}}_i - \Sigma^{\text{R}}_i - 1/g^{\text{R}}_i)$ for $(\Delta^{\text{R}}_i - \Delta^{\text{A}}_i)$ above. After some rearrangement, Eq.(3.24) gives $1/(g^{\text{R}}_i g^{\text{A}}_i) - 1/g^{\text{RA}}_i = (\Sigma^{\text{R}}_i - \Sigma^{\text{A}}_i)/(g^{\text{R}}_i - g^{\text{A}}_i)$, which equals K^{RA}_i in view of Eq.(3.23). Therefore, Σ_i and K^{RA}_i satisfy the identity (2.60) at $n = 2$.

Using the notation of $g^{\text{RA}}_{i\omega}$, we rewrite Eq.(3.21b) as

$$\Sigma^{<}_i = \Delta^{<}_i g^{\text{RA}}_i [1/(g^{\text{R}}_i g^{\text{A}}_i) - 1/g^{\text{RA}}_i]. \tag{3.25}$$

Using the relation $\Delta_i^< g_i^{\mathrm{RA}} = g_i^<$ from Eq.(3.17a) and recognizing the quantity in the square bracket as K_i^{RA}, we get $\Sigma_i^< = K_i^{\mathrm{RA}} G_i^<$. Substituting this relation into Eq.(3.21c) and letting $H_0^< = \Sigma_{\mathrm{LR}}^<$, we arrive at a recursive equation for $G_i^<$ of the same structure as Eq.(3.6), with $\gamma_i^{(2)}$ replaced by K_i^{RA}. As K_i^{RA} is also a local object, we see that the $G_i^<$ under CPA can be expressed with the diffuson and so that CPA in fact leads to a diffusive description of the transport system.

From the discussion above, we see that CPA fits well in both propagator and locator formalisms. On the one hand, the propagator formalism gives a natural picture taking disordered potential as the perturbation, which explains why CPA is accurate in the weak disorder limit. On the other hand, the intersite hopping becomes negligible in the strong limit of binary disorder [48], and thus CPA simply yields the locators at each site, which produce the split bandstructure featured by localized electronic systems. Therefore, the perturbation expansion with respect to either disordered potential or intersite hopping turns out fairly effective under CPA. What's more, the locator formulation also reveals the mean-field nature in CPA: the Δ_i quantity plays the role of an effective field akin to the Weiss field in the classical context of Ising model [75]. More precisely, CPA belongs to a category of *dynamical* mean-fields in that the local quantum fluctuations are fully taken into account by the frequency dependent locators. In practice the performance of CPA drops as the system dimension decreases [48]. This is in fact a common feature of mean-field theories with a short-range coupling between local degrees of freedom. As there are less neighbors at lower dimensions, the importance of spatial fluctuations rises and leads to an increasing demand of going beyond mean-field approximations [76]. With this motivation, we introduce in the following the dual fermion method, which computes a perturbation correction to CPA by taking into account more diagrams from the series of Fig.3.8.

3.3.2 Dual fermion method

The dual fermion (DF) method was recently introduced by Rubtsov *et al.* in the context of strongly correlated fermions on the Hubbard lattice [77, 78].[3] Its original usage was for correcting the dynamical mean-field solution [75] of electronic structure by incorporating nonlocal fluctuations on all length scales. Later on, Terletska *et al.*[82] adapted the DF theory to the disorder-averaging problem for equilibrium lattices, and remarkable improvements over CPA were obtained in the results of one-particle density of states and linear response conductivities. With the continuous development during recent years, the DF technique has also been utilized to facilitate other theo-

---

[3] In fact, even before the term "dual fermion" was coined, its mathematical foundation, i.e. the Hubbard-Stratonovich transformation, had already been applied to the Hubbard model and other many-body systems in several works [79–81].

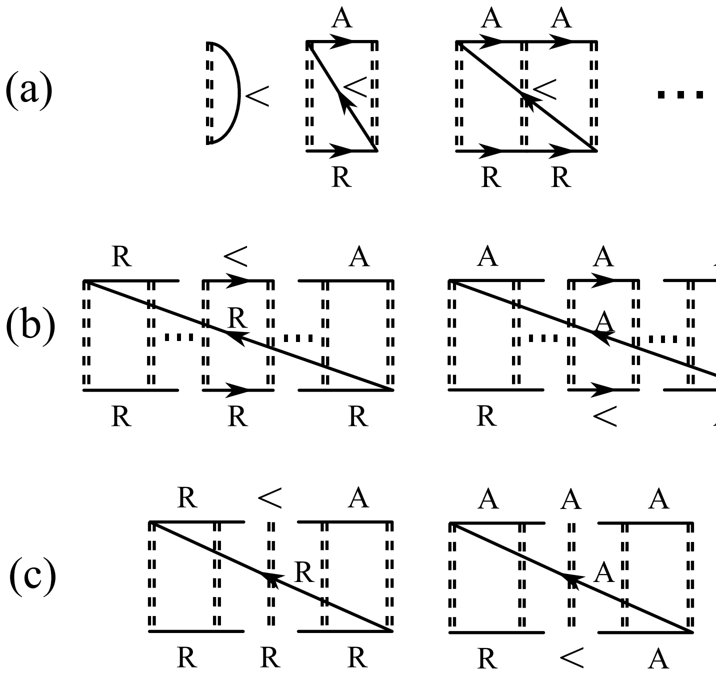

Figure 3.10: Diagrams for the dual lesser self-energy $\tilde{\Sigma}^{<}$. Solid lines represent dual Green's functions $\tilde{G}$ and double dashed lines are cumulants $\tilde{\gamma}^{(2)}$. These diagrams are divided into three groups according to the position of $\tilde{G}^{<}$. Note that in (c) $\tilde{G}^{<}$ is nested inside a vertex $\tilde{\gamma}^{(2)}$.

retical problems of great importance, such as the Kondo quantum dot [83], the phase diagram of the equilibrium Anderson-Hubbard model [84], etc.

Whereas the DF theory was originally formulated in the path-integral language [77, 82], when restricted to the noninteracting disordered system, the theory simply reduces to a diagrammatic resummation scheme in terms of the locators.[4] Our objective here is to sum up all the diagrams of Fig.3.8 which bear the maximally crossing structure as demonstrated in Fig.3.6(b). To this end we choose the diagrams as presented in Fig.3.10, which are one-particle irreducible in the locator formalism. The solid lines therein should represent

$$\tilde{G}_0 = (\mathcal{V}^{-1} - g)^{-1}, \tag{3.26}$$

which we call the reference DF Green's function. Note that $\tilde{G}_0$ absorbs all the dangling g-locators in the diagrams. Analogous to the theory as presented in Sec.2.2.1, we can take the diagrams of Fig.3.10 as a self-energy $\tilde{\Sigma}$ and require it to be self-consistent with the DF Green's function [cf. Eq.(2.70)]:

$$\tilde{G}^{\mathrm{R}} = \left[(\mathcal{V}^{\mathrm{R}})^{-1} - g^{\mathrm{R}} - \tilde{\Sigma}^{\mathrm{R}} \right]^{-1} \tag{3.27a}$$

---

[4] A formal correspondence between the dual fermion theory and the more ancient linked cluster formalism has been discussed in Ref.[85].

$$\tilde{G}^{<} = (1+\tilde{G}^{\mathrm{R}}\tilde{\Sigma}^{\mathrm{R}})\tilde{G}_0^{<}(1+\tilde{\Sigma}^{\mathrm{A}}\tilde{G}^{\mathrm{A}}) + \tilde{G}^{\mathrm{R}}\tilde{\Sigma}^{<}\tilde{G}^{\mathrm{A}}. \tag{3.27b}$$

In order to write down the expression of $\tilde{\Sigma}$, we first define the following ladder notation:

$$\mathcal{L}^{\mathrm{XY}} = \tilde{\gamma}^{\mathrm{XY}} + \tilde{\gamma}^{\mathrm{XY}}(\tilde{G}^{\mathrm{X}}_{\omega} \bullet \tilde{G}^{\mathrm{Y}}_{\omega})\mathcal{L}^{\mathrm{XY}}, \tag{3.28}$$

where $\bullet$ represents the element-wise multiplication (in the real-space), and X and Y are either R or A. To illustrate, the notation $\tilde{\gamma}^{\mathrm{RA}}$ would refer to the case that Eq.(3.16a) is computed under $k_1 = k_{1'} = 1$ and $k_2 = k_{2'} = 2$. Using the notation $\mathcal{L}^{\mathrm{XY}}$, the retarded dual self-energy can hence be written as

$$\tilde{\Sigma}^{\mathrm{R}} = \mathcal{L}^{\mathrm{RR}} \bullet [\tilde{G}^{\mathrm{R}}]^{\mathrm{T}}, \tag{3.29}$$

where "T" denotes matrix transpose. For $\tilde{\Sigma}^{<}$ one needs to apply the $\mathrm{R} < \mathrm{A}$ pattern as explained in Sec.2.1.2, and thus $\tilde{\Sigma}^{<}$ equals the sum of the following three parts (also see Fig.3.10):

$$(\mathrm{a}) = \mathcal{L}^{\mathrm{RA}} \bullet [\tilde{G}^{<}]^{\mathrm{T}}, \tag{3.30a}$$

$$(\mathrm{b}) = \Big[\mathcal{L}^{\mathrm{RR}}(\tilde{G}^{\mathrm{R}} \bullet \tilde{G}^{<})\mathcal{L}^{\mathrm{RA}}\Big] \bullet [\tilde{G}^{\mathrm{R}}]^{\mathrm{T}} + \Big[\mathcal{L}^{\mathrm{RA}}(\tilde{G}^{\mathrm{A}} \bullet \tilde{G}^{<})\mathcal{L}^{\mathrm{AA}}\Big] \bullet [\tilde{G}^{\mathrm{A}}]^{\mathrm{T}}, \tag{3.30b}$$

$$\begin{aligned}(\mathrm{c}) = &\Big\{[\mathcal{L}^{\mathrm{RA}}(\tilde{G}^{\mathrm{R}} \bullet \tilde{G}^{\mathrm{A}}) + 1]\tilde{\gamma}^{<\mathrm{A}}[1 + (\tilde{G}^{\mathrm{A}} \bullet \tilde{G}^{\mathrm{A}})\mathcal{L}^{\mathrm{AA}}]\Big\} \bullet [\tilde{G}^{\mathrm{A}}]^{\mathrm{T}} \\ &+ \Big\{[\mathcal{L}^{\mathrm{RR}}(\tilde{G}^{\mathrm{R}} \bullet \tilde{G}^{\mathrm{R}}) + 1]\tilde{\gamma}^{\mathrm{R}<}[1 + (\tilde{G}^{\mathrm{R}} \bullet \tilde{G}^{\mathrm{A}})\mathcal{L}^{\mathrm{RA}}]\Big\} \bullet [\tilde{G}^{\mathrm{R}}]^{\mathrm{T}}.\end{aligned} \tag{3.30c}$$

Since in terms of the diagrammatics $\tilde{G}$ is terminated with $\mathcal{V}$ at either end while the original Green's function G is terminated with g, a simple relation between $\tilde{G}$ and G follows:

$$G = \mathcal{V}^{-1}\tilde{G}\mathcal{V}^{-1} - \mathcal{V}^{-1}. \tag{3.31}$$

The flowchart of a DF calculation is presented in Fig.3.11. The program consists of two self-consistent loops. The outer one concerns the agreement between the local Green's functions, i.e. $G_{ii} = g_i$, same as in CPA. This consistency is achieved by adjusting Δ_i. The inner loop calculates a self-consistent pair of the dual Green's function and the self-energy under a given Δ_i. The whole algorithm starts with an initial guess of Δ_i and computes the locators using Eq.(3.17), together with the local self-energy Σ_i [via Eq.(3.19)] and cumulant $\tilde{\gamma}^{(2)}$ [via Eq.(3.16a)]. Then the reference Green's function $\tilde{G}_0$ is computed via Eq.(3.26) and is inserted in the dual self-energy diagrams [see Eqs. (3.29) and (3.30)]. The computed $\tilde{\Sigma}$ is plugged into Eq.(3.27) to generate a dual Green's function $\tilde{G}$, which is then plugged back into the diagrams of Fig.3.10. This process is iterated until both $\tilde{G}$ and $\tilde{\Sigma}$ converge. The converged $\tilde{G}$ is then converted to the Green's function G in the original lattice space by means of Eq.(3.31). At this point, we check whether the real-space diagonal of G meets the criterion $G_{ii} = g_i$ at each site, where g_i is the locator computed at

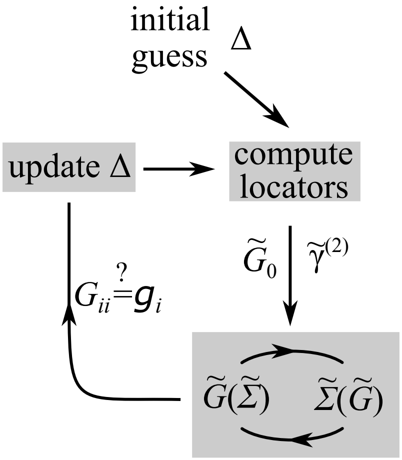

Figure 3.11: Flowchart of the dual fermion computation.

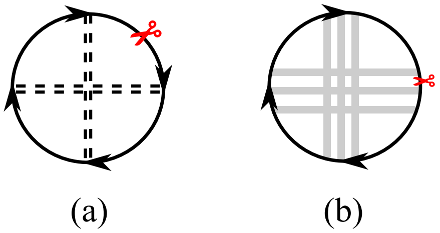

Figure 3.12: (a) A Luttinger-Ward diagram corresponding to the second diagram of Fig.3.10(a). (b) Cutting a Green's function line inside $\tilde{\gamma}^{(2)}$. The grey stripes are $K^{(2)}$-kernels for the ladder-series of $\tilde{\gamma}^{(2)}$.

the beginning of the algorithm. If not, we update Δ_i using Eqs. (3.20a) and (3.21a). The whole procedure is iterated until $G_{ii} = g_i$.[5] Since for noninteracting systems the Green's functions at different energies are decoupled, the above algorithm can be run parallelly over energies.

Before closing this section, we wish to point out that charge conservation is *not* in general guaranteed in the DF method. Although the dual self-energy $\tilde{\Sigma}$ (Fig.3.10) can be derived from a Luttinger-Ward diagram in terms of the dual Green's function $\tilde{G}$, we note that it is the original Green's function G that carries the physical information, and it does not seem to inherit the Φ-derivability through the mapping (3.31). A Luttinger-Ward diagram corresponding to the dual $\tilde{\Sigma}$ is plotted in Fig.3.12(a). Removing one of the solid lines therein leads to the second diagram of Fig.3.10(a). However, since $\tilde{\gamma}^{(2)}$ is defined as the two-particle locator minus the product of two one-particle locators [see Eq.(3.16a)], according to Eq.(2.31) $\tilde{\gamma}^{(2)}$ can be expanded as a ladder series as illustrated in Fig.3.9(b). The Kadanoff-Baym scheme requires that each Green's function in

---

[5] Note that a different self-consistent criterion for choosing Δ was used in the original DF literature [77]. Here we use the same criterion as in CPA, i.e. $G_{ii} = g_i$, because in practice we find it leading to a better charge conserving performance.

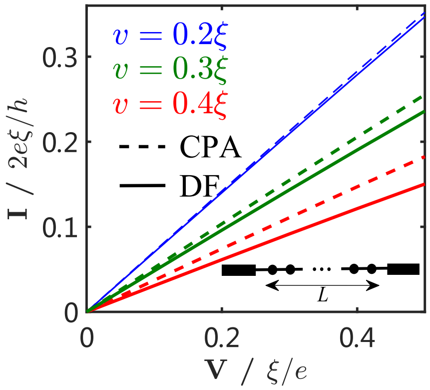

Figure 3.13: $I - V$ relation of a biased one-dimensional chain with $L = 30a, W = 1$. v is the onsite disordered potential. Inset: schematic of the lattice model.

a Luttinger-Ward diagram be deleted one by one in order to obtain the self-energy, but apparently the diagrams of Fig.3.10 miss those generated from cutting Green's functions *inside* the $\tilde{\gamma}^{(2)}$ ladder, as illustrated in Fig.3.12(b). Therefore, the dual self-energy proposed here is incomplete in terms of ensuring charge conversation. In fact, it still remains an open question in the locator formalism as for how to devise conserving approximations based on the diagram expansion technique. In numerical simulations the charge conservation can be investigated by comparing currents computed at different principal layers [see Eq.(2.78)]. When charge is strictly conserved, these currents should be equal. However, in practice we find a (slight) deviation of $< 0.04\%$ among the currents when using the DF method. In particular, the self-consistent conditions as demonstrated in Fig.3.11 are found helpful in reducing the current deviation.

3.4 Numerical studies

The CPA and the DF method are numerically implemented on the discreet lattice described in Sec.2.5.4. Here the e-e interaction is turned off and the temperature is set at zero. To model substitutional disorder, we add a binary random number $\pm v$ to the onsite potential v_i in the scattering region. As discussed above, the DF method does not strictly preserve charge conservation. Therefore, in calculating charge currents, we take the mean over all the principal layers within the central region, i.e. $I = \sum_{l=1}^{N} I_l/N$.

As our first numerical application of this thesis, we compute the $I - V$ curve (Fig.3.13) for a biased one-dimensional chain with $L = 30, W = 1$ using both CPA and DF. The disorder degree is adjusted by varying the v parameter from 0.2ξ to 0.4ξ. We rigidly shift the band structures in

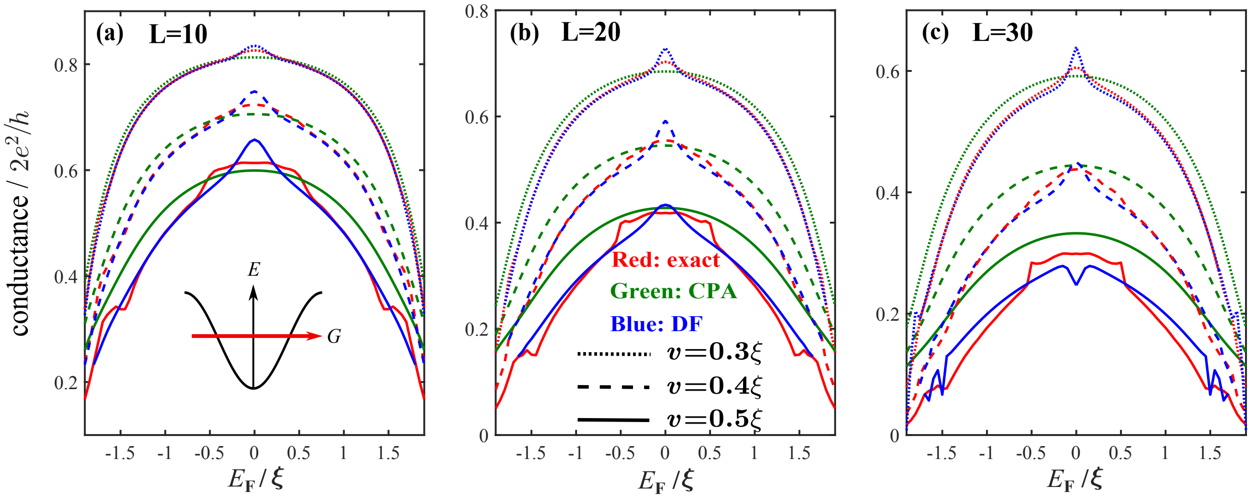

Figure 3.14: Disorder-averaged electronic conductance calculated with different methods: exact (red), CPA (green), and dual fermion (blue). The systems considered here are one-dimensional chains with $W = 1$ and three different L. The disorder strength is adjusted via v. The Fermi energy E_F at which the conductance is calculated is swept from -2.0ξ to 2.0ξ. Some of the blue curves are cut off at certain energies because the DF algorithm tends to diverge around band edges.

the leads according to the applied bias voltage, and assume a linearly dropping electrical potential across the scattering region. The Fermi energy in either lead is fixed at 1.0ξ away from the shifted band center. From Fig.3.13 we see that both CPA and DF predict an ohmic linear $I - V$ relation, but DF yields a lower conductance than CPA and this discrepancy increases with an increasing v.

In order to examine which of the two methods is more accurate, we compute the linear conductance [see Eq.(2.75)] using both CPA and DF, and compare their results with the exact one obtained from a brute-force average over the entire disorder ensemble: the conductance is computed one by one for each of the $2^{W\times L}$ configurations and the mean value is taken at the end. We show in Fig.3.14 the results for a few different structures and disorder strengths (v). Note that the Fermi energy E_F at which the conductance is calculated is swept from -2.0ξ to 2.0ξ. Let us first look at the exact results (red curves). We see that each conductance profile $\mathcal{G}(E)$ can be divided into three characteristic regions: center ($E \in [-v, +v]$), edge ($E \in [-2\xi, -2\xi + v] \cup [2\xi - v, 2\xi]$), and wing ($E \in [-2\xi + v, -v] \cup [v, 2\xi - v]$). The exact result exhibits a bump in the center and a kink on the edge, which becomes especially noticeable when $v > 0.4\xi$. Besides, in the wing region, the exact $\mathcal{G}(E)$ profile appears rather smooth. From the green curves in Fig.3.14, we see CPA yield a smooth and round $\mathcal{G}(E)$ profile across the entire energy window, missing the fine details seen in the exact solution. This is typical for a diffusive approximation, because both the DOS and the classical scattering rate vary smoothly over the energy [12]. Noteworthily, CPA tends to overestimate the conductance in the wing and the edge region, and this overestimation gets more severe as the disorder strength v or the channel length L increases. This finding supports the theoretical analyses in Sec.3.2 and signifies the incompleteness of CPA for not taking into account interfering processes. Since the Cooperon process is most important in one dimension, DF can be expected to effectively correct the CPA result. This is indeed the case as shown by our numerical simulation. As can be seen in Fig.3.14, DF is especially successful in the wing region, where a quantitative agreement with the exact result can be achieved. Besides, DF captures the "bump" at the center of $\mathcal{G}(E)$ profiles, whereas CPA totally misses it. Although the DF method is constructed as a perturbation correction to the diffusive CPA using the same maximally crossing diagrams just as in the weak localization theory presented in Sec.3.2, we believe that, due to the self-consistent loops and the locator reformulation, DF represents more than just the weak localization. For according to the weak localization theory, as L increases the negative correction to the one-dimensional conductance would remain constant [12], which we know untrue since the Anderson transition [86] must set in at some point. On the contrary, Fig.3.14 shows that the correction given by DF grows as L increases, which is more reasonable. Apart from the success achieved by DF, we also notice a performance drop and that the algorithm could even fail to converge in the vicinity of band edges. This is also the region where CPA makes the most overestimation in comparison to the exact result. Invoking the phenomenological picture developed earlier in this chapter, we note that both the Fermi wave vector k_{F} and the mean free path l_0 drop to zero at the band edge (also see Fig.4.1 of Ref.[87]), rendering the weak disorder scenario invalid. It is well known that perturbation-based methods such as DF cannot handle the strong localization, and more sophisticated techniques ought to be employed [88, 89].

In the classical transport theory the conductivity should be a constant in a uniformly doped material, and accordingly the resistance R of a quasi-one-dimensional conductor increases linearly with its length. We would expect this classical relation to stay true for CPA since it essentially describes the diffusive transport. On the other hand, Eq.(3.14) indicates that the quantum conductivity correction due to the weak localization features a L dependence, rendering the $R-L$ relation nonlinear. These predictions are verified by our simulation. Figure 3.15 displays the $R-L$ relations of our disordered lattices under a few different widths W and random potential v. The resistance is calculated as the inverse of disorder-averaged conductance, which is computed with either CPA or DF. The electronic Fermi energies are set at 1.0ξ away from the lowest sub-band edges (see Fig.2.16). We find that the DF method produces a nonlinear $R-L$ relation which can be approximately described by the following formula (also see the logarithmic inset plots in

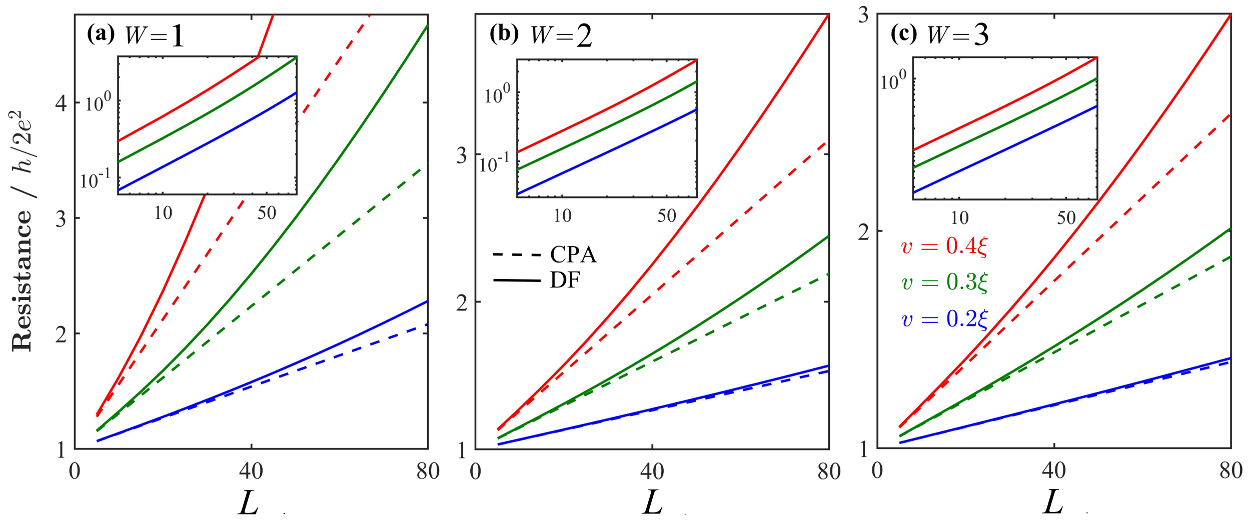

Figure 3.15: $R - L$ relations computed with CPA and DF under a few different widths W and random potential v. The electronic Fermi energies are set at 1.0ξ away from the lowest sub-band edges (see Fig.2.16). Insets: logarithmic plots of the same data.

Fig.3.15):

$$R = R_0 + \frac{\zeta(v)}{W} L^{\alpha}, \tag{3.32}$$

where R_0 stands for the ballistic limit $h/2e^2$, ζ is a function of the disorder strength v, and $\alpha \approx 1.1$. The power-law growth indicated by Eq.(3.32) is a consequence of the use of infinite ladder series in our self-energy construction; had we truncated the series, we would instead obtain a much slower increase in R. Note that in the case of strong localization where L is larger than the localization length [12], $R - L$ should follow a much faster exponential relation [90], which is yet beyond the applicable regime of DF.

As explained in Sec.3.1, the Cooperon process that leads to localization particularly relies on the time reversal trajectories. When a (weak) magnetic field is added perpendicular to the trajectory plane, the time reversal symmetry is broken, and hence one would expect a suppression in the localization effect and a rise in the electric conductance. This phenomenon is termed the negative magnetoresistance in the literature [12]. To simulate this effect we apply a static magnetic field perpendicular to the lattice plane of our model and simply switch our hopping amplitude to the form of Eq.(2.80). Suppose the x and z axes are set parallel to the transport and the magnetic field respectively, the vector potential is thus written $\vec{A} = (By, 0, 0)$. We use a structure of $W = 3, L = 50$ with $v = 0.35\xi$ as the test bed,[6] and apply both DF and CPA to compute its resistance under

---

[6] Note that the magnetic effect cannot be manifested in a strict one-dimensional system, such as $W = 1$, because of the absence of magnetic flux.

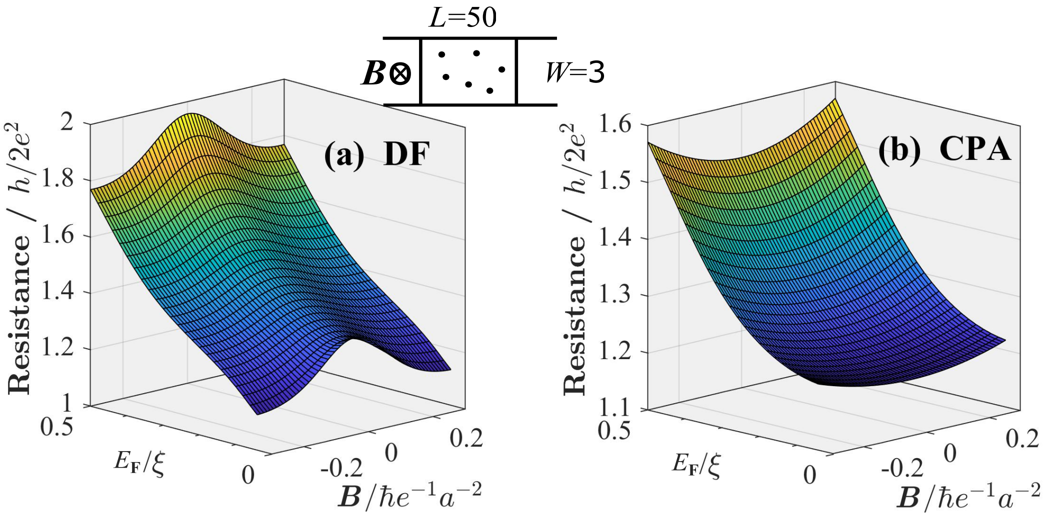

Figure 3.16: Electrical resistance calculated with (a) DF and (b) CPA at different Fermi energies (E_F) in the presence of a perpendicular magnetic field (B). The simulated system is a 3×50 ($W \times L$) square lattice with binary disorder whose strength $v = 0.35\xi$. A sketch of the system setup is displayed at the top.

varying field strength and Fermi energy. The result is displayed in Fig.3.16. As can be clearly seen, DF succeeds in predicting a decreasing resistance as the magnetic field gets stronger, i.e. negative magnetoresistance, whereas CPA predicts an opposite (implausible) tendency.

3.5 Summary

In this chapter we reviewed the mesoscopic transport theory of quantum diffusion and the weak localization correction in disordered systems with randomly distributed scattering centers. The two physical phenomena turn out to be respectively associated with the processes represented by the diffuson (ladder) and the Cooperon (maximally crossing) diagrammatic objects. In order to implement the theories on numerical models, we switched to the locator formalism which does not assume translational symmetry and naturally permits a higher degree of disorder. Using the locator language the coherent potential approximation (CPA) was introduced, which amounts to a local mean-field approximation for the electronic structure and a diffusive description for the transport. We then used the dual fermion (DF) technique to sum up the Cooperon diagrams in the locator series in order to introduce a localization correction on top of CPA. Our simulation results showed that the DF method is indeed effective and more accurate than CPA. In particular, DF captures the nonlocal effects that lead to the localization effect. Notwithstanding its success, the DF method still has a hard time in the strong localization regime, which is in fact ubiquitous for all perturbation-based methods. Analogous to the strong correlation problem of interacting fermions, renormalization techniques [88] should be in order for accurately describing the electronic transport subject to strong localizations.

Chapter 4

Energy relaxation due to e-e interaction

The electron-electron (e-e) interaction is an effect one must take notice of when discussing many-electron systems. Different from the scattering off static impurities, e-e interaction is intrinsic to any many-electron systems. By convention, effects of e-e interaction are divided into three parts: Hartree, Fock (exchange), and correlation. As already explained in Sec.2.3.1, the Hartree represents the simplest interaction effect, i.e. the electric mean-field set up by the charge distribution in the system; therefore it is classical. In terms of the diagrammatics formulated in Sec.2.3.1, the Hartree effect corresponds to the diagram of Fig.2.10(a). The effect derived from Fig.2.10(b) is termed the Fock (exchange) effect. Though not obvious from the diagram, the physical origin of the exchange effect is in fact the celebrated Pauli exclusion principle of identical particles. Translating Fig.2.10(b) into its mathematical formula, we get the following self-energy for the exchange effect:

$$\Sigma^{\mathrm{R}}_{\mathrm{X}}(\mathbf{r}_1, \mathbf{r}_2) = \mathrm{i}U(\mathbf{r}_1, \mathbf{r}_2) \int G^{<}(\mathbf{r}_1, \mathbf{r}_2, \varepsilon) \frac{d\varepsilon}{2\pi} \tag{4.1}$$

As can be readily seen, the exchange self-energy is energy independent and thus can be regarded as a hermitian correction to the non-interacting Hamiltonian.[1] Since both Hartree and Fock self-energies are hermitian, they can be used, in conjunction with the non-interacting Hamiltonian, to set a reference electronic structure of the interacting system, which is composed of well-defined energy-eigenstates.

The rest of the (infinite number of) diagrams generated by the Hedin equation thus constitute the so-called correlation effect, which is separated from Hartree and Fock in that its self-energies are non-hermitian, energy dependent, and hence cannot be written in a mean-field form. The concept of correlation encompasses a broad spectrum of many-body effects, from the elementary e-e scattering process which fits in the perturbation framework and on which we shall focus in this

---

[1] Note that the exchange self-energy acquires spin-dependence in a spin-nondegenerate system.

chapter, to strongly correlated matters such as the Mott insulator, for which the theoretical tools developed in this thesis do not suffice.

As correlation effects generally cannot be expressed in closed forms, the typical methodology is classifying them by their particular many-body phase and using certain representative model as basis to capture the main physics of the corresponding system. One celebrated theoretical model on this aspect is the Fermi liquid (attributed to Landau), which has gained great success in describing normal metals with a simple Fermi surface. Low-energy (compared to the Fermi energy) excitations in a Fermi liquid are represented by the creation or annihilation of *nearly independent* quasiparticles, whose life-time (i.e. inverse energy uncertainty) is much longer than the time scale of external perturbations [6]. A quasiparticle state is not an exact eigenstate of the interacting system. Rather, it must be understood as a superposition of states with energies confined in a finite range inverse to its life-time. The proper way to introduce the quasiparticle concept is via the renormalization procedure [6, 91–93], which yields an effective Hamiltonian for the original system at a desired energy scale. Parameters such as the particle mass and the interaction strength would be redefined as a result of renormalization. As can be anticipated, the renormalized interaction would typically be weaker than in the original system, thus rendering the new model dominated by its quadratic part, which defines the underpinning quasiparticle spectrum. It is at this point that one may feel safer applying the perturbation technique.[2] Therefore, when interpreting the results presented in this chapter, one should bear in mind that the system we are looking at is assumed to bear the Fermi liquid nature at the background.

As the system we study in this thesis is the quantum wire, it should be mentioned that the Fermi liquid formalism is believed to break down in strict one-dimension, where the electrons occupy the lowest sub-band only. The reason for the breakdown lies in the particular "nested Fermi surface" feature of the one-dimensional system, which renders its low-energy excitations all governed by certain collective modes (i.e. charge or spin density waves) instead of individual quasiparticles [6, 94]. This phase of matter is referred to as the Luttinger liquid in the literature. It is usually described using the bosonization procedure [94], which is by no means covered by this thesis. However, we notice that the condition for building up a system featuring the phase of Luttinger liquid is demanding. In particular it requires a sufficiently long piece of wire, which is typically on the scale of micrometers [95, 96]. Therefore, in order to justify using Fermi-liquid as the base here, we assume our model system is too short to host a Luttinger liquid.[3] Besides we note that the

---

[2] Although the renormalized Hamiltonian dismisses the original bare electrons and relies on the introduced quasiparticles, it should in principle contain as much information in terms of the physical observables.

[3] The breakdown of Fermi-liquid in one-dimension can be diagnosed by calculating the polarization P of the noninteracting 1D Fermion gas. One finds that P would diverge in the long wavelength and low frequency limit [97].

electrodes to which the wire is coupled should always be regarded as Fermi-liquid reservoirs.

The e-e interaction as a perturbation is responsible for two particular physical effects in disordered mesoscopic conductors, i.e. dephasing and energy relaxation. The dephasing effect is usually associated with the Cooperon process as discussed in Chapter 3. As explained there, the enhanced return probability of electrons due to Cooperon relies on the phase alignment between time-reversal trajectories. This phase alignment retains in the presence of a *static* electric field but is not robust against a dynamically fluctuating field [12]. In the presence of e-e interaction, an intrinsic dynamic field can be induced due to the screening effect among interacting electrons and thus impacts the Cooperon process [23]. Nevertheless, this effect amounts to a correction to transport coefficients that is subleading to the weak localization and the Altshuler-Aronov effect (see chapters 3 and 5 respectively), and thus it is not discussed in this thesis.

The energy relaxation is a more general phenomenon which simply arises from the energy exchange during the e-e interaction process. Since e-e interaction alone conserves both the total momentum and the energy of the system, the energy relaxation effect is best manifested in the single-particle (energy) distribution function rather than in transport coefficients. An important aspect of energy relaxation in mesoscopic conductors is that the electrons injected from the out-of-equilibrium reservoirs have a tendency of equilibration in the interacting region. In particular this effect leads to an energy distribution of the particle occupation that is fundamentally different from the noninteracting case, showing the nonequilibrium electrons' efforts to equilibrate. What's more, the equilibration process could become collaborative when there are other wires placed nearby, even if the e-e interaction is the only way for these wires to "cross-talk". Interestingly the equilibration in one nonequilibrium wire can be facilitated at the price of driving others out of equilibrium. These physical effects and the associated theoretical formalism are what this chapter is devoted to.

4.1 The *GW* method

In order to derive a practical numerical scheme we simplify the Hedin formalism (see Sec.2.3.1) by neglecting the vertex correction Λ_{ee} (see Fig.2.9). The resulting approximate self-energy thus reads

$$\Sigma_{\mathrm{ee}}(1,2) \simeq \mathrm{i}G(1,2)W(1,2). \tag{4.2}$$

The polarization involved in the calculation of the screened e-e interaction W is accordingly approximated as

$$P(1,2) \simeq -\mathrm{i}G(1,2)G(2,1^{+}). \tag{4.3}$$

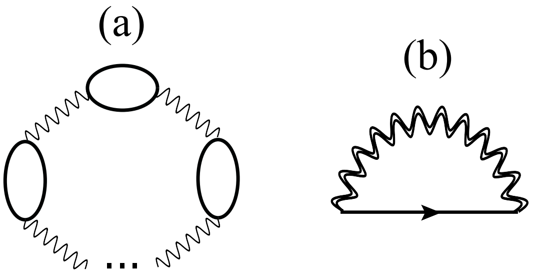

Figure 4.1: (a) Φ-diagram and (b) self-energy under the GW approximation. The double-wiggle line represents the screened e-e interaction W, see Fig.2.9.

We hence obtain a closed set of (simplified) Hedin equations which can be solved numerically. The resulting formalism was coined the GW approximation [33] as its self-energy has the form of Eq.(4.2). As can be seen from Fig.4.1, the GW self-energy is obviously Φ-derivable and is thus suitable for transport calculations where a set of conservation properties are desired [55]. Although the GW theory was originally proposed for metallic systems of a high electron density, in practice it often shows a fair versatility for other systems such as semiconductors [98] and molecular transport junctions [99]. Overall the GW method is a good compromise between the physical accuracy and computational efforts. In the following we present in detail the numerical procedure of our transport calculation that involves both e-e and e-impurity scattering.

As per Eq.(2.70) we first write down the Green's functions in the scattering region with the discrete basis set:

$$G^{\mathrm{R}}(\omega) = \left[\omega I_{N\times N} - H - \Sigma^{\mathrm{R}}_{\mathrm{LR}} - \Sigma^{\mathrm{R}}_{\mathrm{H}} - \Sigma^{\mathrm{R}}_{\mathrm{X}} - \Sigma^{\mathrm{R}}_{\mathrm{C}} - \Sigma^{\mathrm{R}}_{\mathrm{CPA}}\right]^{-1}, \tag{4.4a}$$

$$G^{<}(\omega) = G^{\mathrm{R}}\left[\Sigma^{<}_{\mathrm{LR}} + \Sigma^{<}_{\mathrm{C}} + \Sigma^{<}_{\mathrm{CPA}}\right] G^{\mathrm{R}\dagger}, \tag{4.4b}$$

where H is the Hamiltonian within the central scattering region, Σ_{LR} denotes the total lead self-energy, Σ_{H} denotes the classical Hartree potential, Σ_{X} denotes the exchange self-energy [see Eq.(4.1)], Σ_{C} is the correlation self-energy approximated in the form of Eq.(4.2), and Σ_{CPA} is the disorder-induced self-energy to be computed by the coherent potential approximation (CPA, see chapter 3). Note that only H, Σ_{H}, and Σ_{X} are Hermitian and ω-independent.

To calculate Σ_{C} we need first the polarization which is expressed as

$$P^{</>}_{ij}(\omega) = -2\mathrm{i}\int \frac{d\omega'}{2\pi} G^{</>}_{ij}(\omega+\omega')\, G^{>/<}_{ji}(\omega'), \tag{4.5a}$$

$$P^{</>}_{ij}(t) = -2\mathrm{i} G^{</>}_{ij}(t) G^{>/<}_{ji}(-t), \tag{4.5b}$$

in the frequency and time domains respectively. Using the Kramers-Kronig relation [55], the

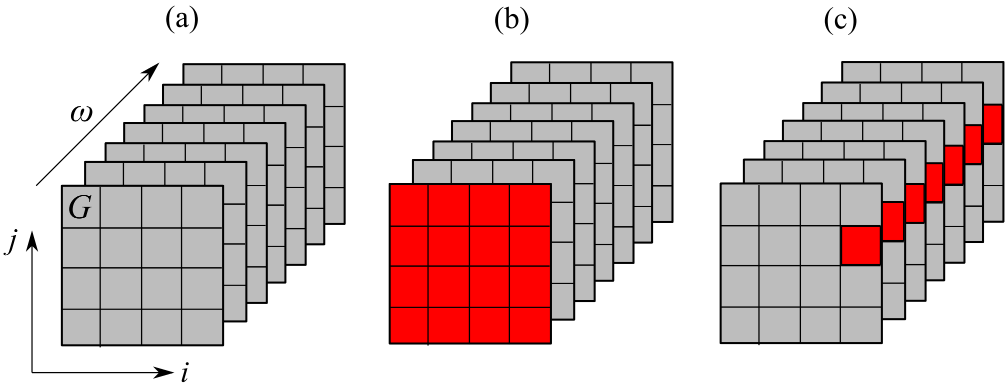

Figure 4.2: The Green's function and other intermediate variables (i.e. P, W, Σ) are stored as 3D-arrays in our numerical program, the third dimension being the frequency ω. (b): slicing view at a given ω. (c): slicing view at a given pair of real-space indices ij. The numerical program is parallelized as per either of the two views.

retarded component is obtained from

$$P_{ij}^{\mathrm{R}}(\omega) = \mathrm{i}\int \frac{d\omega'}{2\pi}\frac{P_{ij}^{>}(\omega') - P_{ij}^{<}(\omega')}{\omega - \omega' + i0^{+}}, \tag{4.6a}$$

$$P_{ij}^{\mathrm{R}}(t) = \Theta(t)\left[P_{ij}^{>}(t) - P_{ij}^{<}(t)\right], \tag{4.6b}$$

where Θ denotes the Heaviside step function. The polarization is computed with the Fourier transform approach [55]. The Green's functions $G^{</>}$ obtained in the frequency domain (see Fig.4.2b) are Fourier transformed into the time domain (Fig.4.2c), where the computations simply become element-wise products as can be seen from Eq.(4.5b). A brief outline of the numeric Fourier transform technique is given in appendix A. We also employ the zero-padding technique [100] to the frequency series of $G^{</>}(\omega)$ and $P^{</>}(\omega)$ to improve the numeric accuracy. The elongated series for $G^{</>}(\omega)$ are at least four times as long as the original, and for $P^{</>}(\omega)$ a longer padding (six times) is used. The reason for using a longer padding for $P^{</>}(\omega)$, whose Fourier image is used to compute Eq.(4.6b), is that the real part of $P^{\mathrm{R}}(\omega)$ in fact decays very slowly as ω increases. The outcoming numeric value of $\mathrm{Re}P^{\mathrm{R}}(\omega)$ obtained from the above procedure always decays to zero at the two ends of the frequency series. Therefore, if no zero-padding were used, $\mathrm{Re}P^{\mathrm{R}}(\omega)$ could be severely underestimated at large ω.

Using the matrix notation, the screened interaction is expressed as

$$W^{\mathrm{R}}(\omega) = \left[I - UP^{\mathrm{R}}(\omega)\right]^{-1}U, \tag{4.7a}$$

$$W^{</>}(\omega) = W^{\mathrm{R}}(\omega)\,P^{</>}(\omega)\,W^{\mathrm{A}}(\omega), \tag{4.7b}$$

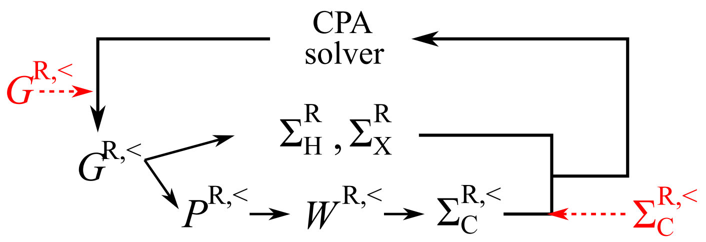

Figure 4.3: Flowchart of the numerical scheme. The main flow is marked by the black arrows. The insertions labeled by dashed arrows represent the mixing operation, which involves the historical results of the corresponding quantity computed during previous iterations. Either the Green's function or the correlation self-energy (Σ_{C}) can be used as the mixing operand. Note that the CPA solver, employed to compute the disorder self-energy, contains a second layer of iteration in itself. This part of algorithm is presented in Sec.3.3.1.

where U is the interaction matrix parameterized as $U_{ij} = ua/|\mathbf{r}_i - \mathbf{r}_j|$. Using the same Fourier transform based method as in Eq.(4.5a), the correlation self-energy is calculated by

$$\Sigma^{</>}_{\mathrm{C},ij}(\omega) = \mathrm{i}\int \frac{d\omega'}{2\pi} G^{</>}_{ij}(\omega-\omega')\, W^{</>}_{ij}(\omega')\,, \tag{4.8a}$$

$$\Sigma^{</>}_{\mathrm{C},ij}(t) = \mathrm{i}G^{</>}_{ij}(t)\, W^{</>}_{ij}(t)\,. \tag{4.8b}$$

The retarded component $\Sigma^{\mathrm{R}}_{\mathrm{C}}$ is again obtained from the Kramers-Kronig relation (4.6b), where P should be replaced by Σ_{C}. Without disorder-average, one can simply insert the computed exchange-correlation self-energies back to Eq.(4.4) and hence closes the set of Hedin equations. However, in order to take into account disorder scattering on an equal footing with the e-e interaction, we need to add an extra step which carries out the self-consistent CPA computation, as illustrated in the flowchart Fig.4.3. During this nested CPA calculation, the exchange-correlation self-energies are put in the H_0 object defined in Eqs. (3.20c) and (3.21c). The resulting coupled CPA-Hedin equation effectively generates an infinite series of diagrams as exemplified in Fig.4.4. Note that all these diagrams are non-crossing in that each diagram block is embedded within another block of higher level: they do not include crossing diagrams such as Fig.2.11(b').

Our numerical program consists in iterating the loop shown in Fig.4.3 until a numerical convergence is reached. We note that the convergence is essential for the conservation properties, as asserted by the Kadanoff-Baym theory. To facilitate this process one could adopt a mixer, whose simplest form reads

$$G^{\mathrm{R},<}(\varepsilon) = \beta G^{\mathrm{R},<}_{\mathrm{out}}(\varepsilon) + (1-\beta) G^{\mathrm{R},<}_{\mathrm{in}}(\varepsilon), \tag{4.9}$$

where G_{in} denotes the input Green's function used to compute the interaction self-energies, and G_{out} denotes the output of the CPA nested iteration which follows the Σ_{C} computation. The left

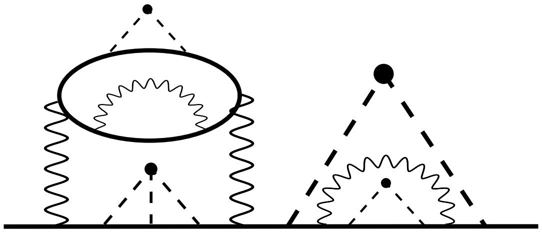

Figure 4.4: Exemplary Green's function diagram generated by the self-consistent scheme as formulated in the main text (also see Fig.4.3).

	G	Σ	P	W
$X^{\mathrm{R}}(\omega) = \left(X^{\mathrm{A}}(\omega)\right)^{\dagger}$	✓	✓	✓	✓
$X^{\mathrm{R}}(\omega) = \left(X^{\mathrm{R}}(-\omega)\right)^{*}$			✓	✓
$X^{</>}(\omega) = -\left(X^{</>}(\omega)\right)^{\dagger}$	✓	✓	✓	✓
$X^{<}(\omega) = -(X^{>}(-\omega))^{*}$			✓	✓

Table 4.1: Symmetry relations. X represents a matrix expressed with real-space basis, which can be G, Σ, P or W. A check mark means that the quantity of the corresponding column satisfies the relation of the corresponding row.

hand side of Eq.(4.9) then becomes the input of the subsequent iteration. Alternatively one can mix the interaction self-energy by using the same formula Eq.(4.9); the major advantage of doing so is that, in comparison with $G^{\mathrm{R},<}$, $\Sigma_{\mathrm{C}}^{\mathrm{R},<}$ is much smoother as a function of energy, thus numerically more stable. In practice the GW scheme presented here converges much more slowly than the disorder solver. To accelerate the convergence, more sophisticated mixers, such as the Pulay algorithm [101, 102] employed in Refs.[3, 55], can be an option. However, we notice that the Pulay algorithm does not always guarantee a convergence. Apart from the mixer, we find it useful to impose the symmetry relations listed in Table.4.1; this helps on the robustness of the iterative program. These symmetry relations regarding G, Σ, P, W can be easily derived from their basic definitions.

4.2 Applications

We implement the numerical method presented above on the discrete lattice model which we established in Sec.2.5.4 and, as applications, we study specifically the energy distribution function of particle occupation and the Coulomb drag effect in nonequilibrium quantum wires.

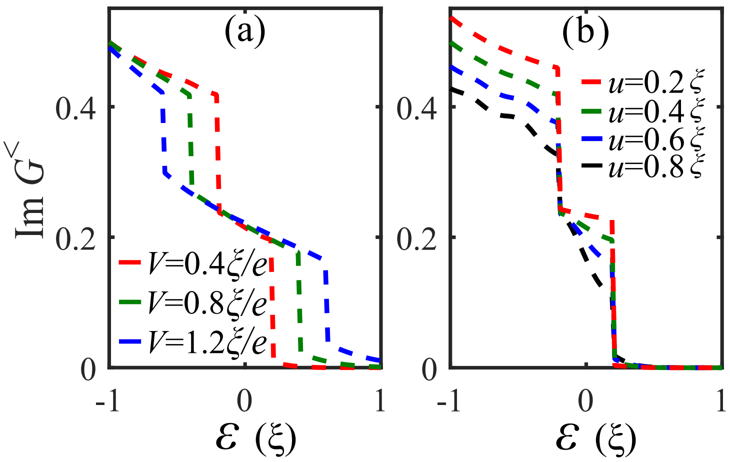

Figure 4.5: Energy distribution of particle occupation at the middle of a nonequilibrium wire ($L = 40a$). The setup of our model is detailed in the main text. Subplots (a) and (b) respectively show the evolution of the energy distribution under different bias and e-e interaction strength u. The results in (a) are obtained under $u = 0.4\xi$

4.2.1 Nonequilibrium energy distribution

In mesoscopic physics the degree of energy relaxation is often measured by a length scale L_{in} which is interpreted as the mean free path between successive *inelastic* e-e scattering events [22]. If $L_{\text{in}} \gg L$, L being the wire length in between electronic reservoirs (leads), electrons could barely have a chance to exchange energy before reaching the reservoirs, and thus the system is effectively noninteracting and nonlinear. In the other limit $L_{\text{in}} \ll L$, the inelastic scattering becomes so frequent that local equilibrium is established on the scale of L_{in} in the wire, and hence the local energy distribution of particle occupation displays an equilibrium profile [14]. In the intermediate range of inelastic scattering, the energy distribution then interpolates between the two limit cases. As the energy distribution of particle occupation is measurable by experiments [14], it is a practical approach to probing the inelastic scattering or the energy relaxation rate of interacting electrons. The numerical method presented in this chapter provides a natural access to this energy distribution function since it can be simply read off from the diagonal of $\text{Im}G^<(\varepsilon)$, according to its definition (2.11). It is worth noting that the self-consistent procedure for computing the correlation self-energy is essential for observing the characteristics of energy relaxation on $\text{Im}G^<(\varepsilon)$ profile; this procedure solves an integral equation equivalent to the more widely used kinetic (differential) equation [14, 44].

To demonstrate we set up a one-dimensional lattice model with $W = 1,\ L = 40a$ (see Fig.2.15). The disorder is modeled by a binary random variable $v = \pm 0.5\xi$, where ξ is the hopping amplitude, and the bare e-e interaction is modeled as $U_{ij} = ua/|x_i - x_j|$, $i \neq j$. The temperature in the leads is set at zero and the chemical potentials are set at the band-structure center. When a voltage is applied to the lead, accordingly its band-structure, together with the chemical potential, gets shifted in a rigid manner. Besides, the Hartree potential between the leads is assumed linear in our simulation; this is often a good approximation in the presence of both disorder and e-e interaction [60].

The particle occupation at the middle of the wire under different voltage bias and e-e interaction strengths u is displayed in Fig.4.5. The two sharp drops in each curve correspond to the two Fermi surfaces at the lead chemical potentials; they would be smeared at a finite temperature. The signature of energy relaxation consists of the slope between the drops and the tail above the higher Fermi energy. In particular, we note that the "tail" must vanish at equilibrium even in the presence of interactions, as guaranteed by the one-particle fluctuation-dissipation relation [44]. Therefore this "tail" signifies a pure *nonequilibrium* effect of energy excitation. Both the "tail" and the slope increase with an increasing bias (Fig.4.5a) or an increasing interaction strength (Fig.4.5b). Indeed, increasing these two parameters amounts to an enhancement of the equilibration process. In the sense of energy relaxation, the effect of increasing bias can be interpreted as a phase-space augmentation to facilitate the e-e scattering.

4.2.2 Coulomb drag

Coulomb drag [42] refers to the phenomenon that a charge current (or an open-circuit voltage) is induced in an otherwise equilibrium conductor when it is placed beside another conductor which is driven out of equilibrium (Fig.4.6), even though there is no particle exchange between the two. The Coulomb drag is a true e-e correlation effect in that the Hartree-Fock does not contribute: the electrostatic and exchange effects merely induce a Hermitian correction to the noninteracting Hamiltonian, and therefore the equilibrium conductor would stay equilibrium. The first-order physical process contributing to the drag effect thus comes from the diagram depicted in Fig.2.10(c), which is also the lowest-order contribution to the quasiparticle relaxation rate in a many-electron system [12]. Indeed, the Coulomb drag can be viewed as a manifestation of the elementary scattering of correlated electrons in the special case that they are spatially separated. From this point of view, the drag current is just a result of momentum transfer between interacting conductors since charge current is entirely determined by the momentum distribution [103, 104]. Nevertheless, we classify Coulomb drag as an energy relaxation effect in this chapter because the momentum transfer involved in the drag process is always associated with certain amount of energy transfer. The reason is that there is only one single Fermi surface in the dragged conductor and, without inter-conductor

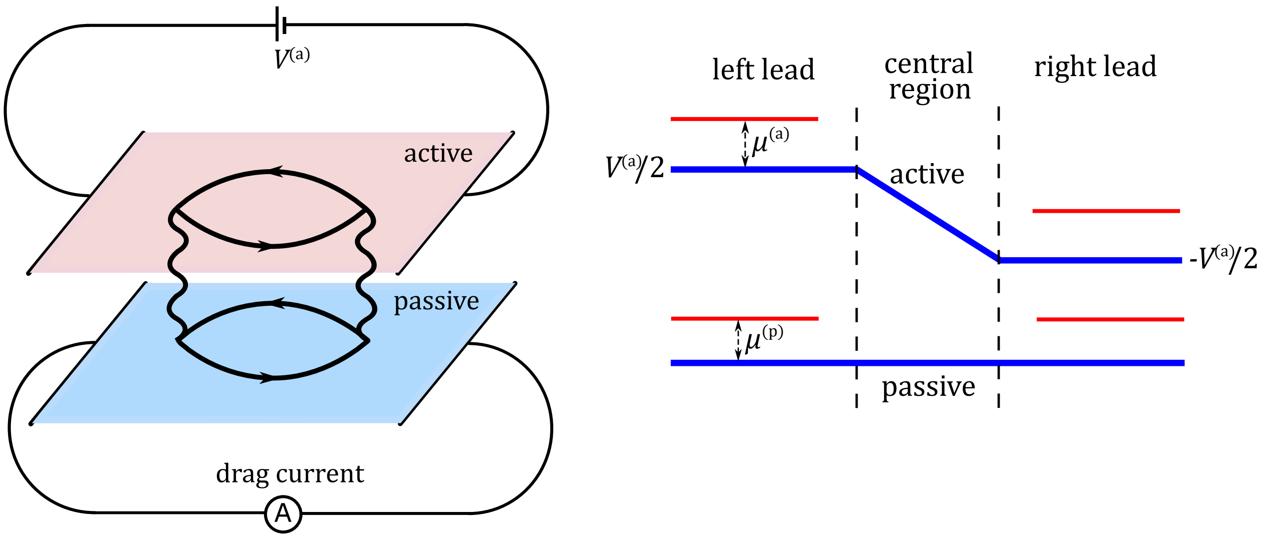

Figure 4.6: Left panel: Schematic diagram of the Coulomb drag setup. A potential bias is applied across the active wire and the drag current is measured in the passive wire. The Feynman diagram in the plot represents the lowest order process responsible for the drag effect, corresponding to the self-energy of Fig.2.10(c). Right panel: potential profile in the wires. Blue lines represent the electrostatic (Hartree) potential which rigidly shifts energy levels of the noninteracting Hamiltonian. Red lines represent chemical potentials measured with respect to the band structure center of respective leads.

interactions, all states below the Fermi energy are filled (assuming zero temperature). Therefore, for a change in momentum, an electron in the dragged conductor must jump over the Fermi surface, which necessitates some energy exchange.

Another perspective to the Coulomb drag physics consists in relating the drag current to the classical or quantum fluctuations in the driving conductor. Specifically, as suggested by early theoretical works [105, 106] specializing in the linear response Coulomb drag, the dc drag current could be interpreted as a rectification of the thermal charge fluctuation (represented by the polarization) in the driving conductor. As a result the linear Coulomb drag exists only at a finite temperature. On the other hand, recent studies on double quantum dots [42, 107, 108] have pointed out a new direction of the Coulomb drag physics at zero temperature: instead of the nearly equilibrium thermal fluctuations, the drag current can also be driven by the shot noise of finite mesoscopic conductors in the nonlinear regime. With this understanding, Coulomb drag has been further proposed as a noise sensing technique for nanoscale circuits [42].

In terms of diagrammatics, both equilibrium and nonequilibrium charge fluctuations are unitedly represented by the polarization diagram in Fig.2.10(c). Thus they are treated on an equal footing in our nonequilibrium formalism. In accordance with the previous linear-response analyses

[105, 106, 109] on the Coulomb drag, we keep only the lowest-order diagram for our simulations, i.e. truncating the W series at Fig.2.10(c). We note that higher-order drag effects [42, 110] and in particular the drag in non-Fermi-liquids [111–113] have arisen as an active field of research recently. These advanced topics are not accounted for by the formalism presented here.

After the brief survey on Coulomb drag theory, we now set up a minimal numerical model to simulate the Coulomb drag effect in mesoscopic wires. As sketched in Fig.4.6, the system consists of two parts. The upper subsystem (referred to as the active wire in the following) is subject to an external bias $V^{(a)}$, i.e. the band structures in the corresponding leads differ by a rigid shift of $eV^{(a)}$. On the other hand, the lead band structures and the chemical potentials in the lower subsystem (passive wire) are set aligned, so that it would be at equilibrium when the interwire interaction is turned off. Besides, we assume a linear Hartree potential (see Fig.4.6) between each pair of the leads, and the temperature is set at zero in all leads. Both wires are modeled by the discrete lattice with identical hopping amplitude ξ, lattice constant a, and a binary impurity energy $\pm v$. In the real-space the two wires are placed parallel to each other: we stack together two copies of the lattice defined in Fig.2.15. In our simulations the interwire distance is fixed at a and no interwire hopping is allowed. In order to analyze the elementary Coulomb drag physics we remove the intrawire e-e interaction and assume an interwire interaction of the form

$$H_{\mathrm{e-e}} = \sum_{i\in\mathrm{active}, j\in\mathrm{passive}} \frac{u}{\sqrt{\left(x_i - x_j\right)^2 + \left(y_i - y_j\right)^2 + a^2}} \hat{n}_i^{(a)} \hat{n}_j^{(p)}, \tag{4.10}$$

where i, j are restricted within the central scattering region. The following formula [cf. Eq.(2.74)] is used to compute the charge current through any of the four leads denoted by α:

$$I_\alpha = \frac{e}{h} \int d\varepsilon \mathrm{Tr}\left[\Sigma_\alpha^<(\varepsilon) G^>(\varepsilon) - \Sigma_\alpha^>(\varepsilon) G^<(\varepsilon)\right]. \tag{4.11}$$

Note that the lead chemical potentials $\mu^{(a,p)}$, which are measured with respect to band centers, are set equal in either wire. In our simulations the chemical potentials and the bias voltages are treated as independent model parameters. For later reference we also formulate the energy current [60] as follows:

$$J_\alpha = \frac{1}{h} \int \varepsilon \cdot \mathrm{Tr}\left[\Sigma_\alpha^<(\varepsilon) G^>(\varepsilon) - \Sigma_\alpha^>(\varepsilon) G^<(\varepsilon)\right] d\varepsilon. \tag{4.12}$$

Conservation laws supposedly lead to $I_{\mathrm{L}}^{(a)} + I_{\mathrm{R}}^{(a)} = I_{\mathrm{L}}^{(p)} + I_{\mathrm{R}}^{(p)} = 0$ (i.e. charge conservation in respective wires) and $J_{\mathrm{L}}^{(a)} + J_{\mathrm{R}}^{(a)} + J_{\mathrm{L}}^{(p)} + J_{\mathrm{R}}^{(p)} = 0$ (i.e. total energy conservation), which can be utilized as numeric accuracy criteria for our simulations.

To illustrate the Coulomb drag physics, we first carry out our numerical simulation for a pair of wires with $L = 10, W = 1$ under a fixed activation bias $V^{(a)} = 0.8\xi/e$ (while leaving the chemical

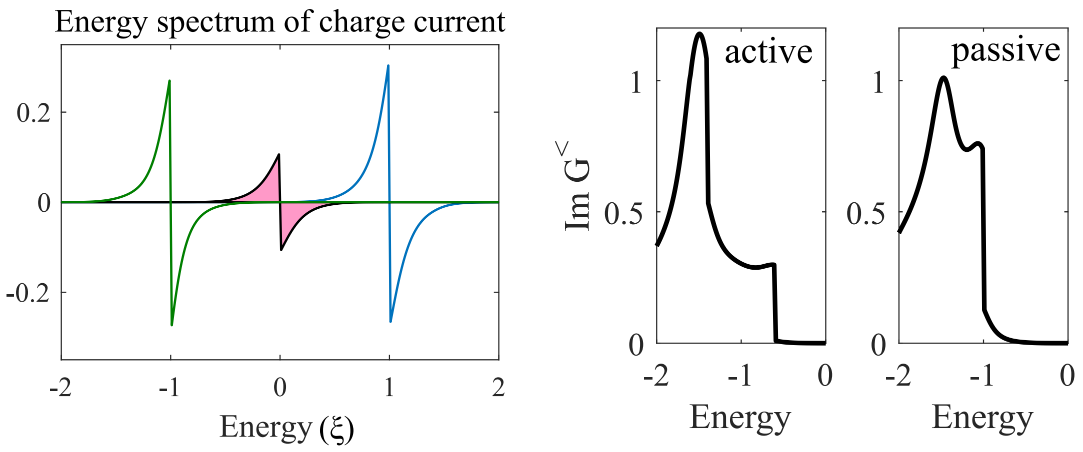

Figure 4.7: Left panel: integrand of Eq.(4.11) for the left lead of the passive wire, at $\mu^{(a/p)} = -1,\ 0,\ 1\xi$ (corresponding to green, black, blue curves) respectively. Right panel: electron occupation at the middle of the two wires when $\mu^{(a/p)}$ is set at -1.0ξ. Other model parameters: $v = 0.2\xi,\ u = 1.0\xi,\ V^{(a)} = 0.8\xi/e,\ L = 10a,\ W = 1$.

potentials $\mu^{(a,p)}$ variable). As expected the presence of the active wire would drive the passive one out of equilibrium. To gain insights we plot in Fig.4.7 the energy spectrum of the charge current in the passive wire, i.e. the integrand of Eq.(4.11), in the following denoted by $i(\varepsilon)$. In the figure the typical profile of $i(\varepsilon)$ is illustrated under three different chemical potentials $\mu^{(a/p)} = -1, 0, 1\xi$, situated in the lower half, center, and the upper half of the band-structure correspondingly. We notice that $i^{(p)}(\varepsilon)$ is in general neither positive nor negative definite: the current carried by the excited electrons above the Fermi energy is always accompanied by a countercurrent (commonly pictured as the hole drag current in the literature [42]) which comes from the depleted states just below the Fermi energy, and their subtraction amounts to the net measurable drag current in the electrodes. An absolute cancelation occurs when $\mu^{(a/p)}$ is set at zero, i.e. the band center.[4] In Fig.4.7 the shaded areas under the profile of $i^{(p)}(\varepsilon)$ at $\mu^{(a/p)} = 0$ exactly cancel, resulting in a zero drag current. However, note that a zero drag current does not mean that the passive wire remains equilibrium in this case. We shall shortly see that its nonequilibrium status can also be identified by the energy flow. In contrast to the $\mu^{(a/p)} = 0$ case, nonzero drag currents are obtained at $\mu^{(a/p)} = -1, 1\xi$. Interestingly, although the two $i^{(p)}(\varepsilon)$ profiles do not match, they in fact amount to equal drag currents. This is a result from the following more general relation which applies to systems with electron-hole symmetric band-structures:

$$I^{(p)}(\mu^{(a)}, \mu^{(p)}) = -I^{(p)}(-\mu^{(a)}, \mu^{(p)}) = -I^{(p)}(\mu^{(a)}, -\mu^{(p)}) = I^{(p)}(-\mu^{(a)}, -\mu^{(p)}), \tag{4.13}$$

---

[4] In fact, absolute cancelations can occur when either of $\mu^{(a,p)}$ is set at the band center, see Eq.(4.13).

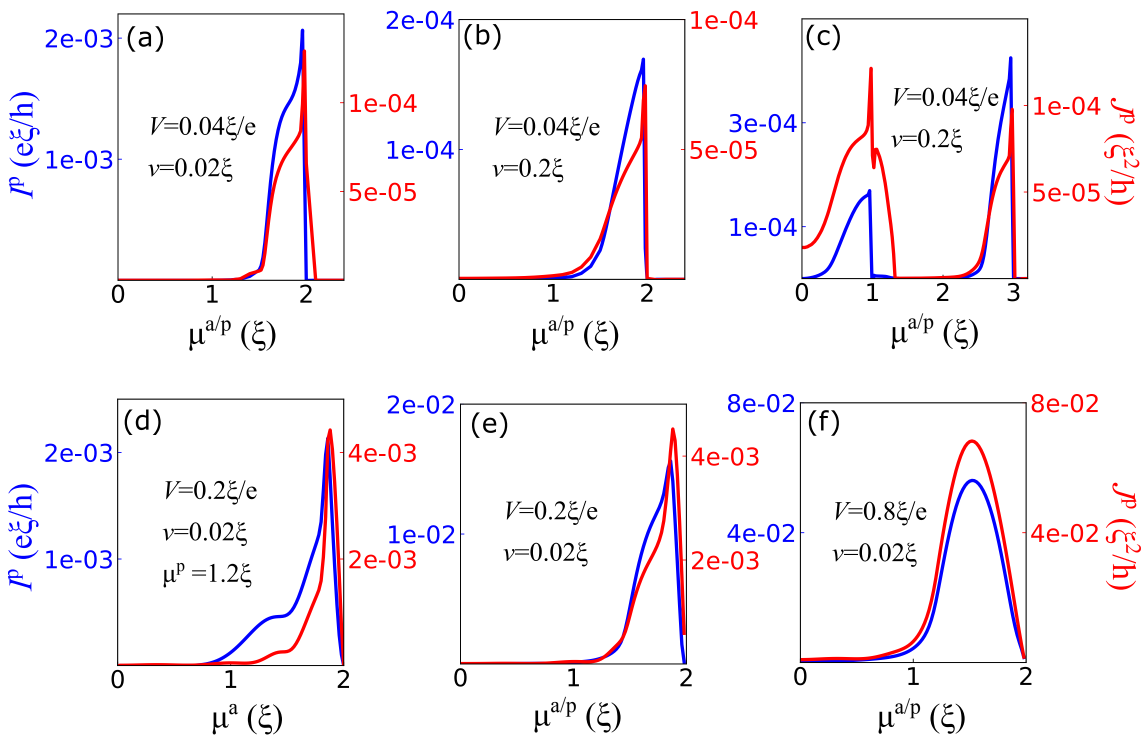

Figure 4.8: Relation between the passive charge current $I^{(p)}$ (blue curves), the interwire energy current $J^{(p)}$ (red curves), and the chemical potentials $\mu^{(p)}, \mu^{(a)}$. The e-e interaction is set at $u = 1.0\xi$, and the wire length $L = 10a$. For results in subplot (c), a wire width of $W = 2a$ is used ($W = 1$ for the others). Note that only half of the energy range is shown here because the other half can be deduced with the parity relation Eq.(4.13).

where the drag current $I^{(p)}$ is viewed as function of $\mu^{(a,p)}$ at given $V^{(a)}$. The proof of Eq.(4.13) is given in appendix C. It should be pointed out that the relation (4.13) may not hold if certain higher order diagrams or physical processes are taken into account [110].

As stated above, the energy relaxation effect is essential for Coulomb drag. To concretize this point we plot in Fig.4.7 the particle occupation in the active and passive wires respectively. As can be seen, the occupation in the active wire is similar to that of an isolated nonequilibrium wire. In contrast, the occupation in the passive wire shows only one "cliff" at $\mu^{(a/p)}$. The lack of a nonzero energy window for transport results in the smallness of its drag current. Another noticeable feature on the occupation profile is the "tail" at $\varepsilon > \mu^{(a/p)}$: it signifies the presence of energy relaxation due to interaction with the active wire.

In the following we shall further analyze the relation between the drag current and the chemical potentials. Under a relatively small bias voltage $V = 0.04\xi/e$ and disorder strength $v = 0.02\xi$, the charge current $I^{(p)}$ in the passive wire and the energy current J between two wires are computed

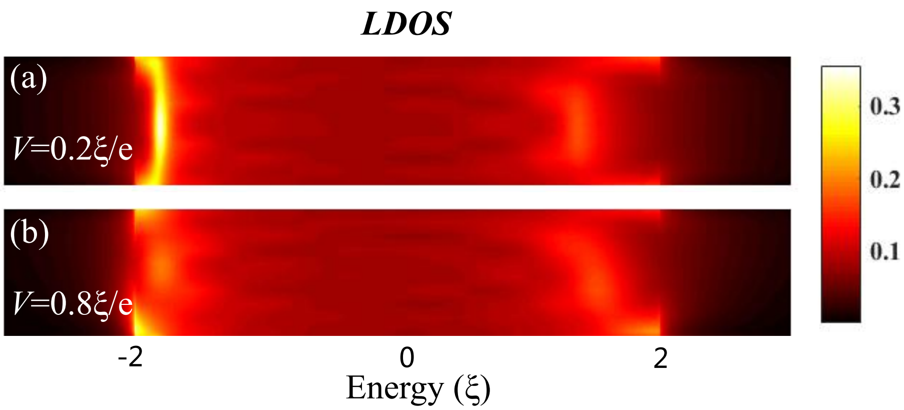

Figure 4.9: Local density of states in the passive wire under two different activation bias voltages. The y-axes of the plots represent positions along the wire in the interaction region. The chemical potentials $\mu^{(a/p)} = -1.8\xi$. Other model parameters are same as those for Fig.4.8(e,f).

with varying chemical potentials ($\mu^{(p)} = \mu^{(a)}$). The result is displayed in Fig.4.8(a). We see that $I^{(p)}$ is noticeably pronounced when $\mu^{(a/p)}$ is close to 2ξ, which is the band edge. This behavior was first observed in the study of ballistic wires using the Boltzmann equation approach [114, 115]: it was found that the low group velocities around the band edge together with a small interwire momentum transfer lead to an enhanced Coulomb matrix, and hence produce a drag current peak. Figure 4.8(a) indicates that the band-edge associated drag peak preserves in our model whose interaction region is rather constrained, much smaller than the thermal length, and hence it might have a different origin. It was argued in Ref.[42] that this drag peak may be instead related to the mesoscopic shot noise which is also peaked at band edges. Overall one could understand the drag peak based on the simple fact that the electron-hole asymmetry, which lies in the heart of drag effects, reaches maximum at band edges. The evolution of this drag peak in response to other model parameters is as follows. Increasing the disorder strength (Fig.4.8b) and the bias voltage (Fig.4.8e) respectively decreases and increases the overall drag current, while its peak near the band edge retains. Further increasing the bias $V^{(a)}$ however degrades this peak structure, as illustrated by Fig.4.8(f). This observation can be explained by the smearing of the van Hove singularity due to enhanced energy relaxation at high bias voltage. To concretize this reasoning we plot in Fig.4.9 the local DOS of the passive wire under $V^{(a)} = 0.2\xi/e$ and $0.8\xi/e$ respectively. The glowing area in Fig.4.9(a) then corresponds to the van Hove DOS singularity of one-dimensional materials, and clearly it fades out at $V^{(a)} = 0.8\xi/e$. Figure 4.8(d) shows the result when $\mu^{(p)}$ is fixed at 1.2ξ and we sweep $\mu^{(a)}$ only. Although the drag current in this case is overall much smaller than that in Fig.4.8(e), it still preserves the peak structure at the band edge. In addition to strict one-dimensional wires, the Coulomb drag in wires whose electronic structure consists of two bands is also computed; the result is displayed in Fig.4.8(c). We observe an additional peak situated at the sub-band edge, which agrees with the prediction by previous theoretical works [114, 115].

So far we have been focusing on the *charge* current in our Coulomb drag model. Recent theoretical works have shown a growing interest in the energy flow (or near-field heat transfer in some contexts) between insulated many-electron systems [110, 116, 117]. As indicated in Eq.(4.12), our formalism is also applicable to computing the energy current. For the numerical model used here, the interwire energy currents (from the active wire to the passive wire) are computed and plotted in Fig.4.8 along with the charge currents. As can be seen, the two currents are highly correlated. Indeed, a higher energy transfer rate can drive a larger drag current. However, note that energy currents can exist even if there is zero charge current in the passive wire. For example at the electron-hole symmetric point $\mu^{(a/p)} = 0$, the charge current $I^{(p)} = 0$, as a result of Eq.(4.13), while the energy current can be nonzero, as best illustrated by Fig.4.8(c). In fact, even if the driving bias is set at zero, i.e. $V^{(a)} = 0$, there can be a nonzero energy flow between the wires, given a temperature difference.

4.3 Summary

We have formulated a practical numerical method for simulating Fermi-liquid-based many-electron systems, in the presence of both e-e interaction and disorder. Specifically we approximate the many-body correlation effect by discarding the vertex correction in the Hedin equations. The resulting so-call GW scheme consists of a closed set of equations which can be solved efficiently with a self-consistent numerical program. Besides, its Φ-functional derivablility ensures conservation laws to hold. The numerical formalism was applied to simulating the energy relaxation effects in mesoscopic wires, which require a self-consistent treatment of the correlation self-energy. The energy relaxation in single wires is manifested in the energy distribution of particle occupation: the inelastic e-e scattering tends to drive a nonequilibrium system toward a locally equilibrium state. Signatures of this process can be readily seen on the $G^<$ profile obtained from the self-consistent calculation. In particular, the equilibration was found enhanced as either the bias or the e-e interaction is increased, in qualitative agreement with experimental results [14]. We have also studied a very interesting energy relaxation effect in pairs of mesoscopic wires, namely the Coulomb drag effect. Using numerical results we have elucidated the strong dependence of Coulomb drag on the electron-hole asymmetry which comes from the underlying band structures. We also pointed out a potential usage of our formalism to investigate the near-field energy transfer between interacting systems.

Chapter 5

Altshuler-Aronov effects

The Altshuler-Aronov (AA) effects refer to two experimental discoveries in mesoscopic metallic systems, i.e. the zero-bias anomaly [29, 118] and the temperature-dependent quantum correction to conductivities [25, 119]. The former phenomenon concerns the strong density of states (DOS) depletion at the Fermi energy of disordered low-dimensional samples. It is manifested as a dip on the differential conductance (dI/dV) profile obtained from tunnel junction measurements where the disordered sample forms a tunnel contact with the reference electrode. The zero-bias simply refers to the equilibrium situation where the two Fermi energies are aligned and thus the DOS at the Fermi energy of the disordered sample is probed. Notably, this tunnel conductance dip gets deeper rapidly as the temperature decreases. Removing the tunnel contact and measuring the conductivity of the disordered sample on its own, one finds a similar temperature dependency.[1] These two phenomena turn out to be closely related [12] and essentially arise from the same physical process which involves the *interplay* between disorder scattering and e-e interaction. In the following we set up a heuristic picture to illustrate this very important physical process based on the works of Refs.[23, 120].

In Sec.3.1 it was argued that, for a pair of paths making nonzero contribution to the two-point propagation probability upon disorder-average, they must pass through the same set of impurity sites. However, this restriction can be relaxed in the presence of e-e interaction: Even spatially separated paths can be paired up and yield a nonzero interference that affects the probability propagation. To see this, consider a single impurity placed in the middle of an electron gas (Fig.5.1a). The induced potential disturbance reconstructs the surrounding electron distribution, which thus acts as an additional scattering source to electrons passing through the medium. The red path shown

---

[1] Usually the conductivity measurement mixes in the contribution from the weak localization effect. To separate out the temperature dependence due to the AA effect, one could apply a magnetic field. Unlike the weak localization, the AA effect is unsusceptible to phase misalignment.

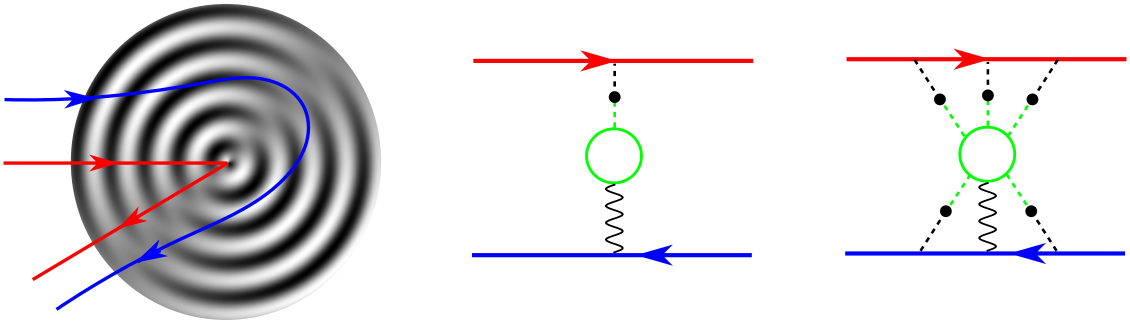

(a) (b) (c)

Figure 5.1: (a) Illustration of the two associated scattering processes. A single impurity is placed at the center of the circle, and it induces a charge redistribution in the vicinity. The resulting potential fluctuation acts as additional scattering source to the electrons (blue curve). (b) Diagrammatic representation of (a). (c) Generalization of (b) for a system containing multiple random impurities.

in Fig.5.1(a), which scatters off the impurity itself, and the blue one experiencing the Coulomb potential created by the charge "ripples"[2] thus form an interfering pair to be counted in the total probability propagation. Notably, this contribution survives under the disorder-average over impurity potential, because the charge redistribution is correlated to the impurity.

The scattering process described above is translated into the diagram shown in Fig.5.1(b). The green part represents the electron density correction due to the presence of impurity, and it is connected to the blue line via a wavy curve which stands for the direct Hartree interaction. Figure 5.1(c) is a generalization to Fig.5.1(b) for systems containing multiple random impurities. In this case, taking disorder-average amounts to attaching the impurity (dashed) lines that are rooted on the green ring to those on the arrowed lines. The resultant diagram is reminiscent of the self-energy which we showed before in Fig.2.11(a'), from which Fig.5.1(c) can be formally derived. In fact, the physical process described here has a Fock counterpart which should also be taken into account on an equal footing. Although the Fock process is not as easily visualized as in Fig.5.1(a), its diagrammatic representation is readily available, as given by Fig.2.11(b'). The self-energies of Figs. 2.11(a') and 2.11(b') thus constitute the foundation of the Altshuler-Aronov formalism.

The interaction induced suppression to the DOS and conductivity of diffusive conductors was first elucidated by Altshuler and Aronov using the perturbative linear-response approach [21, 121]. As in $d \leq 2$ this suppression develops a singularity at the zero temperature, the AA effect is believed to be a precursor of the much more complicated Anderson-Mott transition [122]. The implication of a phase transition signifies the necessity of renormalization treatments, which were

---

[2] These ripples are commonly known as the Friedel oscillation in many-electron systems [32].

henceforth developed in Refs.[123–125].

The investigation of AA effects in finite nonequilibrium structures was initiated by Nagaev [126], who analytically derived an expression for the nonlinear current in diffusive metallic contacts. Part of Nagaev's development will be reviewed below in this chapter. Using a quasiclassical approach, Schwab *et al.*[127] analyzed the nonlinear transport in nanowires of different characteristic ratios L_T/L, where $L_T = \sqrt{\hbar D/k_B T}$ is the thermal diffusion length. Aiming to generalize the zero-bias anomaly at nonequilibrium, Gutman *et al.*[128] considered a disordered film with its longitudinal size smaller than the energy relaxation length. Specifically, using matrix-field analyses, they found that the DOS anomaly should split in two at the electrode Fermi energies, and that the anomalies are smeared by certain dephasing effect due to the bias-induced fluctuations of internal electromagnetic fields.

The main objective of this chapter is to establish a diagrammatic formalism that computes the AA corrections in nonequilibrium numerical models without phenomenological parameters typically invoked in theoretical analyses. We shall stick closely to the original diagrammatics formulated in Ref.[21], which is focused on the most elementary interaction process between diffusive electrons.[3] Before getting into the implementation details of our numerical formalism, we shall first derive some analytical results that will give us a preliminary idea about what becomes of the AA effect in finite nonequilibrium systems.

5.1 Theoretical analyses

Our theoretical model consists of a short wire sandwiched between two ideal electrodes, i.e. the continuous version of Fig.2.15. The wire length L should be much longer than the electron-impurity mean free path (l_0), so that the transport is mostly diffusive and that the energy distribution of electrons follows the diagram in Fig.3.4. Throughout our analyses the e-e interaction will be treated as a first-order perturbation.

Before getting into the analytical derivation, it would be helpful to review the various characteristic length scales in the problem. First, because of momentum relaxation, wavefunctions of single-particle states are confined in a spatial region bounded by l_0. However, the particle density could correlate in space over a distance much larger than l_0. This type of long-range correlation is associated with the diffuson and is usually characterized by a classical length scale $L_\omega = \sqrt{D/\omega}$, as can be obtained from Eq.(B.11) of Appendix B. In the following, we shall see that the ratio between L_ω and the sample size (L) plays an important role in the interaction correction to DOS.

---

[3] The Cooperon process contributes a modification to the AA effects, as discussed in Refs.[21, 129].

At nonzero temperatures, the thermal diffusion length $L_T = \sqrt{\hbar D/k_B T}$ would come into play, which was used to cutoff the macroscopic sample size in the original work [21]. For short mesoscopic wires it is reasonable to set $L_T \gg L$, so that L_T becomes irrelevant effectively. In addition to the diffuson, another long-range object could be the Coulomb interaction, whose spatial scope depends specifically on the charge carrier density and the system dimension. Nevertheless, it is essentially the long-range nature of the diffuson that is responsible for the singularities in the interaction induced corrections, whereas different models of e-e interaction merely result in some additional prefactors [12, 21].

The above length scale analysis should suffice when the e-e interaction is treated only to the first order. However, if one were to go beyond this approximation level, other length scales, such as the energy relaxation length and the dephasing length [22], would come into the picture and further complicate the problem. These higher-order effects will not be considered in this section, but they will be revisited in Sec.5.3 by means of numerical investigation. Analytical results of this section apply to short diffusive wires where the dominant cutoff length scale is the wire length itself.

5.1.1 Density of states

The first-order DOS correction due to interaction can be written as

$$\delta\nu(\varepsilon) = -\frac{1}{\pi}\mathrm{Im}[G^{\mathrm{R}}(\varepsilon)\Sigma^{\mathrm{R}}(\varepsilon)G^{\mathrm{R}}(\varepsilon)], \tag{5.1}$$

where G^{R} denotes the non-interacting (retarded) Green's function and Σ^{R} denotes the Hartree-Fock self-energy

$$\begin{aligned}\Sigma^{\mathrm{R}}(\mathbf{r}_1, \mathbf{r}_2, \varepsilon) &= -2\mathrm{i}\delta(\mathbf{r}_1 - \mathbf{r}_2)\int \frac{d\omega}{2\pi}\int d\mathbf{r}\; G^{<}(\mathbf{r}, \mathbf{r}, \omega)U^{\mathrm{R}}(\mathbf{r}_1, \mathbf{r}, 0) \\ &+ \mathrm{i}\int \frac{d\omega}{2\pi}\left[G^{<}(\mathbf{r}_1, \mathbf{r}_2, \varepsilon-\omega)U^{\mathrm{R}}(\mathbf{r}_1, \mathbf{r}_2, \omega) + G^{\mathrm{R}}(\mathbf{r}_1, \mathbf{r}_2, \varepsilon-\omega)U^{<}(\mathbf{r}_1, \mathbf{r}_2, \omega)\right].\end{aligned} \tag{5.2}$$

Plugging Eq.(5.2) into Eq.(5.1) and then taking disorder average, we find the following Green's function correlators to be calculated: $\langle G^{\mathrm{R}}G^{<}G^{\mathrm{R}}\rangle$ and $\langle G^{\mathrm{R}}G^{\mathrm{R}}G^{\mathrm{R}}\rangle$. The lesser Green's function can be expanded in the form $G^{\mathrm{R}}vG^{\mathrm{R}}\cdots vG^{<}v\cdots G^{\mathrm{A}}vG^{\mathrm{A}}$. The diagram for calculating averages of three Green's functions follows that in Fig.2.7(b). When disorder-average is taken under the first Born approximation, the $K^{(2)}$ four-point vertex reduces to a single dashed line (see Fig.3.2), and diffuson ladders are formed in the three corners. Note that the $K^{(3)}$ kernel vanishes here since a single impurity line does not contain internal Green's functions. When evaluating the ladder series, we are only concerned about those corresponding to $\langle G^{\mathrm{R}}G^{\mathrm{A}}\rangle$ since any pair of G^{R} would

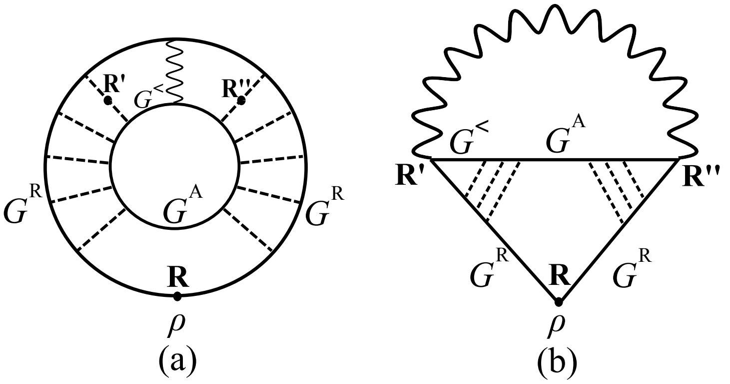

Figure 5.2: Diagrams for the Hartree (a) and Fock (b) corrections to the electronic density of states. The capital letters (e.g. $\mathbf{R}$) mark macroscopic spatial coordinates based on a length scale greater than the impurity-electron mean free path.

result in a small factor $(\varepsilon_{\rm F}\tau)^{-1}$ [see Eq.(B.2)]. The resulting diagrams are given in Fig.5.2. Note that we have discarded the correlator $\langle G^{\rm R}G^{\rm R}G^{\rm R}\rangle$ and omitted the vertex correction in the bottom corner. In addition, $G^<$ is pushed to the leftmost in order to avoid having $G^{\rm R}G^{\rm R}$. The resulting ladder series is evaluated as $\gamma\langle G^{\rm R}G^{\rm A}\rangle\gamma = \mathcal{P}/(2\pi\nu_0\tau_0^2)$, where $\mathcal{P}$ denotes the diffusion propagator as defined in Eq.(B.12).

On the one hand, the ladder series that show up in the diagrams represent diffuson propagators which are long-range objects varying on a length scale greater than the microscopic mean free path (l_0). On the other hand, the Green's functions decay exponentially over a distance of l_0. With this observation, those diagram blocks between the diffusons can be calculated separately: they can be "detached" from the diffusons. For instance the triangular block at the bottom of either diagram is sandwiched between two diffusons, and therefore it can be written as

$$\int d\mathbf{r}_1 d\mathbf{r}_2 G^{\rm R}(\mathbf{R},\mathbf{r}_1,\varepsilon)G^{\rm A}(\mathbf{r}_1,\mathbf{r}_2,\varepsilon-\omega)G^{\rm R}(\mathbf{r}_2,\mathbf{R},\varepsilon)$$
$$= \int \frac{d^dk}{(2\pi)^d}\left[G^{\rm R}(\mathbf{k},\varepsilon)\right]^2 G^{\rm A}(\mathbf{k}-\mathbf{q},\varepsilon-\omega) \approx I^{2,1} = -2\pi {\rm i}\nu_0(\varepsilon){\tau_0}^2, \tag{5.3}$$

where $\mathbf{r}_1$ and $\mathbf{r}_2$ are integrated independently on the diffusons, because of their scale difference. In performing the k-integration above, we have used the techniques developed in Appendix B. Note that the $\mathbf{q}$-dependence in the above integral has been discarded: if not, the expansion technique of Eq.(B.7) should be used, which would lead to an extra factor of ql_0, small under the diffusive approximation.

Figure 5.3 displays a closer view of the diagram blocks which contain the interaction vertex. Since these blocks are also sandwiched between diffusons, they can be evaluated in the same way

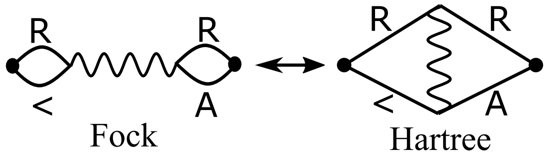

Figure 5.3: Close view of the diagram blocks which contain the e-e vertex in Fig.5.2. R, A, $<$ denote retarded, advanced, and lesser (Green's function) respectively. The black dots mark the joints with diffusons.

as Eq.(5.3). For the diagram on the left hand side of Fig.5.3, we can write down the expression

$$\left[\int \frac{d^dk}{(2\pi)^d} G^<(\mathbf{k}\mathbf{R}', \varepsilon-\omega) G^{\mathrm{R}}(\mathbf{k}\varepsilon)\right] U^{\mathrm{R}}(\mathbf{R}', \mathbf{R}'', \omega) \left[\int \frac{d^dk}{(2\pi)^d} G^{\mathrm{A}}(\mathbf{k}, \varepsilon-\omega) G^{\mathrm{R}}(\mathbf{k}\varepsilon)\right]. \quad (5.4)$$

Note that the $\mathbf{R}'$-dependence in $G^<$ should not be overlooked since it could vary on a macroscopic length scale. To proceed we approximate $G^<$ as

$$G^<(\mathbf{k}\mathbf{R}', \varepsilon-\omega) \approx f(\varepsilon-\omega, \mathbf{R}') \left[G^{\mathrm{A}}(\mathbf{k}, \varepsilon-\omega) - G^{\mathrm{R}}(\mathbf{k}, \varepsilon-\omega)\right], \quad (5.5)$$

where f is given by the diffusive distribution (3.9). The remaining k-integrals in (5.4) thus read

$$\left[\int \frac{d^dk}{(2\pi)^d} G^{\mathrm{A}}(\mathbf{k}, \varepsilon-\omega) G^{\mathrm{R}}(\mathbf{k}\varepsilon)\right]^2 \approx (I^{1,1})^2 = (2\pi\nu_0\tau_0)^2. \quad (5.6)$$

Here the ω-dependence has been discarded since it would give rise to terms carrying a factor of $\omega\tau_0$, which is again small in the diffusive limit.

The diagram on the right hand side of Fig.5.3 reads

$$\int d(\mathbf{r}_1-\mathbf{r}_2) \left[\int d\mathbf{r}' G^<(\mathbf{r}_1, \mathbf{r}', \varepsilon-\omega) G^{\mathrm{R}}(\mathbf{r}', \mathbf{r}_2, \varepsilon)\right] U^{\mathrm{R}}(\mathbf{r}_1-\mathbf{r}_2, 0) \\ \times \left[\int d\mathbf{r}'' G^{\mathrm{A}}(\mathbf{r}_1, \mathbf{r}'', \varepsilon-\omega) G^{\mathrm{R}}(\mathbf{r}'', \mathbf{r}_2, \varepsilon)\right]. \quad (5.7)$$

The reason why we integrate over the difference $(\mathbf{r}_1-\mathbf{r}_2)$ instead of $\int d\mathbf{r}_1 d\mathbf{r}_2$ separately is that the e-e vertex is surrounded by the Green's functions and its center must be constrained in the microscopic region: $(\mathbf{r}_1+\mathbf{r}_2)/2 = \mathbf{R}' = \mathbf{R}''$. To proceed we again adopt the approximation Eq.(5.5), and hence the integrals in the brackets of (5.7) amount to

$$\left[\int G^{\mathrm{R}}(\mathbf{r}_1, \mathbf{r}') G^{\mathrm{A}}(\mathbf{r}', \mathbf{r}_2) d\mathbf{r}'\right]^2 = \left(\mathrm{i}\tau_0 \left[G^{\mathrm{R}}(\mathbf{r}_1, \mathbf{r}_2) - G^{\mathrm{A}}(\mathbf{r}_1, \mathbf{r}_2)\right]\right)^2 = \left[2\tau_0 \mathrm{Im} G^{\mathrm{R}}(\mathbf{r}_1, \mathbf{r}_2)\right]^2, \quad (5.8)$$

where the first equality follows directly from Eq.(3.5). To simplify the notation, we introduce a function as follows:

$$\alpha(\mathbf{r}) = -\frac{\mathrm{Im} G^{\mathrm{R}}(\mathbf{r})}{\pi\nu_0} = \cos\sqrt{2m\varepsilon} r \cdot \exp(-r/2l_0), \quad d=1 \quad (5.9)$$

where the second equality follows from the Fourier transform of Eq.(3.5) in one-dimension. Apparently $\alpha(\mathbf{r})$ is a short-range function bounded by l_0. Thus the interaction block in the Hartree diagram contains a factor of $\int \alpha^2(\mathbf{r})U^{\mathrm{R}}(\mathbf{r},0)d\mathbf{r}$, where the long-range part of the Coulomb potential is cut off by l_0. Besides, note that only the static potential $U^{\mathrm{R}}(\mathbf{r},\Omega=0)$ counts here, since in the Hartree diagram the interaction vertex is connected to a closed fermion loop which conserves energy.

Collecting all the pieces in Fig.5.2, we get

$$\begin{aligned}\delta\nu(\varepsilon,\mathbf{R}) = -\frac{\nu_0}{\pi}\mathrm{Im}\int d\omega d\mathbf{R}'d\mathbf{R}''\mathcal{P}(\mathbf{R},\mathbf{R}',\omega)f(\varepsilon-\omega,\mathbf{R}')\\ \times[U^{\mathrm{R}}(\mathbf{R}',\mathbf{R}'',\omega)-2\mathcal{F}\bar{U}\delta(\mathbf{R}'-\mathbf{R}'')]\mathcal{P}(\mathbf{R}'',\mathbf{R},\omega).\end{aligned} \tag{5.10}$$

The $\mathcal{F}$ factor arises from the e-e vertex in the Hartree diagram:

$$\mathcal{F} = \frac{\int \alpha^2(\mathbf{r})U^{\mathrm{R}}(\mathbf{r})d\mathbf{r}}{\int U^{\mathrm{R}}(\mathbf{r})d\mathbf{r}}, \tag{5.11}$$

where $\bar{U} = \int U^{\mathrm{R}}(\mathbf{r})d\mathbf{r} = U^{\mathrm{R}}(\mathbf{q}=0)$. Since $\alpha(\mathbf{r})$ is a short-range function decaying in space, the value of $\mathcal{F}$ falls in between 0 and 1. For very strong screening, namely when the screening length is shorter than the Fermi wavelength, $\mathcal{F}=1$, while in the opposite limit $\mathcal{F}=0$. It is important to notice that the actual value of $\mathcal{F}$ affects the sign of $\delta\nu$. Evaluating Eq.(5.10) also requires the knowledge of $U^{\mathrm{R}}(\mathbf{R}',\mathbf{R}'',\omega)$. According to the dynamic screening theory in the diffusive limit [12], the effective interaction is approximated as $U^{\mathrm{R}}(\mathbf{q},\omega)\approx(-\mathrm{i}\omega+Dq^2)/(2\nu_0 Dq^2)$ in Fourier space. To simplify the calculation of Eq.(5.10) and to meanwhile allow for cross-validations with our numerical formalism, we omit the ω-dependency and hence adopt a local interaction model:

$$U_0(\mathbf{R}_1-\mathbf{R}_2) = (2\nu_0)^{-1}\delta(\mathbf{R}_1-\mathbf{R}_2). \tag{5.12}$$

When restricted to one-dimension, Eq.(5.10) reads

$$\delta\nu(\varepsilon,x) = \frac{2\mathcal{F}-1}{2\pi}\mathrm{Im}\int d\omega\int_0^L dx' f(\varepsilon-\omega,x')[\mathcal{P}(x,x',\omega)]^2. \tag{5.13}$$

The diffuson $\mathcal{P}$ takes the one-dimensional form [see Eq.(B.15)]

$$\mathcal{P}(x,x',\omega) = \frac{L_\omega}{D}\frac{\sinh(x_m/L_\omega)\sinh(L-x_M)/L_\omega}{\sinh(L/L_\omega)}, \tag{5.14}$$

where $x_m=\min(x,x')$, $x_M=\max(x,x')$, and $L_\omega=\sqrt{\mathrm{i}D/\omega}$ sets the length scale of a diffusive mode with frequency ω. Using the linear expression of $f(\varepsilon,x)$, we rewrite the DOS correction in two parts:

$$\delta\nu = (1-2\mathcal{F})(\delta\nu_1+\delta\nu_2), \tag{5.15}$$

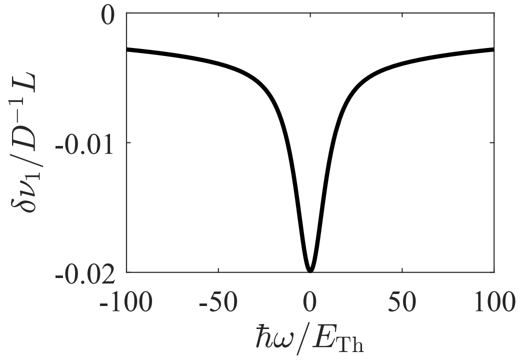

Figure 5.4: Schematic profile of the interaction-induced DOS anomaly in a disordered finite wire. The energy reference is set at the Fermi level. E_{Th} represents the Thouless energy $\hbar D/L^2$. See Eq.(5.18) for mathematical details.

where

$$\delta\nu_1(\varepsilon, x) = -\frac{1}{4\pi}\mathrm{Re}\left[\mathcal{P}_x(\varepsilon - eV/2) + \mathcal{P}_x(\varepsilon + eV/2)\right], \tag{5.16a}$$

$$\delta\nu_2(\varepsilon, x) = \mathrm{Im}\int\limits_{\varepsilon-eV/2}^{\varepsilon+eV/2}\frac{d\omega}{2\pi}\int_0^L dx'\frac{x'-L/2}{L}\left[\mathcal{P}(x,x',\omega)\right]^2. \tag{5.16b}$$

Let us first look at the first part $\delta\nu_1$, which is simply proportional to the recurrence probability $\mathrm{Re}\mathcal{P}_{x=x'}(\omega)$. Since $\mathrm{Re}\mathcal{P}_x(\omega)$ is an even function peaked at $\omega = 0$, $\delta\nu_1$ is symmetric in ε and has two cusps at $\varepsilon = \pm eV/2$ under an external bias. The cusp depth $\delta\nu_1(\pm eV/2)$ varies with x. To see this, we set ω at zero and hence obtain

$$\mathrm{Re}\mathcal{P}_x(\omega = 0) = \frac{x}{D}\left(1 - \frac{x}{L}\right). \tag{5.17}$$

Therefore $\delta\nu_1(\pm eV/2)$ is deepest at $x = L/2$, and around the cusp

$$\delta\nu_1(\omega, L/2) = -\mathrm{Re}\left\{\frac{\mathrm{tanh}L/2L_\omega}{8\pi\sqrt{-\mathrm{i}D\omega}}\right\}, \tag{5.18}$$

where $\omega = \varepsilon \pm eV/2$. The result of Eq.(5.18) is visualized in Fig.5.4. On the contrary, $\delta\nu_1(\pm eV/2)$ vanishes at the ends of the wire. The underlying physical picture is that, the closer particles get to the boundaries, the more tendency they will be absorbed by the reservoirs and never return to the interacting region.

At a fixed x/L ratio, $\delta\nu_1(\pm eV/2)$ is proportional to L. This implies a DOS singularity when the thermodynamic limit $L \to \infty$ is taken. To see this singularity on the energy axis, we set $x = x' = L/2$ at first and then get $\mathrm{Re}\mathcal{P}(\omega) = 1/\sqrt{8D\omega}$ from Eq.(5.14) in the limit $L \gg L_\omega$.

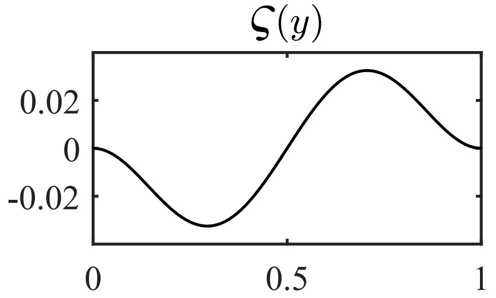

Figure 5.5: Plot of the function $\varsigma(y) = (1-2y)(y-1)^2y^2(4y^2-4y-1)$, which we invoke in Eq.(5.23).

Thus at equilibrium we have $\delta\nu_1(\varepsilon) = -(4\pi\sqrt{2D\varepsilon})^{-1}$, which reproduces the well-known "zero-bias anomaly" (as $\varepsilon \to 0$) first elucidated by Altshuler and Aronov [21]. In real materials, this singularity is cut off by the thermal diffusion length $\sqrt{\hbar D/k_BT}$ at a finite temperature. In the present work which is mainly focused on short wires, this anomaly is simply cut off by the system size [see Eq.(5.18)].

The second part $\delta\nu_2$ [see Eq.(5.16b)] exists only at nonequilibrium, and it contributes a subleading modulation on top of $\delta\nu_1$. The spatial integral in Eq.(5.16b) yields

$$\int_0^L dx' \frac{x'-L/2}{L}[\mathcal{P}(x,x',\omega)]^2 = \frac{L_\omega^4}{8LD^2\sinh^2(L/L_\omega)} \times \left[\left(1-\cosh\frac{2x}{L_\omega}-\frac{L-2x}{L_\omega}\sinh\frac{2x}{L_\omega}+\frac{2x(L-x)}{L_\omega^2}\right)\sinh^2\frac{L-x}{L_\omega}-(x\to(L-x))\right]. \tag{5.19}$$

Nevertheless, the remaining frequency integral cannot be performed analytically. To proceed we simplify the result of Eq.(5.19) in the low bias limit $eV \ll \hbar D/L^2 (= E_{\mathrm{Th}})$, where E_{Th} is known as the Thouless energy in the literature. In this limit, the frequency (ω) to be integrated over the bias window [see Eq.(5.16b)] is bounded by $\hbar\omega \ll E_{\mathrm{Th}}$. Therefore the diffuson $\mathcal{P}$ can be expanded with respect to the small parameter L/L_ω:

$$[\mathcal{P}(x,x',\omega)]^2 = \frac{L^2}{D^2}\tilde{x}_m^2(1-\tilde{x}_M)^2 + \frac{L^4}{3D^2L_\omega^2}\tilde{x}_m^2(1-\tilde{x}_M)^2(\tilde{x}_m^2+\tilde{x}_M^2-2\tilde{x}_M)+\cdots, \tag{5.20}$$

where the notation $\tilde{x}$ stands for x/L. The spatial integral of Eq.(5.19) thus reduces to

$$\begin{aligned}&\mathrm{Im}\int_0^L dx'\frac{x'-L/2}{L}[P(x,x',\omega)]^2\\ &\approx \mathrm{Im}\frac{L^5}{3D^2L_\omega^2}\left[\int_0^{x/L}(\tilde{x}'-1/2)[\tilde{x}'(\tilde{x}-1)]^2(\tilde{x}'^2+\tilde{x}^2-2\tilde{x})d\tilde{x}'\right.\\ &\qquad\left.+\int_{x/L}^1(\tilde{x}'-1/2)[\tilde{x}(\tilde{x}'-1)]^2(\tilde{x}'^2+\tilde{x}^2-2\tilde{x}')d\tilde{x}'\right]\end{aligned}$$

$$= -\mathrm{Im}\frac{L^5}{180D^2L_\omega^2}\varsigma(x/L),\quad L \ll L_\omega. \tag{5.21}$$

The ς function is a polynomial as shown in Fig.5.5. The same result can also be obtained directly by expanding the right hand side of Eq.(5.19) with respect to L/L_ω. Performing the remaining frequency integration in Eq.(5.16b):

$$-\,\mathrm{Im}\int\limits_{\varepsilon-eV/2}^{\varepsilon+eV/2} L_\omega^{-2}\frac{d\omega}{2\pi} = \frac{eV\varepsilon}{2\pi D}, \tag{5.22}$$

we hence arrive at

$$\delta\nu_2(\varepsilon,x) \approx \frac{eVL^5}{360\pi D^3}\varsigma(x/L),\ eV \ll E_{\mathrm{Th}} \tag{5.23}$$

in the low bias limit. We notice that $\varsigma(x/L)$, as well as $\delta\nu_2$, is an odd function with respect to $x = L/2$, and that it vanishes at $x = 0, L$. This particular x-dependence is in fact a generic property which can be easily deduced from Eq.(5.19). In addition, $\delta\nu_2$ is also an odd function of ε, which can be deduced from Eq.(B.13) since flipping the sign of ω is equivalent to taking the conjugate (and since $\delta\nu_2$ concerns only the imaginary part of the associated integrand).

If we are only concerned about $\delta\nu_2$ around the cusps of the DOS correction, namely $\delta\nu_2(\pm|\eta + eV/2|)$, we can alternatively apply the nonlinear limit $L \gg L_\omega$ to Eq.(5.19), which then reduces to $L_\omega^3(2x-L)/(8LD^2)$ for $0 < |x - L/2| < L/2$. As such, we get

$$\begin{aligned}\delta\nu_2(\pm\left|\eta + eV/2\right|, x) &\approx \pm\frac{2x-L}{8LD^2}\mathrm{Im}\int_\eta^{eV+\eta} L_\omega^3\frac{d\omega}{2\pi}\\ &= \pm\frac{2x-L}{8\pi L\sqrt{2D}}\left(\frac{1}{\sqrt{\eta}} - \frac{1}{\sqrt{eV+\eta}}\right),\ E_{\mathrm{Th}} \ll \eta.\end{aligned} \tag{5.24}$$

Both linear and nonlinear results suggest that the DOS correction should have a profile such that $|\delta\nu(eV/2,x)|$ is greater (lesser) than $|\delta\nu(-eV/2,x)|$ if $x < L/2$ ($x > L/2$), assuming the chemical potential of the left lead is higher. This point will be verified by our numerical simulation (see Fig.5.16 below). Besides, whether the interaction effect develops peaks or cusps on the DOS profile depends on the sign of $(2\mathcal{F} - 1)$ [see Eq.(5.15)]. It turns out that, for bulk metals, the AA effect always results in a negative DOS correction (i.e. a cusp) when the dynamic part of screened e-e interaction is taken into account [12].

5.1.2 Charge current

According to Eq.(2.8) the charge current can be expressed as

$$j(\mathbf{r}) = \frac{e\hbar}{2m}\int\frac{d\varepsilon}{2\pi}\lim_{\mathbf{r}\to\mathbf{r}'}\left(\nabla' - \nabla\right)G^<(\mathbf{r},\mathbf{r}',\varepsilon). \tag{5.25}$$

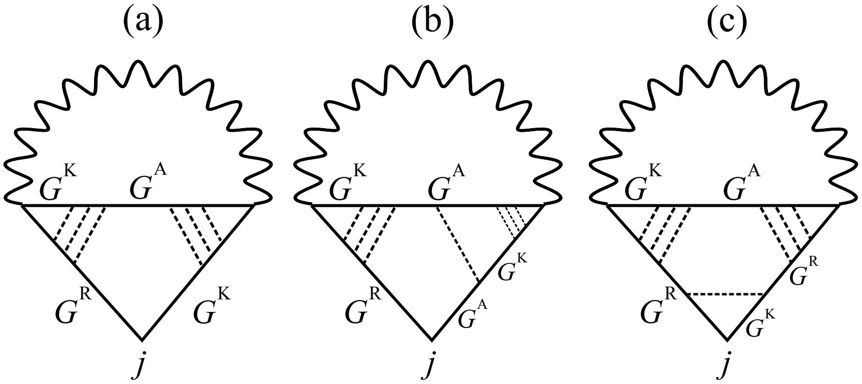

Figure 5.6: Diagram for the exchange (Fock) correction to charge current. These diagrams were first given in Ref.[126].

To comply with existing literatures [126, 127], we use the general relation $G^< = (G^{\rm K}-G^{\rm R}+G^{\rm A})/2$ to replace the $G^<$ in the above equation. Since $(G^{\rm R} - G^{\rm A})$ is symmetric under time reversal symmetry, it makes no contribution when $(\nabla' - \nabla)$ is applied. Thus our objective becomes calculating the interaction correction to $G^{\rm K}$. To the first order in e-e interaction, the correction to $G^{\rm K}$ reads

$$\delta G^{\rm K} \approx G^{\rm R}\Sigma^{\rm R}G^{\rm K} + G^{\rm K}\Sigma^{\rm A}G^{\rm A} + G^{\rm R}\Sigma^{\rm K}G^{\rm A}, \tag{5.26}$$

where the convolution relation as shown in Eq.(2.23c) is employed. Note that the first two terms on the right hand side of Eq.(5.26) contribute equally to the current since $G^{\rm R}\Sigma^{\rm R}G^{\rm K} = -[G^{\rm K}\Sigma^{\rm A}G^{\rm A}]^\dagger$. With $G^{\rm K}$ instead of $G^<$, the retarded self-energy is expressed as [cf. Eq.(5.2)]

$$\begin{aligned}\Sigma^{\rm R}(\mathbf{r}_1,\mathbf{r}_2,\varepsilon) &= -{\rm i}\delta(\mathbf{r}_1-\mathbf{r}_2)\int\frac{d\omega}{2\pi}\int d\mathbf{r}\; G^{\rm K}(\mathbf{r},\mathbf{r},\omega)U^{\rm R}(\mathbf{r}_1,\mathbf{r},0)\\ &+\frac{\rm i}{2}\int\frac{d\omega}{2\pi}\left[G^{\rm K}(\mathbf{r}_1,\mathbf{r}_2,\varepsilon-\omega)U^{\rm R}(\mathbf{r}_1,\mathbf{r}_2,\omega)+G^{\rm R}(\mathbf{r}_1,\mathbf{r}_2,\varepsilon-\omega)U^{\rm K}(\mathbf{r}_1,\mathbf{r}_2,\omega)\right],\end{aligned} \tag{5.27}$$

and the Keldysh self-energy:

$$\Sigma^{\rm K}(\mathbf{r}_1,\mathbf{r}_2,\varepsilon) = \frac{\rm i}{2}\int\frac{d\omega}{2\pi}\left[G^{\rm K}(\mathbf{r}_1,\mathbf{r}_2,\varepsilon-\omega)U^{\rm K}(\mathbf{r}_1,\mathbf{r}_2,\omega)\right]. \tag{5.28}$$

The terms containing $U^{\rm K}$ should be discarded when the AA effect is the prime concern, because they amount to higher order (in terms of the inverse dimensionless conductance given by Ohm's law) corrections related with the dephasing effect [23]. Thus the remaining terms in Eq.(5.26) all have the form $G^{\rm K}U^{\rm R}$.

Applying the same disorder-average technique as demonstrated in Sec.5.1.1, we obtain Fig.5.6 for the charge current correction. These diagrams were first obtained and calculated in Ref.[126]. Note that we have omitted showing the corresponding Hartree diagrams since they can be easily produced by reconnecting the interaction line (see Fig.5.3). To simplify the current vertex which contains the operator $(\nabla' - \nabla)$, we apply to it the Fourier transform $(\mathbf{r} - \mathbf{r}') \to \mathbf{k}$. As such, the charge current correction is now written

$$\delta j(\mathbf{R}) = \mathrm{i}\frac{e\hbar}{m}\int\frac{d\varepsilon}{2\pi}\int\frac{d\mathbf{k}}{(2\pi)^d}k_x\delta G^{\mathrm{K}}(\mathbf{k},\varepsilon,\mathbf{R}), \tag{5.29}$$

assuming the electric field is applied along $\hat{x}$.

Analogous to Eq.(5.5), the G^{K} in Fig.5.6 is approximated as

$$G^{\mathrm{K}}(\mathbf{kR},\varepsilon) \approx F(\varepsilon,\mathbf{R})\left[G^{\mathrm{A}}(\mathbf{k},\varepsilon) - G^{\mathrm{R}}(\mathbf{k},\varepsilon)\right] = \frac{F(\varepsilon,\mathbf{R})}{\mathrm{i}\tau_0}G^{\mathrm{A}}(\mathbf{k},\varepsilon)G^{\mathrm{R}}(\mathbf{k},\varepsilon), \tag{5.30}$$

where $F(\varepsilon,\mathbf{R})$ is given by

$$F(\varepsilon,x) = \left(1 - \frac{x}{L}\right)\tanh\frac{\varepsilon - eV/2}{2k_{\mathrm{B}}T} + \frac{x}{L}\tanh\frac{\varepsilon + eV/2}{2k_{\mathrm{B}}T}. \tag{5.31}$$

The diagram blocks which contain the e-e interaction vertex can be evaluated in the same way as in Sec.5.1.1, except that here G^{K} is substituted for $G^{<}$. The evaluation of the bottom block connected with the current vertex requires a bit more elaboration: the one in Fig.5.6(a) reads

$$\begin{aligned}&\int\frac{d\mathbf{k}}{(2\pi)^d}\frac{\hbar k_x}{m}G^{\mathrm{R}}(\mathbf{k},\varepsilon)G^{\mathrm{A}}(\mathbf{k}-\mathbf{q},\varepsilon-\omega)G^{\mathrm{K}}(\mathbf{k}\varepsilon,\mathbf{R}) \approx \\ &\int\frac{d\mathbf{k}}{(2\pi)^d}(\mathbf{v}_{\mathbf{k}}\cdot\hat{x})(-\mathbf{v}_{\mathbf{k}}\cdot\mathbf{q})\left[G^{\mathrm{A}}(\mathbf{k},\varepsilon)\right]^3\left[G^{\mathrm{R}}(\mathbf{k},\varepsilon)\right]^2\frac{F(\varepsilon,\mathbf{R})}{\mathrm{i}\tau_0} = -6\pi\nu_0\tau^3\frac{v_{\mathrm{F}}^2}{d}q_xF(\varepsilon,\mathbf{R}),\end{aligned} \tag{5.32}$$

where the Taylor expansion Eq.(B.7) and the identity Eq.(B.9) have been used. Note that, due to the presence of the current vertex, only the anisotropic terms are kept. Same techniques are applied to Fig.5.6(b), where the corresponding block is evaluated as

$$\begin{aligned}&\int\frac{d\mathbf{k}}{(2\pi)^d}(\mathbf{v}_{\mathbf{k}}\cdot\hat{x})(-\mathbf{v}_{\mathbf{k}}\cdot\mathbf{q})\left[G^{\mathrm{A}}(\mathbf{k},\varepsilon)\right]^3G^{\mathrm{R}}(\mathbf{k},\varepsilon)\gamma\int\frac{d\mathbf{k}'}{(2\pi)^d}G^{\mathrm{A}}(\mathbf{k}'-\mathbf{q},\varepsilon-\omega)G^{\mathrm{K}}(\mathbf{k}'\varepsilon\mathbf{R}) \\ &\approx 2\pi\nu_0\tau^3\frac{v_F^2}{d}q_xF(\varepsilon,\mathbf{R}).\end{aligned} \tag{5.33}$$

Should we keep adding dashed lines to Fig.5.6(b) in the middle, we would generate terms of the form $G^{\mathrm{A}}G^{\mathrm{A}} \sim \nu_0/\varepsilon$ [see Eq.(B.2)], which could thus be neglected. Figure 5.6(c) amounts to zero under the isotropic approximation of Eq.(5.30):

$$\int\frac{d\mathbf{k}}{(2\pi)^d}\frac{\hbar k_x}{m}G^{\mathrm{R}}(\mathbf{k},\varepsilon)G^{\mathrm{K}}(\mathbf{k}\varepsilon,\mathbf{R}) \approx 0. \tag{5.34}$$

Collecting all the pieces of Fig.5.6 and taking into account its Hartree counterpart, we arrive at

$$\delta j(\mathbf{R}) = -\frac{De\nu_0}{\pi}\mathrm{Im}\int d\varepsilon d\omega\int d\mathbf{R}'d\mathbf{R}''F(\varepsilon,\mathbf{R})\mathcal{P}(\omega,\mathbf{R},\mathbf{R}')F(\varepsilon-\omega,\mathbf{R}')$$

$$\times [U^{\mathrm{R}}(\mathbf{R}', \mathbf{R}'', \omega) - 2\mathcal{F}\bar{U}\delta(\mathbf{R}' - \mathbf{R}'')]\nabla_{\mathbf{R}}\mathcal{P}(\omega, \mathbf{R}'', \mathbf{R}) \cdot \hat{x}. \tag{5.35}$$

The $\hat{x} \cdot \nabla_{\mathbf{R}}$ operator is a real-space translation of the $\mathrm{i}q_x$ factor generated from Eq.(5.32).

In the following, we shall show that the interaction correction to the linear conductivity, which was derived in Ref.[21] using Kubo formula, can be reproduced from the general expression of Eq.(5.35). To this end, we first notice that in the linear-response regime ($k_BT \gg eV$)

$$F_0(\varepsilon + eV) - F_0(\varepsilon) \approx eV\frac{\partial}{\partial\varepsilon}F_0(\varepsilon), \tag{5.36}$$

where $F_0(\varepsilon) = \tanh(\varepsilon/2k_{\mathrm{B}}T)$, and hence

$$\begin{aligned}\int F(\varepsilon, x)F(\varepsilon - \omega, x')d\varepsilon &\to \frac{V}{L}\int d\varepsilon F_0(\varepsilon - \omega){F_0}'(\varepsilon)x + F_0(\varepsilon){F_0}'(\varepsilon - \omega)x' \\ &= \frac{eV}{L}(x - x')\int d\varepsilon \tanh\frac{\varepsilon - \omega}{2k_BT}\frac{\partial}{\partial\varepsilon}\tanh\frac{\varepsilon}{2k_BT} \\ &= \frac{2eV}{L}(x' - x)\frac{\partial}{\partial\omega}\left(\omega\mathrm{coth}\frac{\omega}{2k_BT}\right).\end{aligned} \tag{5.37}$$

Next, the resulting factor $(x - x')$ is put together with $\mathcal{P}(\omega, \mathbf{R}, \mathbf{R}')$, thereby yielding

$$(x - x')\mathcal{P}(\omega, \mathbf{R}, \mathbf{R}') \to \mathrm{i}\frac{\partial\mathcal{P}(\omega, \mathbf{q})}{\partial q_x} = -2\mathrm{i}Dq_x\mathcal{P}^2(\omega, \mathbf{q}) \tag{5.38}$$

after Fourier transform, where Eq.(B.11) has been invoked to obtain the second equality. The spatial integrations in Eq.(5.35) can hence be performed using the convolutional theorem of Fourier transform. The result indicates a linear relation between the current and the bias voltage. Reading off their ratio, we get the conductivity correction:

$$\delta\sigma = -\frac{2\nu_0e^2D^2}{\pi d}\int d\omega\frac{\partial}{\partial\omega}\left(\omega\mathrm{coth}\frac{\omega}{2k_BT}\right)\int\frac{d\mathbf{q}}{(2\pi)^d}q^2\mathrm{Im}\left[(U^{\mathrm{R}}(\mathbf{q}\omega) - 2\mathcal{F}\bar{U})\mathcal{P}^3(\mathbf{q}\omega)\right], \tag{5.39}$$

which is the original linear-response result obtained by Altshuler and Aronov [12, 21]. For $d \leq 2$ Eq.(5.39) leads to a singular suppression to the conductivity as temperature approaches zero [21].

For a finite wire sandwiched between electrodes, one has to compute the spatial integrals in Eq.(5.35) directly in real-space. To simplify our calculation, we adopt Eq.(5.12) again and thus obtain

$$\delta I = -\frac{(1 - 2\mathcal{F})De}{2\pi}\mathrm{Im}\int d\omega d\varepsilon\int dx' F(\varepsilon, x)\mathcal{P}(\omega, x, x')F(\varepsilon - \omega, x')\partial_x\mathcal{P}(\omega, x', x) \tag{5.40}$$

in one-dimension. At this point, it is important to notice that the result of Eq.(5.40) explicitly depends on the coordinate x, thus breaking the current continuity. This issue results from the various approximations we have made in order to simplify our diagram calculation. As a compromise, one

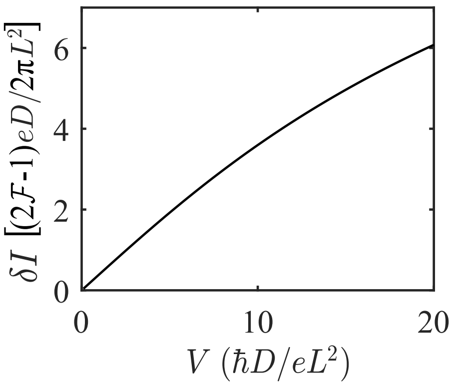

Figure 5.7: $\delta I - V$ curve generated from Eq.(5.44) for a disordered wire at zero temperature. δI is the charge current correction to the first order in e-e interaction.

could either take the average value $L^{-1}\int \delta I(x)dx$ or simply use $\delta I(x = L/2)$ to get an unbiased result. It can be shown that these two approaches will make no qualitative difference in the end. Here we choose the latter approach, i.e. $\delta I = \delta I(x = L/2)$.

To proceed from Eq.(5.40) we plug in

$$\frac{\partial}{\partial x}\mathcal{P}(x,x',\omega) = \begin{cases} \frac{\sinh(x'/L_\omega)\cosh(L-x)/L_\omega}{-D\sinh(L/L_\omega)}, \ x > x' \\ \frac{\cosh(x/L_\omega)\sinh(L-x')/L_\omega}{D\sinh(L/L_\omega)}, \ x < x' \end{cases} \tag{5.41}$$

Besides, the ε-integration yields

$$\int F(\varepsilon,x)F(\varepsilon-\omega,x')d\varepsilon = \begin{cases} \frac{2\hbar\omega}{L}(x'-x) + \frac{(eV-\hbar\omega)}{L^2}(2x-L)(2x'-L), \ |\hbar\omega| \le eV \\ \mathrm{sgn}(\omega)\frac{2eV}{L}(x'-x) + (eV-\hbar\omega), \ |\hbar\omega| > eV \end{cases} \tag{5.42}$$

at zero temperature (or in the limit $k_BT \ll eV$). The spatial integral in Eq.(5.40) thus reads[2]

$$\begin{aligned} &\int_0^L (x-x')\mathcal{P}(\omega,x,x')\frac{\partial}{\partial x}\mathcal{P}(\omega,x',x)dx' \\ &= \frac{L_\omega^3}{16D^2\sinh^2(L/L_\omega)}\left[\sinh\frac{2(L-x)}{L_\omega}\left(1+\frac{2x^2}{{L_\omega}^2}-\cosh\frac{2x}{L_\omega}\right)+x\to(L-x)\right], \end{aligned} \tag{5.43}$$

where x will be set at $L/2$ in the following. The remaining ω-integration can be simplified with $\mathrm{Im}\int_{-\infty}^{+\infty}d\omega \to 2\mathrm{Im}\int_0^{+\infty}d\omega$ since ω enters the integrand through $\mathcal{P}$ which satisfies $\mathcal{P}(-\omega) = \mathcal{P}(\omega)^*$. To further simplify the notation, we introduce $y = L/L_\omega$, $\Upsilon(y) = \frac{1+y^2/2-\cosh y}{\sinh y}$, and $b = \sqrt{eVL^2/(\mathrm{i}\hbar D)}$. As such Eq.(5.40) is rewritten as

$$\delta I = \frac{(1-2\mathcal{F})eD}{2\pi L^2}\mathrm{Im}\left\{\frac{\mathrm{i}eVL^2}{\hbar D}\int_b^\infty \frac{\Upsilon(y)}{y^2}dy - \int_0^b \Upsilon(y)dy\right\}. \tag{5.44}$$

---

[2] Those terms in Eq.(5.42) which are not linear to $(x-x')$ do not contribute once either $x = L/2$ is applied or the average is taken over x.

The remaining integrals in Eq.(5.44) are evaluated numerically. Note that the integrals are carried out along $0 \to (+\infty - \mathrm{i}\infty)$ and that the integrands are analytic functions on the complex plane. Besides, the first integral above can be split in two for numeric convenience: $\int_b^\infty \to \int_b^M -1/M$, since $\Upsilon(y)$ approaches -1 rapidly. The computed $\delta I - V$ curve is plotted in Fig.5.7. Evidently, the only relevant energy scale involved in Eq.(5.44) is the Thouless energy $E_{\mathrm{Th}} = \hbar D/L^2$. Nevertheless, the $\delta I - V$ curve appears linear over a large range of the ratio eV/E_{Th}, with a slight tendency to bend down at a high eV/E_{Th} ratio.

The asymptotic behavior of Eq.(5.44) is as follows. At high voltages $eV \gg E_{\mathrm{Th}}$, Eq.(5.44) reduces to

$$\delta I \approx \frac{(2\mathcal{F}-1)e}{\pi}\sqrt{\frac{DeV}{2\hbar L^2}},\ eV \gg E_{\mathrm{Th}}, \tag{5.45}$$

and in the low bias limit, the linear conductance correction is obtained: $\delta\mathcal{G} = d\delta I/dV \approx 0.4(2\mathcal{F}-1)e^2/h$. If we were to use a bare local potential, i.e. $U_0 \approx U\delta(\mathbf{R}_1 - \mathbf{R}_2)$, we would instead get

$$\delta\mathcal{G} \approx (0.8e^2/h)U\nu_0. \tag{5.46}$$

This latter scenario is more relevant to our numerical model, since the interaction strength can be treated as an input parameter therein. Interestingly, these asymptotic behaviors of δI, derived under the local interaction model, turn out to be very similar (up to a prefactor) to the result of Ref.[126], which was derived with a dynamically screened interaction.

The result that $\delta\mathcal{G}$ is independent on the system size L signifies a divergence in the linear conductivity $\delta\sigma$ in the $L \to \infty$ limit, since $\delta\sigma = \delta\mathcal{G} \cdot L$ in one-dimension. This result is consistent with the original AA theory [12, 21], in which the system is assumed to be thermodynamic so that the limit $L \to \infty$ is applied at first, and then the divergence in $\delta\sigma$ is observed as $T \to 0$.

5.2 Numerical implementation

In the previous section of analytical calculations, a few simplifications have been made in order to facilitate the derivations. For example, the quasi-equilibrium assumption that we imposed through Eq.(5.30), and that all the correlators of the form $\langle G^{\mathrm{R}}G^{\mathrm{R}}\rangle$ were discarded so as to simplify the diagrams. Moreover, in calculating those diagrams, we divided them rigidly into long or short ranged blocks and conquered them in a separate manner. By doing so, we have completely overlooked the coupling at the intermediate scales: those blocks are meant to be connected smoothly after all. A crucial dissatisfaction caused by these simplifications was seen to be the charge current discontinuity as manifested by Eq.(5.40).

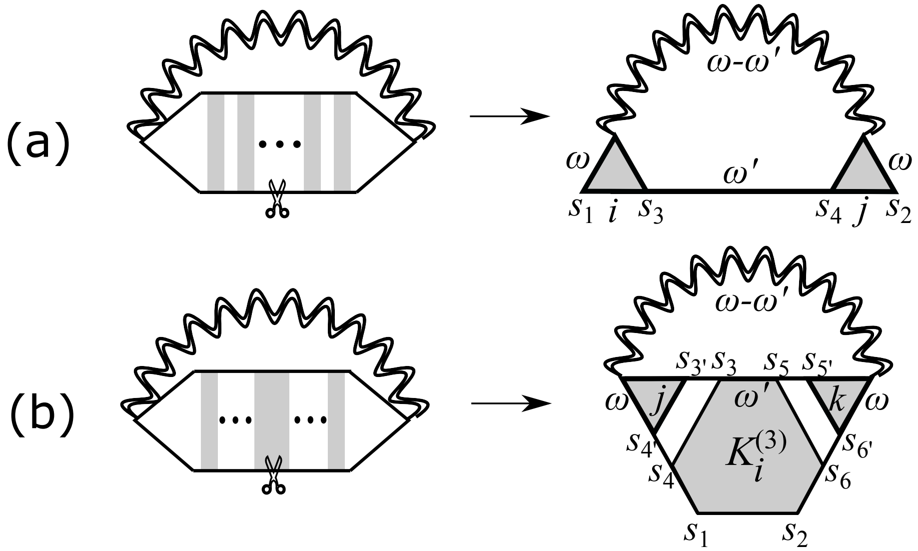

Figure 5.8: Deriving the Fock-exchange self-energy from the corresponding Luttinger-Ward diagram. In (b) a G-line is removed from inside of a $K^{(2)}$-kernel (grey rectangle), which produces a $K^{(3)}$ (the grey hexagon). The i, j, k indices denote real-space sites, ω denotes frequency, and s denotes contour branch. The wiggly line represents the e-e interaction, which is chosen to be either bare or screened by the procedure indicated in Fig.4.1 in our numerical calculations below.

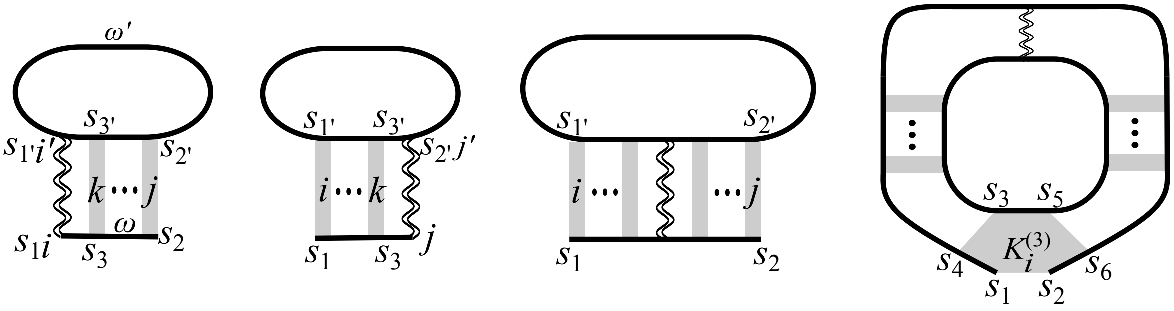

Figure 5.9: Hartree self-energy diagrams.

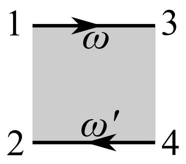

Figure 5.10: Demonstration of the index layout for two-particle Green's functions. Note that a different indexing convention was used in Sec.2.2.2.

To remove the unnecessary simplifications and to restore the current continuity, we shall place our numerical calculations on a more solid ground. To this end, we follow the more rigorous Kadanoff-Baym procedure and re-derive the self-energy diagrams from the first-order Φ-diagrams dressed by diffuson [34]. Figure 5.8 illustrates this procedure when applied to the Fock-exchange diagram. In the figure each line represents the disorder-averaged Green's function generated from the self-consistent CPA calculation. The grey stripes are the diffuson ladder composed of $K^{(2)}$-kernels (see details below). Since the $K^{(2)}$-kernel under CPA contains Green's functions in itself, removing such an internal G-line leads to a $K^{(3)}$-diagram, as demonstrated by Fig.5.8(b). The exchange self-energy should be the sum of Fig.5.8(a) and (b). The Hartree diagrams are derived in a similar fashion; they are shown in Fig.5.9. In the following we shall go through the computational scheme for these diagrams.

As stated in Sec.2.3.2, for numerical computations it is more convenient to work under the Green's function representation Eq.(2.16) instead of the triangular form Eq.(2.18). To this end, we need to first transform the impurity locator defined in Eq.(3.17a) to its $\overset{\supset}{\mathbf{G}}$-representation by using Eq.(2.19). The two-particle locator is redefined accordingly as [cf. Eq.(3.17b)]

$$g^{(2)}_{i\omega\omega'}(s_1s_2,s_3s_4)=\overline{g_{v_i\omega}(s_1,s_3)g_{v_i\omega'}(s_4,s_2)}^{v_i},\tag{5.47}$$

where the indices have been rearranged as per Fig.5.10. The Bethe-Salpeter equation for the locators are thus written

$$\begin{aligned}g^{(2)}_{i\omega\omega'}(s_1s_2,s_3s_4)&=[g*g]_{i\omega\omega'}(s_1s_2,s_3s_4)\\&\quad+[g*g]_{i\omega\omega'}(s_1s_2,s_{3'}s_{4'})\cdot K^{(2)}_{i\omega\omega'}(s_{3'}s_{4'},s_{1'}s_{2'})\cdot g^{(2)}_{i\omega\omega'}(s_{1'}s_{2'},s_3s_4),\end{aligned}\tag{5.48}$$

where $[g*g]_{i\omega\omega'}(s_1s_2,s_3s_4)=g_{i\omega}(s_1s_3)g_{i\omega'}(s_4s_2)$, and note that all the repeated s-indices should be summed over. Viewing $g^{(2)}$, $[g*g]$, and $K^{(2)}$ as 4×4 matrices, we can hence express $K^{(2)}$ using Eq.(5.48): $K^{(2)}_i=[g*g]^{-1}_i-\left(g^{(2)}_i\right)^{-1}$, for each pair of ω,ω'.

In order to calculate $K^{(3)}_i$ we make use of the fact that it must satisfy the diagrammatic equation of Fig.2.7(b) [also see Eq.(2.34)] when all the objects therein are restricted on the local site [1]. The correlators $C^{(n)}$ in Fig.2.7 are accordingly replaced with the disorder-averaged locators $g^{(n)}_i$,

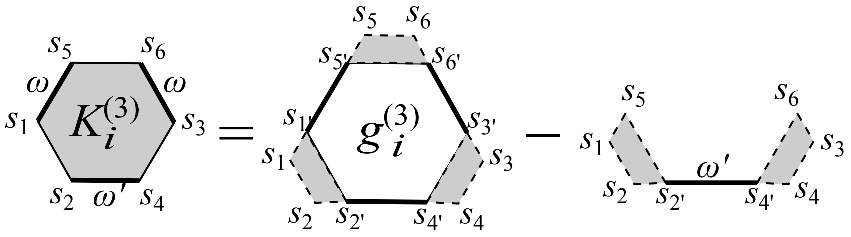

Figure 5.11: Diagrammatic illustration for Eq.(5.49). $g_i^{(3)}$ is the third order locator averaged over the local potential.

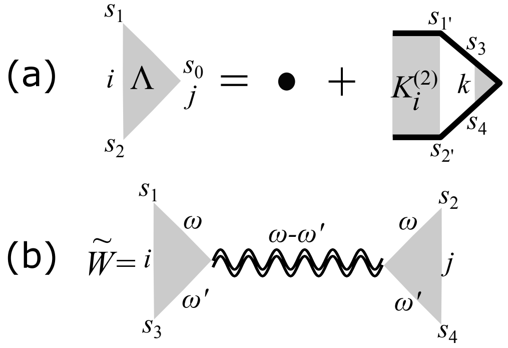

Figure 5.12: (a) Recursive relation for the vertex correction. (b) Dressed e-e interaction.

which are computed in a similar fashion as Eq.(5.47). To solve for $K_i^{(3)}$ we multiply the matrix $\left(g_i^{(2)}\right)^{-1}$ on both sides of Fig.2.7(b) from all three directions, and thence obtain

$$K^{(3)}_{i\omega\omega\omega'}(s_1s_2, s_3s_4, s_5s_6) = g^{(3)}_{i\omega\omega\omega'}(s_{1'}s_{5'}, s_{6'}s_{3'}, s_{4'}s_{2'}) \cdot g^{(2),-1}_{i\omega\omega'}(s_1s_2, s_{1'}s_{2'}) \cdot g^{(2),-1}_{i\omega\omega'}(s_{3'}s_{4'}, s_3s_4)$$
$$\cdot\, g^{(2),-1}_{i\omega\omega}(s_{5'}s_{6'}, s_5s_6) - [g*g]^{-1}_{i\omega\omega'}(s_1s_2, s_5s_{2'}) \cdot g_{i\omega'}(s_{4'}s_{2'}) \cdot [g*g]^{-1}_{i\omega\omega'}(s_6s_{4'}, s_3s_4), \tag{5.49}$$

as illustrated in Fig.5.11.

Another building block of Fig.5.8 is the disorder-induced vertex correction

$$\Lambda_{\omega\omega'}(s_1s_2i, s_0j) = \delta_{s_1s_2}\delta_{s_1s_0}\delta_{ij} + K^{(2)}_{i\omega\omega'}(s_1s_2, s_{1'}s_{2'}) \cdot [G*G]_{\omega\omega'}(s_{1'}s_{2'}i, s_3s_4k) \cdot \Lambda_{\omega\omega'}(s_3s_4k, s_0j), \tag{5.50}$$

where $[G*G]_{\omega\omega'}(s_{1'}s_{2'}i, s_3s_4k) = G_\omega^{s_{1'}s_3}(i,k) \cdot G_{\omega'}^{s_4s_{2'}}(k,i)$, as illustrated in Fig.5.12(a). Under each pair of ω, ω', Λ is a $4N \times 2N$ matrix[4] and can be solved from the linear equation (5.50). The diffuson dressed polarization is thus written [cf. Eq.(2.44)]

$$P_\omega^{s_1s_2}(i,j) = \int \frac{d\omega'}{\mathrm{i}\pi}[G*G]_{\omega+\omega',\omega'}(s_1s_1i, s_3s_4k) \cdot \Lambda_{\omega+\omega',\omega'}(s_3s_4k, s_2j). \tag{5.51}$$

---

[4] N is the number of lattice sites between leads. The notation s_3s_4k, as a matrix index, should be interpreted as $(s_3 + 2 \cdot s_4 + 4 \cdot k)$.

$P^{\mathrm{R},<,\mathrm{A}}$ are then obtained by using the transformation (2.19), which allows for computing the screened interaction with Eq.(4.7). As can be seen in Fig.5.8, the interaction vertex W is subject to being dressed with Λ at the ends:

$$\tilde{W}_{\omega\omega'}(s_1s_3i, s_2s_4j) = \Lambda_{\omega\omega'}(s_1s_3i, sk) \cdot W^{ss'}_{\omega-\omega'}(k,l) \cdot \Lambda_{\omega'\omega}(s_4s_2j, s'l), \tag{5.52}$$

as illustrated in Fig.5.12(b). Collecting all the pieces, we get the exchange part of the self-energy (Fig.5.8) as follows:

$$\begin{aligned} \Sigma^{s_1s_2}_{\mathrm{X},\omega}(i,j) = &- \int \frac{d\omega'}{2\pi\mathrm{i}} G^{s_3s_4}_{\omega'}(i,j) \cdot \tilde{W}_{\omega\omega'}(s_1s_3i, s_2s_4j) + \int \frac{d\omega'}{2\pi\mathrm{i}} G^{s_1s_2}_{\omega'}(i,j) \cdot W^{s_1s_2}_{\omega-\omega'}(i,j) \\ &- \delta_{ij} \int \frac{d\omega'}{2\pi\mathrm{i}} \Big([G*G]\tilde{W}[G*G] \Big)_{\omega\omega'}(s_4s_3i, s_6s_5i) \cdot K^{(3)}_{i\omega\omega\omega'}(s_6s_5, s_4s_3, s_2s_1), \end{aligned} \tag{5.53}$$

where the GW self-energy (the second term on the right hand side) without disorder vertices has been excluded, for it is computed in a separate routine. In order to write down the expression for the Hartree part (Fig.5.9), we introduce the following new diagrammatic elements, viz. the ladder-sum

$$\mathcal{L} = (I_{4N} - K^{(2)}[G*G])^{-1} K^{(2)}, \tag{5.54}$$

where $K^{(2)}$ denotes a $4N \times 4N$ diagonal block matrix with ith block being $K^{(2)}_i$, and the interaction block

$$\Theta_{\omega\omega'}(s_1s_{1'}i, s_2s_{2'}i') = G^{s_1s_3}_{\omega}(i,j) \cdot G^{s_3s_2}_{\omega}(j,i') \cdot G^{s_{2'}s_{3'}}_{\omega'}(i',j') \cdot G^{s_{3'}s_{1'}}_{\omega'}(j',i) \cdot W^{s_3s_{3'}}_0(j,j'), \tag{5.55}$$

which resembles the diagram on the right in Fig.5.3. Note that the Hartree diagram only concerns the *static* interaction W_0 whose frequency is set at zero. Given the expressions for all building blocks, Fig.5.9 is thence translated into

$$\begin{aligned} \Sigma^{s_1s_2}_{\mathrm{H},\omega}(i,j) = &\int \frac{d\omega'}{\pi\mathrm{i}} G^{s_1s_3}_{\omega}(i,k) \cdot G^{s_{3'}s_{1'}}_{\omega'}(k,i') \cdot G^{s_{1'}s_{2'}}_{\omega'}(i',j) \cdot W^{s_1s_{1'}}_0(i,i') \cdot \mathcal{L}_{\omega\omega'}(s_3s_{3'}k, s_2s_{2'}j) \\ &+ \int \frac{d\omega'}{\pi\mathrm{i}} G^{s_3s_2}_{\omega}(k,j) \cdot G^{s_{2'}s_{3'}}_{\omega'}(j',k) \cdot G^{s_{1'}s_{2'}}_{\omega'}(i,j') \cdot W^{s_1s_{1'}}_0(j,j') \cdot \mathcal{L}_{\omega\omega'}(s_1s_{1'}i, s_3s_{3'}k) \\ &+ \int \frac{d\omega'}{\pi\mathrm{i}} G^{s_{1'}s_{2'}}_{\omega'}(i,j) \cdot [\mathcal{L}\Theta\mathcal{L}]_{\omega\omega'}(s_1s_{1'}i, s_2s_{2'}j) \\ &+ \delta_{ij} \int \frac{d\omega'}{\pi\mathrm{i}} K^{(3)}_{i\omega\omega\omega'}(s_6s_5, s_4s_3, s_2s_1) \cdot [(I + [G*G]\mathcal{L})\Theta(\mathcal{L}[G*G] + I)]_{\omega\omega'}(s_4s_3i, s_6s_5i), \end{aligned} \tag{5.56}$$

with spin degeneracy already taken into account. Note that, if one wishes to calculate $\Sigma^{\mathrm{R},<}$, the transformation (2.47) needs to be applied to the results of Eqs.(5.53) and (5.56).

The physical quantities such as DOS and charge current are extracted from the Green's function, whose first order correction (δG) involves a disorder-average of the form $C^{(3)}$. According to the theory of Sec.2.2.2, every pair of G-lines in the $C^{(3)}$-diagram need to be dressed with a ladder series. Therefore, δG is written

$$\delta G(1,2) = C^{(2)}(12,34) \cdot [\Sigma_{\mathrm{H}}+\Sigma_{\mathrm{X}}](3,4), \tag{5.57}$$

where

$$C^{(2)}(12,34) = G(1,3)G(4,2) + G(1,1')G(2',2)\mathcal{L}(1'2',3'4')G(3',3)G(4,4'). \tag{5.58}$$

The composite index (e.g. 1) denotes a tuple (i,s), and the index layout of $C^{(2)}$ here corresponds to Fig.5.10 (cf. Fig.2.7a). Note that the vertex correction procedure of Eq.(5.57) is particularly important for ensuring charge conservation in transport calculations.

5.3 Numerical studies

The numerical formalism presented above is implemented with the lattice model as introduced in Sec.2.5.4. To make correspondence with the short wire model analyzed in Sec.5.1, in our simulations we consider strict one-dimensional systems with $W = 1$. Besides, the temperature is always set at zero.

We start with the simplest interacting model where the nonlocal interaction is omitted, i.e. $U_{i\neq j} = 0$. Since the local interaction arises from electrons of opposite spins, the Fock contribution vanishes to the first order in U_0. This scenario corresponds to setting $\mathcal{F} = 1$ in the analytical results presented in Eqs.(5.13) and (5.44). The second order correction in U_0 involves a dressed e-e interaction of the form UPU, where P is the polarization addressed in Eq.(5.51). In the diffusion approximation, it can be shown that [12]

$$P(\mathbf{q},\omega) \approx 2\nu_0 \frac{Dq^2}{-\mathrm{i}\omega + Dq^2}. \tag{5.59}$$

In the low frequency regime where the AA effect sets in, $P(\mathbf{q},\omega)$ tends to be constant. In other words, P is short-ranged in real space, and hence the second order correction effectively contributes a numeric factor to the bare interaction U_0. The same argument can be applied to all the bubble diagrams in the series of screened interaction (see Fig.4.1). Therefore, at this point, we only keep the first order correction in U_0, and, since $\mathcal{F} = 1$ in this case, we foresee a positive correction to both the DOS and the charge current.

Figure 5.13(a) displays the computed charge current correction in a one-dimensional lattice with $L = 40a$. As can be seen, the overall $\delta I - V$ trend agrees very well with the analytical prediction Fig.5.7, and in particular its nonlinear tendency appears minor. $\delta I - V$ curves under three

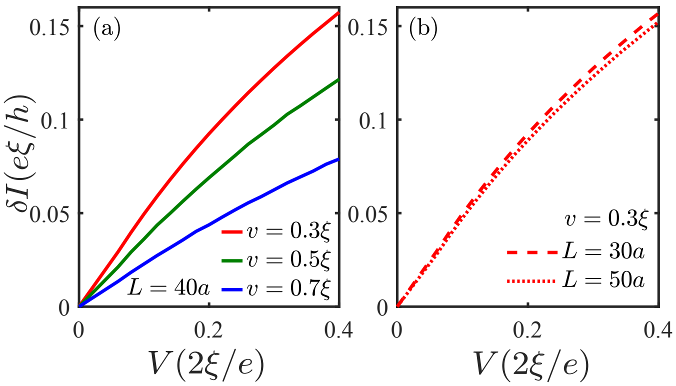

Figure 5.13: $\delta I - V$ relation calculated using the discrete lattice model under the setting $U_0 = \xi, U_{ij} = 0$ and a binary disorder. δI stands for the charge current correction to the first order in U_0. (a) The system size is set at $L = 40a$ while the disorder strength is varied by tuning the impurity potential v. (b) Results for $L = 30a, 50a$ under $v = 0.3\xi$.

different disorder strengths are plotted in Fig.5.13(a), from which we see that δI decreases with an increasing disorder strength. This behavior can be understood with Eq.(5.45), as the nonlinear current correction is proportional to $\sqrt{D}$, where D stands for diffusion constant. In the linear regime, as indicated by Eq.(5.46), the conductance is proportional to the noninteracting DOS (ν_0), which decreases with an increasing disorder strength. In contrast to the disorder strength, the wire length L is found less effective to δI, as illustrated in Fig.5.13(b). Indeed the linear conductance correction Eq.(5.46) has no dependency on L. Nevertheless, the nonlinear current predicted by Eq.(5.45) is proportional to L^{-1}, which explains the slight drop of δI at large V as L increases.

In the following we investigate the AA correction to the DOS profile. As discussed in Sec.5.1.1, the DOS correction is overall dominated by the symmetric part $\delta\nu_1$, which can be well represented by the result at the middle of the chain [see Eqs.(5.16a) and (5.18)]. The numerical result from our simulation is displayed in Fig.5.14. The solid curves mark the nonequilibrium results obtained under a bias of $V = 0.4\xi/e$. Those obtained under zero bias with otherwise same system parameters are marked by the dashed curves. Firstly, we notice that the peaks of $\delta\nu$ align very well with the respective Fermi energies of the leads, with the exception of short wires [e.g. the black curve in Fig.5.14(b)] whose linear-nonlinear crossover sets in at a much higher bias due to its large Thouless energy. For those curves that clearly display the nonlinear feature, i.e. those with split peaks, their peak values are nearly half of those obtained in equilibrium, which is consistent with Eq.(5.16a). Furthermore, the peak values increase with increasing disorder strength [see Fig.5.14(a)], and particularly they increase linearly versus the system size L [see Fig.5.14(b)]. These observations can be well understood with Eq.(5.17). To investigate the contribution from the asymmetric part $\delta\nu_2$

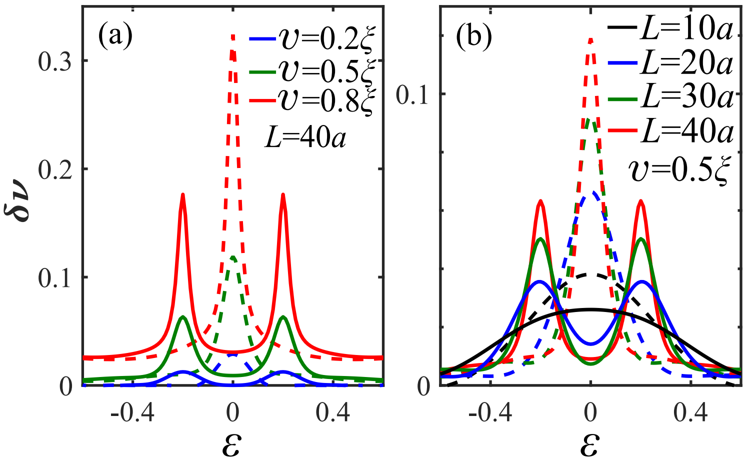

Figure 5.14: DOS corrections at the middle of the model wire. The interaction is assumed to be local. The solid lines mark the nonequilibrium results obtained under $V = 0.4\xi/e$. The dashed lines mark the corresponding results obtained in equilibrium (i.e. $V = 0$). (a) The system size L is fixed while the disorder strength v varies. (b) The other way around.

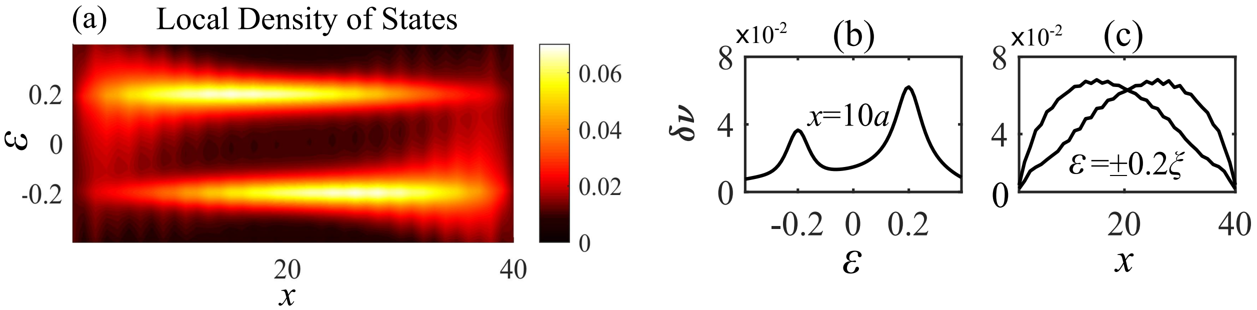

Figure 5.15: (a) Complete profile of the local DOS correction as a function of position and energy in a system of $L = 40a$, $U_{ij} = 0$, and $v = 0.5\xi$. (b) Cut at $x = 10a$. (c) Cut at $\varepsilon = \pm eV/2$.

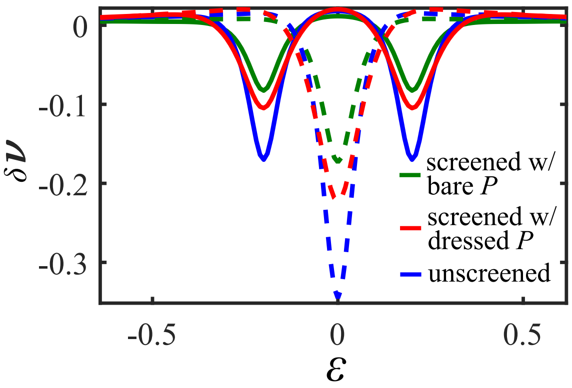

Figure 5.16: DOS correction from the Fock contribution (Fig.5.8) at the middle of the model wire ($L = 40a, v = 0.5\xi$). The interaction takes the form $U_{ij} = ua/|x_i - x_j|$. Blue curve: The bare interaction U_{ij} is used in the diagram. Red curve: Screening is taken into account via Eq.(4.7) where the polarization P is dressed with vertex correction. Green curve: The screened interaction is calculated with the bare polarization, i.e. without vertex correction. Dashed curves: corresponding equilibrium results.

[see Eq.(5.16b)], we plot the full profile of $\delta\nu(\varepsilon, x)$ at a given L and v [see Fig.5.15(a)]. In particular we observe that, away from the middle point $x = L/2$, the two peak values of $\delta\nu$ are not equal [see Fig.5.15(b)], and that their relative heights [see Fig.5.15(c)] have the x-dependancy as theoretically predicted in Sec.5.1.1.

So far we have seen that the numerical results for the local interaction model agrees very well with our theoretical prediction. In what follows, we switch to a long-range interaction modeled by $U_0 = 0, U_{ij} = ua/|x_i - x_j|$, which was not accounted for by the theoretical analyses of Sec.5.1. In particular we shall investigate the effects of many-body screening and the associated energy relaxation on the DOS correction in our model system. To this end, we compute the effective interaction using Eq.(4.7), with a polarization either dressed by the diffuson or not, and substitute the dynamic interaction into the diagrams of Fig.5.8. Figure 5.16 displays the result calculated for the Fock contribution to the DOS correction. Since the Fock contribution corresponds to $\mathcal{F} = 0$ in Eq.(5.15), it gives rise to cusps (negative corrections) instead of peaks in the DOS profile. Both the red and the green curves in Fig.5.16 are obtained with the screening effect being taken into account. The difference is that, for the red curves a dressed polarization [see Eq.(5.51)] is used where the disorder vertex correction is included, whereas the bare polarization is used for the green curves. Both results show a screening induced suppression of the DOS correction in comparison to that calculated with the bare interaction (blue curves). We also observe that the screening with dressed polarization (red curves) appears less effective. This reflects the fact that diffusion in general tends to hinder the screening process.

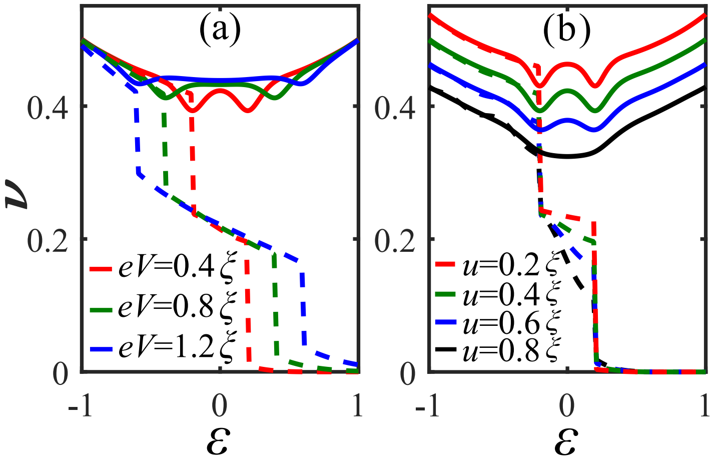

Figure 5.17: Energy relaxation effects on the DOS correction under differing bias voltages (a) and interaction strengths (b). The dashed curves represent the self-consistently computed energy distributions at the middle of the wire [see Fig.4.5]. The AA correction to DOS is computed with the diagram of Fig.5.8 using the self-consistent Green's function which corresponds to the dashed result. The solid curves are given by the self-consistent Green's function minus the AA correction.

Thus far our diagram calculations have relied on the disorder-average, yet noninteracting Green's function. This approach is only valid when the energy relaxation length is much longer than L. Ideally the effect of energy relaxation should be determined self-consistently within the numerical formalism. To this end, we employ the self-consistent GW-CPA scheme as presented in chapter 4 and insert the thus generated Green's function into the diagram of Fig.5.8 to compute the DOS correction. We carry out computation based on the result of Fig.4.5. Figure 5.17 displays the DOS with AA correction taken into account. From Fig.5.17(a) it can be observed that the AA correction tends to be suppressed as the bias increases. This effect can be attributed to the smeared step function in the energy distribution (dashed curves): one can see from Eq.(5.13) that the DOS anomaly depends on the sharpness of the distribution function $f(\varepsilon)$. Such mechanism is akin to the temperature induced smearing of DOS anomaly as reported in Ref.[130]. The effect of increasing interaction strength is two-fold. First, it enhances the equilibration process just like the effect of bias increase, as already explained in Sec.4.2.1. Second, the enhanced energy relaxation tends to smear the zero-frequency peak of the diffuson, since the diffusive motion of single particles no longer conserves energy in the presence of inelastic e-e scattering. Consequently, as the interaction increases, the two-cusp structure in the DOS profile tends to be smeared [see the black curve in Fig.5.17(b)].

5.4 Summary

In this chapter we developed a real-space diagrammatic formalism for computing the Altshuler-Aronov (AA) effects on the DOS and the electronic transport of mesoscopic structures. Different from macroscopic samples, in finite mesoscopic systems the AA effects are subject to the nonlinear external bias and the cutoff due to system size. Specifically, we found that in short diffusive wires the DOS anomaly should split in two at the respective lead Fermi energies, and that it grows linearly with respect to the wire length. In addition, in the nonlinear transport regime, the value of the DOS correction acquires a nonsymmetric position-dependence along the wire. Effects of dephasing and energy relaxation have also been considered using the screened interaction and self-consistent iterations. Both effects were found to smear the interaction induced DOS anomaly. Under the locally interacting model, the charge current correction was computed to the first order in interaction. Its magnitude was found to decrease with an increasing disorder strength or system length.

Chapter 6

Conclusions

Based on the nonequilibrium Green's functions and the many-body perturbation technique, we have developed a practical formalism to compute a variety of quantum effects in disordered mesoscopic systems. To ensure the property of charge conservation on transport quantities, we have applied the Kadanoff-Baym scheme to our theoretical constructions, which start with a certain Luttinger-Ward diagram and generate self-energy diagrams by respectively removing each Green's function line from it. In the Keldysh formalism, the Feynman diagrams have the same structures as their equilibrium counterparts, except that at each vertex an extra index is introduced to track the branches of the Keldysh contour. We have implemented the real-space Green's function formalism on a ribbon-like lattice model, which numerically simulates a quasi-one-dimensional mesoscopic system. In our transport calculations, the effects of electronic reservoirs are taken care of by treating part of the lattice as thermal equilibrium leads, whose self-energies are exactly computed. Following this methodology we have studied three particular quantum effects in disordered mesoscopic systems: weak localization, energy relaxation, and the Altshuler-Aronov effect. In particular, the last two are many-body effects associated with the e-e interaction.

For noninteracting disordered systems, we implemented the coherent potential approximation (CPA) and the dual fermion (DF) method respectively to calculate the quantum diffusion and localization effects in dc transport coefficients. We showed that CPA corresponds to a diffusion approximation in the transport calculation, while DF incorporates the Cooperon process responsible for the localization effect. From numerical simulations it was found that both methods predict linear $I - V$ relations for a uniformly disordered quantum wire. Whereas DF performs better than CPA overall, there exists certain disorder strength threshold beyond which numerical instability could occur in DF computations. Besides, we noticed that the DF method does not strictly respect the law of charge current continuity. To remedy this inaccuracy the computed current needs be averaged along the transport system. When disorder is weak enough, one could alternatively replace all double-dashed lines in Fig.3.10 with single-dashed lines (see Fig.3.2); the resulting diagrammatic scheme for the real fermion strictly follows the Kadanoff-Baym scheme and thus respects conservation laws.

Combining CPA with GW approximation, we developed a self-consistent formalism for interacting disordered systems. In particular we employed this formalism to study the energy relaxation effects in nonequilibrium quantum wires. By calculating the electronic energy distribution we found that the two separate Fermi surfaces in nonequilibrium wires tend to be smeared due to energy relaxation, and that electrons can be excited to energy levels that are thermally forbidden. The energy relaxation collaborative between a pair of interacting wires leads to Coulomb drag, which was also simulated using our GW-CPA method. The simulation result suggested that around the linear transport regime the drag current peaks whenever the chemical potential sweeps across a band edge. It was also hinted that the drag charge current is closely associated with the energy transfer rate between the wires. Another theoretical achievement on Coulomb drag physics is that we have formulated an electron-hole symmetric relation for *nonequilibrium* drag currents: if the noninteracting Hamiltonian bears the electron-hole symmetry, the drag current is an odd function of the chemical potential.

Apart from scattering off static impurities, electrons also interact with the charge ripples induced by the disordered potential. The interference between the two processes leads to the Altshuler-Aronov (AA) effect which hinders electronic transport and suppresses the density of states at the Fermi energy. According to the conventional theory for macroscopic systems, the AA effect relies on a correlation length scale set by thermal diffusion. Our analysis showed that the AA effect persists in short mesoscopic wires where the correlation is yet cut off by the sample length. Because of this cutoff, the anomalous DOS correction is largely smeared, and it splits in two when the external bias is much greater than the Thouless energy. Besides, numerical computations showed that the inelastic scattering due to e-e interaction may further smear the DOS correction. As to the charge current correction, our result obtained under a local interaction model shows an asymptotic behavior in agreement with previous study [126] which adopted a screened long-range Coulomb potential.

This thesis has only focused on a limited number of quantum effects in disordered mesoscopic systems; some other subleading yet important many-body effects have not been covered. For example, the decoherence due to e-e interaction may suppress the Cooperon process. Taking this effect into account, the qualitative weak localization correction to electric conductivity (in one-dimension) should now read $\delta\sigma = -e^2h^{-1}L_\phi L/(L_\phi+L)$ [cf. Eq.(1.1)], according to Matthiessen's rule [23]. In addition, the Cooperon process also induces a correction to the AA effect [129]. The description of these physical effects involves more complex diagrams, which we shall address in future works. We also look forward to integrating the numerical methods developed in this thesis into an *ab initio* simulation framework, and eventually applying it to realistic materials of interesting structures.

Appendix A

Fourier transforms

In this thesis we adopt the following (continuous) Fourier transform convention:

$$f(\mathbf{k}) = \int f(\mathbf{r})\exp(-\mathrm{i}\mathbf{k}\cdot\mathbf{r})d^d r \tag{A.1a}$$

$$f(\mathbf{r}) = \int f(\mathbf{k})\exp(\mathrm{i}\mathbf{k}\cdot\mathbf{r})\frac{d^d k}{(2\pi)^d} \tag{A.1b}$$

$$f(\omega) = \int f(t)\exp(\mathrm{i}\omega t)dt \tag{A.2a}$$

$$f(t) = \int f(\omega)\exp(-\mathrm{i}\omega t)\frac{d\omega}{2\pi} \tag{A.2b}$$

The discrete (or the fast) Fourier transform and its inverse are defined as

$$y = \mathrm{FFT}(x) \to y_k = \sum_{j=0}^{N-1} x_j \Omega^{-j\cdot k} \tag{A.3a}$$

$$x = \mathrm{IFFT}(y) \to x_j = N^{-1}\sum_{k=0}^{N-1} y_k \Omega^{j\cdot k} \tag{A.3b}$$

where $\Omega = \exp(2\pi\mathrm{i}/N)$ and N is the number of sampling points on the signal. The discrete Fourier transform has the property that $y_{k+N} = y_k$ and $x_{j+N} = x_j$. Namely the algorithm is based on the assumption that the signal $y(t)$ is periodic over the received segment $T = N\Delta t$, Δt being the time interval between sampling points. Accordingly, the frequency interval on the spectrum $x(\omega)$ equals $\Delta\omega = 2\pi/T$, and the spectrum spans from 0 to $2\pi/\Delta t$. The purpose of introducing the discrete Fourier transform is to numerically compute Eq.(A.2) in an efficient way.

In the conventional theory of signal processing, times and frequencies are positive quantities. However, in many physical problems they can be negative. Think about the Green's functions

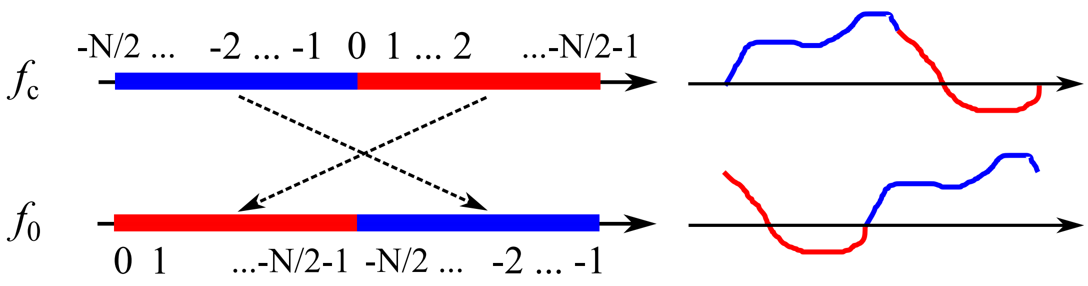

Figure A.1: Left: the swap operation on numeric arrays. Right: the signal curve is shifted by half the period.

which have been used a lot in this thesis. They can have well defined negative time or frequency arguments. For this reason, we need some extra operations about the Green's functions so as to fit them in the FFT algorithm. To be concrete we introduce the swap operation as illustrated in Fig.A.1. Usually the numerically computed Green's functions, in either time or frequency domain, have values on both sides of the zero point. Such kind of numeric series is denoted as f_c (see Fig.A.1), whose center is located at the zero point. To adapt the thus presented Green's function to the FFT algorithm, we sometimes need to swap its left half with its right half. The resulting series is denoted as f_0, whose first element corresponds to the zero-point value of the original Green's function, and whose middle element corresponds to the first one in f_c.

The continuous Fourier transform in Eq.(A.2b) is discretised as

$$f_c(t_0 + k\Delta t) = \int f_c(\omega) e^{-\mathrm{i}\omega(t_0+k\Delta t)} \frac{d\omega}{2\pi} \approx \frac{\Delta\omega}{2\pi} \sum_{j=0}^{N-1} f_c(\omega_0 + j\Delta\omega) \cdot e^{-\mathrm{i}(\omega_0 + j\Delta\omega)(t_0+k\Delta t)}, \quad \text{(A.4)}$$

where $\omega_0 = -\Delta\omega \cdot N/2$ is the lower bound of the frequency window in which $f_c(\omega)$ is evaluated. According to the FFT convention we set $t_0 = 0$ and hence obtain from Eq.(A.4)

$$f_0(k\Delta t) = \frac{\Delta\omega}{2\pi} \sum_{j=0}^{N-1} f_c((j - N/2)\Delta\omega) \cdot \Omega^{-(j-N/2)k}. \quad \text{(A.5)}$$

To proceed we split the sum in the middle:

$$\begin{aligned} f_0(k\Delta t) &= \frac{\Delta\omega}{2\pi} \sum_{j=N/2}^{N-1} f_c((j - N/2)\Delta\omega) \cdot \Omega^{-(j-N/2)k} + \frac{\Delta\omega}{2\pi} \sum_{j=0}^{N/2-1} f_c((j - N/2)\Delta\omega) \cdot \Omega^{-(j-N/2)k} \\ &= \frac{\Delta\omega}{2\pi} \sum_{j=N/2}^{N-1} f_c((j - N/2)\Delta\omega) \cdot \Omega^{-(j-N/2)k} + \frac{\Delta\omega}{2\pi} \sum_{j=0}^{N/2-1} f_c((j + N/2)\Delta\omega) \cdot \Omega^{-(j+N/2)k} \\ &= \frac{\Delta\omega}{2\pi} \sum_{j=0}^{N/2-1} f_0(j\Delta\omega) \cdot \Omega^{-j\cdot k} + \frac{\Delta\omega}{2\pi} \sum_{j=N/2}^{N-1} f_0(j\Delta\omega) \cdot \Omega^{-j\cdot k} = \frac{\Delta\omega}{2\pi} \mathrm{FFT} f_0(\omega). \quad \text{(A.6)} \end{aligned}$$

In the second line the periodic assumption of f_c is utilized, and in the third line f_c is swapped to f_0. Note that the resulting series f_0 starts at $t = 0$. To obtain the standard form where the zero-point sits at the center, we have to swap f_0 again back to f_c. Note that the Fourier transform of the convolutional integral Eq.(4.5b) is formulated under the f_c representation.

The integral in Eq.(A.2a) is carried out in a similar way:

$$f_c(\omega_0 + j\Delta\omega) = \int f_c(t) e^{i(\omega_0 + j\Delta\omega)t} dt \approx \Delta t \sum_{k=0}^{N-1} f_c((k - N/2)\Delta t) \cdot \Omega^{(j-N/2)(k-N/2)}. \tag{A.7}$$

Swapping both $f_c(\omega)$ and $f_c(t)$ to their f_0 representations, we get

$$f_0(j\Delta\omega) = \Delta t \sum_{k=0}^{N-1} f_c((k - N/2)\Delta t) \cdot \Omega^{j(k-N/2)} = \Delta t \sum_{k=0}^{N-1} f_0(k\Delta t) \cdot \Omega^{jk} = \frac{2\pi}{\Delta\omega} \mathrm{IFFT} f_0(t). \tag{A.8}$$

After performing the numerical FFT, we swap $f_0(\omega)$ back to the standard order (f_c).

Appendix B

Diffusive approximation

In theoretical analyses it is often convenient to assume an isotropic band dispersion, i.e. $E(\mathbf{k}) \to E(k)$. Hence the frequently encountered k-integration can be simplified as

$$\int \frac{d^dk}{(2\pi)^d} = \int dE\ \nu_0(E) \int \frac{d\Omega_{\mathbf{k}}}{S^d}, \tag{B.1}$$

where S^d denotes the surface area of the d-dimensional unit sphere: $S^d = 2, 2\pi, 4\pi$ for $d = 1, 2, 3$ respectively. As an application, let us compute the following integral:

$$\int \frac{d^dk}{(2\pi)^d} \left[G^{\mathrm{R}}(\mathbf{k}, \varepsilon)\right]^2 = \int_0^\infty \frac{\nu_0(\omega)}{(\varepsilon - \omega + \mathrm{i}/2\tau_0)^2} d\omega\ \approx \frac{\nu_0(\varepsilon)}{\varepsilon}. \tag{B.2}$$

In completing the ω-integral we made the observation that its major contribution comes from the region $\omega \sim \varepsilon$, since $\varepsilon\tau_0 \gg \hbar$ in the weak disorder limit. If one of the retarded Green's functions in Eq.(B.2) is replaced with G^{A},

$$\int \frac{d^dk}{(2\pi)^d} G^{\mathrm{R}}(\mathbf{k}, \varepsilon) G^{\mathrm{A}}(\mathbf{k}, \varepsilon) = \int_0^{+\infty} \frac{\nu_0(\omega) d\omega}{(\varepsilon - \omega + \mathrm{i}/2\tau_0)(\varepsilon - \omega - \mathrm{i}/2\tau_0)} \approx \gamma(\varepsilon)^{-1}, \tag{B.3}$$

where $\gamma(\varepsilon) = [2\pi\nu_0(\varepsilon)\tau_0(\varepsilon)]^{-1}$. In computing the integral above, again we have made use of the fact that the integrand decays rapidly away from $\omega = \varepsilon$. Therefore, the numerator is set at a constant $\nu_0(\varepsilon)$, and the residual theorem is invoked with a contour surrounding the upper half complex plane.

Noteworthily, the integral of Eq.(B.3) is greater than that of Eq.(B.2) by a factor of $\varepsilon\tau_0$. More generally one often encounters integrals of the form

$$\int \frac{d^dk}{(2\pi)^d} \left[G^{\mathrm{R}}(\mathbf{k}, \varepsilon)\right]^m \left[G^{\mathrm{A}}(\mathbf{k}, \varepsilon)\right]^n \equiv I^{m,n}. \tag{B.4}$$

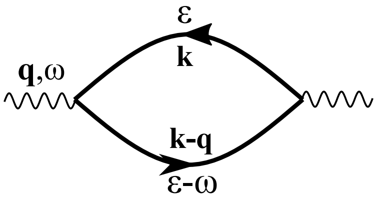

Figure B.1: Diagram for the integral of Eq.(B.6).

This nevertheless can always be reduced by using the identity

$$G^{\mathrm{R}}(\mathbf{k},\varepsilon)G^{\mathrm{A}}(\mathbf{k},\varepsilon)=\mathrm{i}\tau_0(\varepsilon)\left[G^{\mathrm{R}}(\mathbf{k},\varepsilon)-G^{\mathrm{A}}(\mathbf{k},\varepsilon)\right]. \tag{B.5}$$

The values of $I^{m,n}$ can be looked up in Table V of Ref.[131].

Next we consider the integral

$$\mathcal{P}_0(\mathbf{q},\omega)=\int\frac{d^dk}{(2\pi)^d}G^{\mathrm{R}}(\mathbf{k},\varepsilon)G^{\mathrm{A}}(\mathbf{k}-\mathbf{q},\varepsilon-\omega) \tag{B.6}$$

which is diagrammatically depicted in Fig.B.1. To proceed we employ the Taylor expansion

$$G^{\mathrm{A}}(\mathbf{k}-\mathbf{q},\varepsilon-\omega)=G^{\mathrm{A}}(\mathbf{k},\varepsilon)+(\omega-\mathbf{v}_{\mathbf{k}}\cdot\mathbf{q})\big[G^{\mathrm{A}}(\mathbf{k},\varepsilon)\big]^2+(\mathbf{v}_{\mathbf{k}}\cdot\mathbf{q})^2\big[G^{\mathrm{A}}(\mathbf{k},\varepsilon)\big]^3+\cdots, \tag{B.7}$$

where $\mathbf{v}_{\mathbf{k}}=\hbar^{-1}\nabla_{\mathbf{k}}E$ is the group velocity. We then get

$$\mathcal{P}_0(\mathbf{q},\omega)\approx I^{1,1}+\omega I^{1,2}+\frac{v_\varepsilon^2}{d}q^2I^{1,3}=(1+\mathrm{i}\omega\tau_0-D_\varepsilon q^2\tau_0)/\gamma, \tag{B.8}$$

where $D_\varepsilon=v_\varepsilon^2\tau_0/d$ is simply the diffusion coefficient. To get the coefficient in front of $I^{1,3}$ we used the identity

$$\int\frac{d\Omega_{\mathbf{k}}}{S^d}(\hat{\mathbf{k}}\cdot\mathbf{q}_1)(\hat{\mathbf{k}}\cdot\mathbf{q}_2)=\frac{\mathbf{q}_1\cdot\mathbf{q}_2}{d}. \tag{B.9}$$

In chapter 3 we see that the diffusion process is described by the correlator $\left\langle G^{\mathrm{R}}G^{\mathrm{A}}\right\rangle$ which is expanded as a recursive ladder series. Therefore,

$$\left\langle G^{\mathrm{R}}G^{\mathrm{A}}\right\rangle\to\mathcal{L}(\omega,\mathbf{q})=\mathcal{P}_0+\mathcal{P}_0\gamma\mathcal{L}=\frac{1}{\mathcal{P}_0^{-1}-\gamma}\approx\frac{2\pi\nu_0(\varepsilon)}{-\mathrm{i}\omega+D_\varepsilon q^2},\ \ \omega\tau_0,ql_0\ll1. \tag{B.10}$$

The approximation drawn above is valid under the condition $\omega\tau_0, ql_0\ll 1$, i.e. when the period of the driving field is much longer than the characteristic time or length scale of impurity scattering. This condition is termed the diffusive limit in the literature, which defines the classical regime of diffusive transport. More precisely, the probability propagation of a single particle (at energy ε) is written as $\mathcal{P}_\varepsilon=(2\pi\nu_0(\varepsilon))^{-1}\left\langle G^{\mathrm{R}}G^{\mathrm{A}}\right\rangle$ [12]. Therefore,

$$\mathcal{P}_{\mathrm{d}}(\omega,\mathbf{q})=\left(-\mathrm{i}\omega+Dq^2\right)^{-1},\ \ \omega\tau_0,ql_0\ll1, \tag{B.11}$$

where the subscript "d" represents "diffusion", and the ε argument is omitted since in practice it usually equals the Fermi energy. In real-space, Eq.(B.11) transforms to

$$\left(-\mathrm{i}\omega - D\frac{\partial^2}{\partial \mathbf{r}'^2}\right)\mathcal{P}_{\mathrm{d}}(\mathbf{r},\mathbf{r}',\omega) = \delta(\mathbf{r}-\mathbf{r}'), \tag{B.12}$$

which is just the classical diffusion equation. In fact Eq.(B.12) can be shown to be valid as well in systems that lack translational invariance [12].

As an application of Eq.(B.12), we consider a diffusive wire subject to the absorbing (Dirichlet) boundary condition, i.e. $\mathcal{P}_{\mathrm{d}}(x,x',\omega)=0$ at $x(x')=0(L)$. This standard textbook problem has the following solution:

$$\mathcal{P}_{\mathrm{d}}(x,x',\omega) = \frac{2}{L}\sum_{n>0}\frac{\sin(n\pi x/L)\sin(n\pi x'/L)}{\pi^2 n^2 D/L^2 - \mathrm{i}\omega}. \tag{B.13}$$

Using the mathematical identity

$$\sum_{n>0}\frac{\cos nx}{n^2+a^2} = \frac{\pi}{2a}\frac{\cosh a(\pi-|x|)}{\sinh \pi a} - \frac{1}{2a^2}, \tag{B.14}$$

we obtain

$$\begin{aligned}\mathcal{P}_{\mathrm{d}}(x,x',\omega) &= \frac{L_\omega}{2D}\frac{\cosh(L-|x-x'|)/L_\omega - \cosh(L-|x+x'|)/L_\omega}{\sinh(L/L_\omega)}\\ &= \frac{L_\omega}{D}\frac{\sinh(x_m/L_\omega)\cdot\sinh(L-x_M)/L_\omega}{\sinh(L/L_\omega)},\end{aligned} \tag{B.15}$$

where $x_m = \min(x,x')$, $x_M = \max(x,x')$, and $L_\omega = \sqrt{\mathrm{i}D/\omega}$. The square root follows the convention that the result falls in the right half of the complex plane.

Because of the momentum relaxation, the single-particle Green's function $G^{\mathrm{R/A}}$ is spatially confined within a region on the scale of l_0. For studying the single-particle dynamics (e.g. impurity-electron scattering), it suffices to focus only on a local region. Since the system is assumed to be macroscopically homogeneous, microscopic properties such as the relaxation time or cross-sections are uniform in the space. However, there are certain macroscopic objects that vary on a length scale greater than l_0. One example is the diffusion propagator discussed above. Interestingly, although the $G^{\mathrm{R}}G^{\mathrm{A}}$ pair depicted in Fig.B.1 is definitely short-ranged in real-space, when many of such pairs are strung together they form a long-ranged object. Another important quantity that varies in space macroscopically is the statistical distribution, which is encoded in the nonequilibrium Green's functions $G^{\mathrm{K}/>/<}$.[1] To conceptually separate the short and the long-ranged parts

---

[1] Note that the Green's functions are gauge-dependent. Suppose we have a static electric field represented by a scalar potential linear in the space. In this case we obtain Green's functions which also vary in the space. However, if the scalar potential is replaced with a vector potential $\mathbf{A}(t) = \mathbf{E}t$, the resulting Green's functions would be spatially independent. The reader is redirected to Ref.[44] as for how to construct gauge-invariant Green's functions.

of a given two-point function, one often employs the Wigner transformation [44, 60]. To this end we express the Green's function $G(\mathbf{r}_1, \mathbf{r}_2; \varepsilon)$ using the center of mass and relative coordinates $\mathbf{R} = (\mathbf{r}_1 + \mathbf{r}_2)/2, \mathbf{r} = (\mathbf{r}_1 - \mathbf{r}_2)$, and then perform the Fourier transform

$$G(\mathbf{R}, \mathbf{k}; \varepsilon) = \int G(\mathbf{R}, \mathbf{r}; \varepsilon) \exp(-\mathrm{i}\mathbf{k} \cdot \mathbf{r}) d\mathbf{r}. \tag{B.16}$$

Within this representation, the charge current can be expressed as

$$\mathbf{j}(\mathbf{R}) = \frac{e}{m} \int \frac{d\varepsilon}{2\pi\mathrm{i}} \int \frac{d\mathbf{k}}{(2\pi)^d} (\hbar\mathbf{k} - e\mathbf{A}) G^{<}(\mathbf{R}, \mathbf{k}; \varepsilon), \tag{B.17}$$

where $\mathbf{A}$ is vector potential of magnetic field. Note that, in contrast to G^{R} or G^{A}, $G^{\mathrm{K},>,<}$ have an explicit dependency on the macroscopic spatial coordinate $\mathbf{R}$, because of the particle occupation $f(\mathbf{R}, \varepsilon)$ in nonequilibrium.

Appendix C

Electron-hole symmetry in nonequilibrium Coulomb drag

It has been known that the linear response drag (charge) current due to the elementary e-e scattering exists only under certain electron-hole *asymmetric* conditions [42, 104, 106]. Taking undoped graphene as an example, when its occupation is set right at the electron-hole symmetric point, i.e. the Dirac point, the Coulomb drag was predicted to vanish [132].[1] In addition, the drag currents are equal when the chemical potential is set at mirroring points with respect to the electron-hole symmetric point. In this appendix, we show that this relation can be generalized to the nonequilibrium case. To be specific, for the system setup as illustrated in Fig.4.6, the drag current satisfies

$$I^{(p)}(\mu^{(a)},\mu^{(p)}) = -I^{(p)}(-\mu^{(a)},\mu^{(p)}) = -I^{(p)}(\mu^{(a)},-\mu^{(p)}) = I^{(p)}(-\mu^{(a)},-\mu^{(p)}), \tag{C.1}$$

given the sufficient condition that (i) the atomic structure and the hopping Hamiltonian of both subsystems bear inversion symmetry about the center of the device, (ii) independent on the chemical potentials, the electrostatic potential in the active wire is odd about the center of the device while that in the passive wire is zero everywhere, and (iii) the leads of respective subsystems are identical and have an electron-hole symmetric band structure. In the presence of disordered impurities, $I^{(p)}$ in Eq.(C.1) should be understood as the disorder-average drag current, and Eq.(C.1) remains true providing that the probability distribution of the impurity potential is even: $p(\varepsilon_i) = p(-\varepsilon_i)$. The proof of Eq.(C.1) is given in the following.

The noninteracting Hamiltonian of a two-terminal transport model has the following block-

---

[1] Nevertheless, we note that recent experiments showed an unexpected nonzero drag current at the graphene charge-neutrality point [133], which has been associated with disordered charge puddles due to materials imperfections [110, 134].

tridiagonal form:

$$\mathbf{H}_0 = \begin{bmatrix} \ddots & \mathbf{H}_{-m-1,-m} & & & \\ \mathbf{H}_{-m,-m-1} & \mathbf{H}_{-m,-m} + \mathbf{V}_{-m} & \mathbf{H}_{-m,-m+1} & & \\ & \mathbf{H}_{-m+1,-m} & \ddots & \mathbf{H}_{m-1,m} & \\ & & \mathbf{H}_{m,m-1} & \mathbf{H}_{m,m} + \mathbf{V}_m & \mathbf{H}_{m,m+1} \\ & & & \mathbf{H}_{m+1,m} & \ddots \end{bmatrix}$$

where m labels the principle layers, $\mathbf{H}$ denotes the corresponding hopping matrices, and $\mathbf{V}$ represents the diagonal potential matrices. In the active wire we have imposed $\mathbf{V}_{-m} = -\mathbf{V}_m$ while in passive wire we have $\mathbf{V} = 0$. For a real-space model with structural inversion symmetry, we have $\mathbf{H}_{mn} = \mathbf{H}_{-m,-n}$. In this case, eigenvectors of $\mathbf{H}_0$ emerge in pairs with opposite eigenvalues: Providing $\mathbf{\Psi}^{(\kappa)}$ is a certain eigenvector satisfying $\mathbf{H}_0\mathbf{\Psi}^{(\kappa)} = \epsilon^{(\kappa)}\mathbf{\Psi}^{(\kappa)}$, one can derive its pairing eigenvector $\mathbf{\Psi}^{(-\kappa)}$ which satisfies $\mathbf{H}_0\mathbf{\Psi}^{(-\kappa)} = \epsilon^{(-\kappa)}\mathbf{\Psi}^{(-\kappa)}$, where $\epsilon^{(-\kappa)} = -\epsilon^{(\kappa)}$ and $\psi_{-i}^{(-\kappa)*} = \psi_i^{(\kappa)}\eta_i$, i being a real-space index and η being a vector whose explicit form, although mathematically derivable, does not need to be known. Since $\mathbf{H}_0$ is real and because of the inversion symmetry, we have $|\psi_{-i}^{(-\kappa)}| = |\psi_i^{(\kappa)}|$ and thus the value of η_i can only be -1 or 1. Such eigenvector pairing reflects the physical picture that, if $\mathbf{\Psi}^{(\kappa)}$ corresponds to an electron scattering state incident from one side of the device, on the other half of the spectrum there should equally exist a hole state, denoted by $\mathbf{\Psi}^{(-\kappa)}$, incident from the other side.

Using the Lehmann representation, the retarded noninteracting Green's function can be formally written as [60]

$$G_{0,ij}^{\mathrm{R}}(E) = \sum_{\kappa} \frac{\psi_i^{(\kappa)}\psi_j^{(\kappa)*}}{E - \epsilon^{(\kappa)} + \mathrm{i}0^+}. \tag{C.2}$$

Using the symmetry of the wavefunction, we further get

$$G_{0,ij}^{\mathrm{R}}(E) = -\eta_i\eta_j \left[\sum_{\kappa} \frac{\psi_{-i}^{(-\kappa)}\psi_{-j}^{(-\kappa)*}}{-E - \epsilon^{(-\kappa)} + \mathrm{i}0^+} \right]^*. \tag{C.3}$$

The quantity in the bracket is easily recognized as $G_{0,-i,-j}^{\mathrm{R}}(-E)$. Thus we find $G_{0,ij}^{\mathrm{R}}(E) = -\eta_i\eta_j[G_{0,-i,-j}^{\mathrm{R}}(-E)]^*$. Similarly, taking into account the respective Fermi-Dirac distributions in the leads, the lesser Green's function can be written as [135]

$$G_{0,ij}^{<}(\mu, E) = \mathrm{i} \sum_{\alpha=\mathcal{L},\mathcal{R}} f(E - \mu_\alpha) \sum_{\kappa\in\alpha} \delta(E - \epsilon^{(\kappa)})\psi_i^{(\kappa)}\psi_j^{(\kappa)*}. \tag{C.4}$$

With some straightforward algebra, we can continue writing

$$G_{0,ij}^{<}(\mu, E) = \eta_i\eta_j \sum_{\alpha} \mathrm{i}\,[1 - f(-E + \mu_\alpha)] \sum_{\kappa\in\alpha} \delta(-E - \epsilon^{(-\kappa)})\psi_{-i}^{(-\kappa)*}\psi_{-j}^{(-\kappa)}$$

$$= \eta_i \eta_j \left[G^{>}_{0,-i,-j}(-\mu, -E)\right]^*, \tag{C.5}$$

where we have used the identities $\delta(x) = \delta(-x)$ and $1/(e^x+1) = 1-1/(e^{-x}+1)$. In the particular case $\mathbf{V} = 0$, in addition to the electron-hole symmetry, there emerges another pair of scattering states incident from opposite directions with the same energy and flipped wavefunctions. This leads to the relations $G^{\mathrm{R}}_{0,ij}(E) = G^{\mathrm{R}}_{0,-i,-j}(E)$ and $G^{</>}_{0,ij}(E) = G^{</>}_{0,-i,-j}(E)$.

Putting everything into context, upon flipping the sign of the chemical potential in the active wire ($\mu^{(a)} \to -\mu^{(a)}$) while keeping $\mu^{(p)}$ fixed, we have the noninteracting Green's functions change in the following way:

$$G^{\mathrm{R}(p)}_{ij}(\mu^{(a)}, E) = G^{\mathrm{R}(p)}_{-i,-j}(-\mu^{(a)}, E) \tag{C.6a}$$

$$G^{</>(p)}_{ij}(\mu^{(a)}, E) = G^{</>(p)}_{-i,-j}(-\mu^{(a)}, E) \tag{C.6b}$$

$$G^{\mathrm{R}(a)}_{ij}(\mu^{(a)}, E) = -\eta_i \eta_j \left[G^{\mathrm{R}(a)}_{-i,-j}(-\mu^{(a)}, -E)\right]^* \tag{C.6c}$$

$$G^{<(a)}_{ij}(\mu^{(a)}, E) = \eta_i \eta_j \left[G^{>(a)}_{-i,-j}(-\mu^{(a)}, -E)\right]^*, \tag{C.6d}$$

where we have omitted the 0 subscript as later on we will see that the interacting Green's functions also follow these relations. The argument $\mu^{(p)}$ has also been omitted for simpler notations. Plugging Eqs.(C.6b) and (C.6d) into Eq.(4.5a) and making use of the fact $\eta_i^2 = 1$, we get

$$P^{<(p/a)}_{ij}(\mu^{(a)}, E) = P^{<(p/a)}_{-i,-j}(-\mu^{(a)}, E) = \left[-P^{>(p/a)}_{-i,-j}(-\mu^{(a)}, -E)\right]^*. \tag{C.7}$$

Applying Eq.(C.7) to the Kramers-Kronig relation (4.6a), we find

$$P^{\mathrm{R}(p/a)}_{ij}(\mu^{(a)}, E) = P^{\mathrm{R}(p/a)}_{-i,-j}(-\mu^{(a)}, E). \tag{C.8}$$

In our Coulomb drag calculations, we take $W \approx VPV$. Therefore, according to Eq.(4.8), in conjunction with Eqs.(C.6b) and (C.6d), we have

$$\begin{aligned} \Sigma^{</>(p)}_{\mathrm{C},ij}(\mu^{(a)}, E) &= \Sigma^{</>(p)}_{\mathrm{C},-i,-j}(-\mu^{(a)}, E), \\ \Sigma^{<(a)}_{\mathrm{C},ij}(\mu^{(a)}, E) &= \eta_i \eta_j \left[\Sigma^{>(a)}_{\mathrm{C},-i,-j}(-\mu^{(a)}, -E)\right]^*. \end{aligned} \tag{C.9}$$

Using the Kramers-Kronig relation (4.6a) again, we get

$$\begin{aligned} \Sigma^{\mathrm{R}(p)}_{\mathrm{C},ij}(\mu^{(a)}, E) &= \Sigma^{\mathrm{R}(p)}_{\mathrm{C},-i,-j}(-\mu^{(a)}, E), \\ \Sigma^{\mathrm{R}(a)}_{\mathrm{C},ij}(\mu^{(a)}, E) &= -\eta_i \eta_j \left[\Sigma^{\mathrm{R}(a)}_{\mathrm{C},-i,-j}(-\mu^{(a)}, -E)\right]^*. \end{aligned} \tag{C.10}$$

Applying the relations (C.6), (C.9), and (C.10) to the recursive form of the Dyson equation $G^{\mathrm{R}} = G_0^{\mathrm{R}} + G_0^{\mathrm{R}}\Sigma_{\mathrm{C}}^{\mathrm{R}}G_0^{\mathrm{R}} + \cdots$[2] and the Keldysh equation [44] $G^{<} = (1 + G^{\mathrm{R}}\Sigma_{\mathrm{C}}^{\mathrm{R}})G_0^{<}(1 + G^{\mathrm{R}}\Sigma_{\mathrm{C}}^{\mathrm{R}})^{\dagger} + G^{\mathrm{R}}\Sigma_{\mathrm{C}}^{<}G^{\mathrm{R}\dagger}$, we immediately get back to Eq.(C.6). In the presence of disorder, the CPA iteration needs to be carried out as well. Using Eq.(C.6) together with the Eq.(3.18), one can easily verify that Σ_{CPA} follows the same relations as in Eqs.(C.9) and (C.10), providing that the impurity potential probability is an even function with respect to both the energy and the spatial position. Therefore, the relations in Eq.(C.6) stay true throughout the self-consistent calculation. Now we can draw conclusion about how the drag current changes when $\mu^{(a)}$ is flipped:

$$\begin{aligned}
I_{\mathrm{L}}^{(p)}(\mu^{(a)}, \mu^{(p)}) &= \int dE \mathrm{Tr}[G^{>(p)}(\mu^{(a)}, \mu^{(p)})\Sigma_{\mathrm{L}}^{<(p)} - G^{<(p)}(\mu^{(a)}, \mu^{(p)})\Sigma_{\mathrm{L}}^{>(p)}] \\
&= \int dE \mathrm{Tr}[G^{>(p)}(-\mu^{(a)}, \mu^{(p)})\Sigma_{\mathrm{R}}^{<(p)} - G^{<(p)}(-\mu^{(a)}, \mu^{(p)})\Sigma_{\mathrm{R}}^{>(p)}] \\
&= I_{\mathrm{R}}^{(p)}(-\mu^{(a)}, \mu^{(p)}) = -I_{\mathrm{L}}^{(p)}(-\mu^{(a)}, \mu^{(p)}),
\end{aligned} \tag{C.11}$$

where we have used the charge conservation law $I_{\mathrm{L}} + I_{\mathrm{R}} = 0$ and the simple fact about the lead self-energy: $\Sigma_{\mathrm{L},ij}^{</>(p)}(E) = \Sigma_{\mathrm{R},-i,-j}^{</>(p)}(E)$ due to the structural symmetry.

In the other situation where $\mu^{(a)}$ is fixed while $\mu^{(p)}$ is flipped instead, one can derive

$$\begin{aligned}
G_{ij}^{</>(p)}(\mu^{(p)}, E) &= \eta_i\eta_j\left[G_{ij}^{>/<(p)}(-\mu^{(p)}, -E)\right]^*, \\
\Sigma_{\mathrm{L},ij}^{</>(p)}(\mu^{(p)}, E) &= \eta_i\eta_j\left[\Sigma_{\mathrm{L},ij}^{>/<(p)}(-\mu^{(p)}, -E)\right]^*,
\end{aligned} \tag{C.12}$$

which leads to the other half of Eq.(C.1): $I_{\mathrm{L}}^{(p)}(\mu^{(a)}, \mu^{(p)}) = -I_{\mathrm{L}}^{(p)}(\mu^{(a)}, -\mu^{(p)})$.

---

[2] Taking the second term in the Dyson equation as an example, $G_{0,ik}^{\mathrm{R}(a)}\Sigma_{kl}^{\mathrm{R}(a)}G_{0,lj}^{\mathrm{R}(a)}(\mu^{(a)}, E) = [(-\eta_i\eta_k)\, G_{0,-i,-k}^{\mathrm{R}(a)} (-\eta_k\eta_l)\Sigma_{-k,-l}^{\mathrm{R}(a)}(-\eta_l\eta_j)G_{0,-l,-j}^{\mathrm{R}(a)}(-\mu^{(a)}, -E)]^* = (-\eta_i\eta_j)\, [G_{0,-i,-k}^{\mathrm{R}(a)}\Sigma_{-k,-l}^{\mathrm{R}(a)}G_{0,-l,-j}^{\mathrm{R}(a)}(-\mu^{(a)}, -E)]^*$. Repeated indices are summed over.

Bibliography

[1] C. Zhou and H. Guo, General theory for calculating disorder-averaged Green's function correlators within the coherent potential approximation, Phys. Rev. B **95**, 035126 (2017).

[2] C. Zhou and H. Guo, Nonequilibrium dual-fermion approach to electronic transport in disordered nanostructures, Phys. Rev. B **99**, 075414 (2019).

[3] C. Zhou and H. Guo, Coulomb drag between quantum wires: A nonequilibrium many-body approach, Phys. Rev. B **99**, 035423 (2019).

[4] C. Zhou and H. Guo, Altshuler-Aronov effects in nonequilibrium disordered nanostructures, Phys. Rev. B **100**, 045413 (2019).

[5] C. Zhou, X. Chen, and H. Guo, Theory of quantum transport in disordered systems driven by voltage pulse, Phys. Rev. B **94**, 075426 (2016).

[6] G. Giuliani and G. Vignale, *Quantum theory of the electron liquid* (Cambridge university press, 2005).

[7] N. Ashcroft and N. Mermin, *Solid State Physics* (Harcourt College, 1976).

[8] Y. Hu, Y. Zhu, H. Gao, and H. Guo, Conductance of an Ensemble of Molecular Wires: A Statistical Analysis, Phys. Rev. Lett. **95**, 156803 (2005).

[9] Y. M. Blanter and M. Büttiker, Shot noise in mesoscopic conductors, Physics reports **336**, 1 (2000).

[10] A. Anthore, *Decoherence mechanisms in mesoscopic conductors* (Ph.D. thesis, Universite Paris 6, 2003).

[11] B. Huard, *Interactions between electrons, mesoscopic Josephson effect and asymmetric current fluctuations* (Ph.D. thesis, Universite Paris 6, 2006).

[12] E. Akkermans and G. Montambaux, *Mesoscopic physics of electrons and photons* (Cambridge University Press, 2007).

[13] H. Grabert and M. Devoret, *Single Charge Tunneling: Coulomb Blockade Phenomena In Nanostructures* (Springer US, 1992).

[14] H. Pothier, S. Guéron, N. O. Birge, D. Esteve, and M. H. Devoret, Energy Distribution Function of Quasiparticles in Mesoscopic Wires, Phys. Rev. Lett. **79**, 3490 (1997).

[15] A. Anthore, F. Pierre, H. Pothier, and D. Esteve, Magnetic-Field-Dependent Quasiparticle Energy Relaxation in Mesoscopic Wires, Phys. Rev. Lett. **90**, 076806 (2003).

[16] P. Kim, T. W. Odom, J.-L. Huang, and C. M. Lieber, Electronic Density of States of Atomically Resolved Single-Walled Carbon Nanotubes: Van Hove Singularities and End States, Phys. Rev. Lett. **82**, 1225 (1999).

[17] S. Qin, T.-H. Kim, Y. Zhang, W. Ouyang, H. H. Weitering, C.-K. Shih, A. P. Baddorf, R. Wu, and A.-P. Li, Correlating electronic transport to atomic structures in self-assembled quantum wires, Nano letters **12**, 938 (2012).

[18] C. de Graaf, J. Caro, and S. Radelaar, Weak localization in short one-dimensional channels contacted by two-dimensional probes, Phys. Rev. B **46**, 12814 (1992).

[19] G. M. Minkov, O. E. Rut, A. V. Germanenko, A. A. Sherstobitov, V. I. Shashkin, O. I. Khrykin, and V. M. Daniltsev, Quantum corrections to the conductivity in two-dimensional systems: Agreement between theory and experiment, Phys. Rev. B **64**, 235327 (2001).

[20] F. Pierre, *Interactions electron-electron dans les fils mesoscopiques* (Ph.D. thesis, Universite Paris 6, 2000).

[21] B. L. Altshuler and A. G. Aronov, in *Electron-Electron Interactions in Disordered Systems* (Elsevier, 1985), vol. 10 of *Modern Problems in Condensed Matter Sciences*, pp. 1 – 153.

[22] J.-J. Lin and J. Bird, Recent experimental studies of electron dephasing in metal and semiconductor mesoscopic structures, J. Phys.: Condens. Matter **14**, R501 (2002).

[23] I. L. Aleiner, B. L. Altshuler, and M. E. Gershenson, Interaction effects and phase relaxation in disordered systems, Waves in Random Media **9**, 201 (1999).

[24] Y. Imry, *Introduction to Mesoscopic Physics*, Mesoscopic physics and nanotechnology (Oxford University Press, 2002).

[25] K. K. Choi, D. C. Tsui, and S. C. Palmateer, Electron-electron interactions in GaAs-$\mathrm{Al_xGa_{1-x}}$As heterostructures, Phys. Rev. B **33**, 8216 (1986).

[26] M. A. López de la Torre, Z. Sefrioui, D. Arias, M. Varela, J. E. Villegas, C. Ballesteros, C. León, and J. Santamaría, Electron-electron interaction and weak localization effects in badly metallic $\mathrm{SrRuO_3}$, Phys. Rev. B **63**, 052403 (2001).

[27] I. S. Beloborodov, A. V. Lopatin, V. M. Vinokur, and K. B. Efetov, Granular electronic systems, Rev. Mod. Phys. **79**, 469 (2007).

[28] W. L. McMillan and J. Mochel, Electron Tunneling Experiments on Amorphous $\mathrm{Ge}_{1-x}\mathrm{Au}_x$, Phys. Rev. Lett. **46**, 556 (1981).

[29] R. Escudero, J. Lasjaunias, Y. Calvayrac, and M. Boudard, Tunnelling and point contact spectroscopy of the density of states in quasicrystalline alloys, J. Phys.: Condens. Matter **11**, 383 (1999).

[30] D. Mazur, K. E. Gray, J. F. Zasadzinski, L. Ozyuzer, I. S. Beloborodov, H. Zheng, and J. F. Mitchell, Redistribution of the density of states due to Coulomb interactions in $\mathrm{La}_{2-2x}\mathrm{Sr}_{1+2x}\mathrm{Mn_2O_7}$, Phys. Rev. B **76**, 193102 (2007).

[31] N. Ossi, L. Bitton, D. B. Gutman, and A. Frydman, Zero-bias anomaly in a two-dimensional granular insulator, Phys. Rev. B **87**, 115137 (2013).

[32] G. Mahan, *Many-particle physics* (Plenum Press, New York, NY, 1981).

[33] G. Stefanucci and R. Van Leeuwen, *Nonequilibrium Many-Body Theory of Quantum Systems: A Modern Introduction* (Cambridge University Press, 2013).

[34] P. A. Lee and T. V. Ramakrishnan, Disordered electronic systems, Rev. Mod. Phys. **57**, 287 (1985).

[35] A. D. Franklin, M. Luisier, S.-J. Han, G. Tulevski, C. M. Breslin, L. Gignac, M. S. Lundstrom, and W. Haensch, Sub-10 nm carbon nanotube transistor, Nano Lett. **12**, 758 (2012).

[36] S. B. Desai, S. R. Madhvapathy, A. B. Sachid, J. P. Llinas, Q. Wang, G. H. Ahn, G. Pitner, M. J. Kim, J. Bokor, C. Hu, et al., $\mathrm{MoS_2}$ transistors with 1-nanometer gate lengths, Science **354**, 99 (2016).

[37] C. Qiu, F. Liu, L. Xu, B. Deng, M. Xiao, J. Si, L. Lin, Z. Zhang, J. Wang, H. Guo, et al., Dirac-source field-effect transistors as energy-efficient, high-performance electronic switches, Science **361**, 387 (2018).

[38] C. Kane, R. Serota, and P. Lee, Long-range correlations in disordered metals, Phys. Rev. B **37**, 6701 (1988).

[39] M. B. Hastings, A. D. Stone, and H. U. Baranger, Inequivalence of weak localization and coherent backscattering, Phys. Rev. B **50**, 8230 (1994).

[40] J. Taylor, H. Guo, and J. Wang, *Ab initio* modeling of quantum transport properties of molecular electronic devices, Phys. Rev. B **63**, 245407 (2001).

[41] D. Stradi, U. Martinez, A. Blom, M. Brandbyge, and K. Stokbro, General atomistic approach for modeling metal-semiconductor interfaces using density functional theory and nonequilibrium Green's function, Phys. Rev. B **93**, 155302 (2016).

[42] B. N. Narozhny and A. Levchenko, Coulomb drag, Rev. Mod. Phys. **88**, 025003 (2016).

[43] A. Kamenev, *Field theory of non-equilibrium systems* (Cambridge University Press, 2011).

[44] H. Haug and A.-P. Jauho, *Quantum Kinetics in Transport and Optics of Semiconductors* (Springer, Berlin, 2008).

[45] L. V. Keldysh, Diagram technique for nonequilibrium processes, Sov. Phys. JETP **20**, 1018 (1965).

[46] K. Levin, B. Velický, and H. Ehrenreich, Electronic Transport in Alloys: Coherent-Potential Approximation, Phys. Rev. B **2**, 1771 (1970).

[47] Y. Zhu, L. Liu, and H. Guo, Green's function theory for predicting device-to-device variability, Phys. Rev. B **88**, 085420 (2013).

[48] A. Gonis, *Green functions for ordered and disordered systems*, Studies in mathematical physics (North-Holland, 1992).

[49] G. Baym and L. P. Kadanoff, Conservation laws and correlation functions, Phys. Rev. **124**, 287 (1961).

[50] J. Yan and Y. Ke, Generalized nonequilibrium vertex correction method in coherent medium theory for quantum transport simulation of disordered nanoelectronics, Phys. Rev. B **94**, 045424 (2016).

[51] L. Hedin, New Method for Calculating the One-Particle Green's Function with Application to the Electron-Gas Problem, Phys. Rev. **139**, A796 (1965).

[52] G. Baym, Self-consistent approximations in many-body systems, Phys. Rev. **127**, 1391 (1962).

[53] J. Negele and H. Orland, *Quantum many-particle systems*, Frontiers in physics (Addison-Wesley Pub. Co., 1988).

[54] N. Bickers, Parquet equations for numerical self-consistent-field theory, Int. J. Mod. Phys. B **5**, 253 (1991).

[55] K. S. Thygesen and A. Rubio, Conserving GW scheme for nonequilibrium quantum transport in molecular contacts, Phys. Rev. B **77**, 115333 (2008).

[56] M. Srednicki, *Quantum field theory* (Cambridge University Press, 2007).

[57] B. Velický, Theory of electronic transport in disordered binary alloys: coherent-potential approximation, Phys. Rev. **184**, 614 (1969).

[58] Y. Zhu, L. Liu, and H. Guo, Quantum transport theory with nonequilibrium coherent potentials, Phys. Rev. B **88**, 205415 (2013).

[59] M. L. Sancho, J. L. Sancho, and J. Rubio, Highly convergent schemes for the calculation of bulk and surface Green functions, J. Phys. F: Met. Phys. **15**, 851 (1985).

[60] S. Datta, *Electronic Transport in Mesoscopic Systems* (Cambridge University Press, Cambridge, UK, 1997).

[61] H.-Z. Lu and S.-Q. Shen, Weak antilocalization and interaction-induced localization of Dirac and Weyl Fermions in topological insulators and semimetals, Chinese Physics B **25**, 117202 (2016).

[62] Y. Ke, K. Xia, and H. Guo, Disorder scattering in magnetic tunnel junctions: Theory of nonequilibrium vertex correction, Phys. Rev. Lett. **100**, 166805 (2008).

[63] E. Abrahams, P. W. Anderson, D. C. Licciardello, and T. V. Ramakrishnan, Scaling Theory of Localization: Absence of Quantum Diffusion in Two Dimensions, Phys. Rev. Lett. **42**, 673 (1979).

[64] E. Abrahams, *50 years of Anderson Localization* (World Scientific, 2010).

[65] T. Matsubara and Y. Toyozawa, Theory of Impurity Band Conduction in Semiconductors: An Approach to Random Lattice Problem, Prog. Theor. Phys **26**, 739 (1961).

[66] J. A. Blackman, D. M. Esterling, and N. F. Berk, Generalized Locator—Coherent-Potential Approach to Binary Alloys, Phys. Rev. B **4**, 2412 (1971).

[67] R. J. Elliott, J. A. Krumhansl, and P. L. Leath, The theory and properties of randomly disordered crystals and related physical systems, Rev. Mod. Phys. **46**, 465 (1974).

[68] P. Soven, Coherent-potential model of substitutional disordered alloys, Phys. Rev. **156**, 809 (1967).

[69] D. Taylor, Vibrational properties of imperfect crystals with large defect concentrations, Phys. Rev. **156**, 1017 (1967).

[70] P. L. Leath, Equivalence of Expanding in Localized or Bloch States in Disordered Alloys, Phys. Rev. B **2**, 3078 (1970).

[71] I. Turek, V. Drchal, J. Kudrnovsky, M. Sob, and P. Weinberger, *Electronic structure of disordered alloys, surfaces and interfaces* (Kluwer, Boston, 1997).

[72] S. Lowitzer, M. Gradhand, D. Ködderitzsch, D. V. Fedorov, I. Mertig, and H. Ebert, Extrinsic and Intrinsic Contributions to the Spin Hall Effect of Alloys, Phys. Rev. Lett. **106**, 056601 (2011).

[73] Q. Zhang, J. Yan, Y. Zhang, and Y. Ke, Exact muffin tin orbital based first-principles method for electronic-structure and electron-transport simulation of device materials, Phys. Rev. B **100**, 075134 (2019).

[74] E. Runge and H. Ehrenreich, Non-equilibrium transport in alloy based resonant tunneling systems, Ann. Phys. **219**, 55 (1992).

[75] A. Georges, G. Kotliar, W. Krauth, and M. J. Rozenberg, Dynamical mean-field theory of strongly correlated fermion systems and the limit of infinite dimensions, Rev. Mod. Phys. **68**, 13 (1996).

[76] N. Goldenfeld, *Lectures on phase transitions and the renormalization group*, Frontiers in physics (Addison-Wesley, Advanced Book Program, 1992).

[77] A. N. Rubtsov, M. I. Katsnelson, A. I. Lichtenstein, and A. Georges, Dual fermion approach to the two-dimensional Hubbard model: Antiferromagnetic fluctuations and Fermi arcs, Phys. Rev. B **79**, 045133 (2009).

[78] G. Rohringer, H. Hafermann, A. Toschi, A. A. Katanin, A. E. Antipov, M. I. Katsnelson, A. I. Lichtenstein, A. N. Rubtsov, and K. Held, Diagrammatic routes to nonlocal correlations beyond dynamical mean field theory, Rev. Mod. Phys. **90**, 025003 (2018).

[79] D. Boies, C. Bourbonnais, and A. M. S. Tremblay, One-Particle and Two-Particle Instability of Coupled Luttinger Liquids, Phys. Rev. Lett. **74**, 968 (1995).

[80] S. Pairault, D. Sénéchal, and A.-M. S. Tremblay, Strong-Coupling Expansion for the Hubbard Model, Phys. Rev. Lett. **80**, 5389 (1998).

[81] S. K. Sarker, A new functional integral formalism for strongly correlated Fermi systems, Journal of Physics C: Solid State Physics **21**, L667 (1988).

[82] H. Terletska, S.-X. Yang, Z. Y. Meng, J. Moreno, and M. Jarrell, Dual fermion method for disordered electronic systems, Phys. Rev. B **87**, 134208 (2013).

[83] E. Muñoz, C. J. Bolech, and S. Kirchner, Universal Out-of-Equilibrium Transport in Kondo-Correlated Quantum Dots: Renormalized Dual Fermions on the Keldysh Contour, Phys. Rev. Lett. **110**, 016601 (2013).

[84] P. Haase, S.-X. Yang, T. Pruschke, J. Moreno, and M. Jarrell, Dual-fermion approach to the Anderson-Hubbard model, Phys. Rev. B **95**, 045130 (2017).

[85] G. Li, Hidden physics in the dual-fermion approach: A special case of a nonlocal expansion scheme, Phys. Rev. B **91**, 165134 (2015).

[86] P. Wölfle and D. Vollhardt, Self-consistent theory of Anderson localization: General formalism and applications, Int. J. Mod. Phys. B **24**, 1526 (2010).

[87] P. Sheng, *Introduction to Wave Scattering, Localization and Mesoscopic Phenomena*, Springer Series in Materials Science (Springer Berlin Heidelberg, 2006).

[88] D. Vollhardt and P. Wölfle, Diagrammatic, self-consistent treatment of the Anderson localization problem in $d \leq 2$ dimensions, Phys. Rev. B **22**, 4666 (1980).

[89] J. Kroha, T. Kopp, and P. Wölfle, Self-consistent theory of Anderson localization for the tight-binding model with site-diagonal disorder, Phys. Rev. B **41**, 888 (1990).

[90] T. Markussen, R. Rurali, A.-P. Jauho, and M. Brandbyge, Scaling Theory Put into Practice: First-Principles Modeling of Transport in Doped Silicon Nanowires, Phys. Rev. Lett. **99**, 076803 (2007).

[91] L. G. Caron and C. Bourbonnais, Two-cutoff renormalization and quantum versus classical aspects for the one-dimensional electron-phonon system, Phys. Rev. B **29**, 4230 (1984).

[92] C. Bourbonnais and L. G. Caron, *Renormalization group approach to quasi-one-dimensional conductors, in Series on Advances in Statistical Mechanics* (World Scientific, 1991).

[93] R. Shankar, Renormalization-group approach to interacting fermions, Rev. Mod. Phys. **66**, 129 (1994).

[94] T. Giamarchi, *Quantum physics in one dimension*, vol. 121 (Oxford university press, 2004).

[95] Y. Jompol, C. Ford, J. Griffiths, I. Farrer, G. Jones, D. Anderson, D. Ritchie, T. Silk, and A. Schofield, Probing spin-charge separation in a Tomonaga-Luttinger liquid, Science **325**, 597 (2009).

[96] H. Ishii, H. Kataura, H. Shiozawa, H. Yoshioka, H. Otsubo, Y. Takayama, T. Miyahara, S. Suzuki, Y. Achiba, M. Nakatake, et al., Direct observation of Tomonaga–Luttinger-liquid state in carbon nanotubes at low temperatures, Nature **426**, 540 (2003).

[97] J. Voit, One-dimensional Fermi liquids, Rep. Prog. Phys **58**, 977 (1995).

[98] M. Grumet, P. Liu, M. Kaltak, J. Klimes, and G. Kresse, Beyond the quasiparticle approximation: Fully self-consistent GW calculations, Phys. Rev. B **98**, 155143 (2018).

[99] M. Strange, C. Rostgaard, H. Häkkinen, and K. S. Thygesen, Self-consistent GW calculations of electronic transport in thiol- and amine-linked molecular junctions, Phys. Rev. B **83**, 115108 (2011).

[100] W. H. Press, *Numerical recipes 3rd edition: The art of scientific computing* (Cambridge university press, 2007).

[101] P. Pulay, Convergence acceleration of iterative sequences: the case of scf iteration, Chem. Phys. Lett. **73**, 393 (1980).

[102] G. Kresse and J. Furthmüller, Efficiency of ab-initio total energy calculations for metals and semiconductors using a plane-wave basis set, Comput. Mater. Sci. **6**, 15 (1996).

[103] A.-P. Jauho and H. Smith, Coulomb drag between parallel two-dimensional electron systems, Phys. Rev. B **47**, 4420 (1993).

[104] A. M. Lunde, K. Flensberg, and A.-P. Jauho, Intershell resistance in multiwall carbon nanotubes: A Coulomb drag study, Phys. Rev. B **71**, 125408 (2005).

[105] K. Flensberg, B. Y.-K. Hu, A.-P. Jauho, and J. M. Kinaret, Linear-response theory of Coulomb drag in coupled electron systems, Phys. Rev. B **52**, 14761 (1995).

[106] A. Kamenev and Y. Oreg, Coulomb drag in normal metals and superconductors: Diagrammatic approach, Phys. Rev. B **52**, 7516 (1995).

[107] A. Kamenev and A. Levchenko, Keldysh technique and non-linear σ-model: basic principles and applications, Advances in Physics **58**, 197 (2009).

[108] A. L. Chudnovskiy, Double quantum dot as a probe of nonequilibrium charge fluctuations at the quantum point contact, Phys. Rev. B **80**, 081309 (2009).

[109] N. A. Mortensen, K. Flensberg, and A.-P. Jauho, Mesoscopic fluctuations of Coulomb drag between quasiballistic one-dimensional wires, Phys. Rev. B **65**, 085317 (2002).

[110] J. C. W. Song and L. S. Levitov, Energy-Driven Drag at Charge Neutrality in Graphene, Phys. Rev. Lett. **109**, 236602 (2012).

[111] D. Laroche, G. Gervais, M. Lilly, and J. Reno, 1D-1D Coulomb drag signature of a Luttinger liquid, Science **343**, 631 (2014).

[112] D. Nandi, A. Finck, J. Eisenstein, L. Pfeiffer, and K. West, Exciton condensation and perfect Coulomb drag, Nature **488**, 481 (2012).

[113] S. S. Apostolov, A. Levchenko, and A. V. Andreev, Hydrodynamic Coulomb drag of strongly correlated electron liquids, Phys. Rev. B **89**, 121104 (2014).

[114] V. L. Gurevich, V. B. Pevzner, and E. W. Fenton, Coulomb drag in the ballistic electron transport regime, J. Phys.: Condens. Matter **10**, 2551 (1998).

[115] O. Raichev and P. Vasilopoulos, Coulomb drag between parallel ballistic quantum wires, Phys. Rev. B **61**, 7511 (2000).

[116] G. Tang and J.-S. Wang, Heat transfer statistics in extreme-near-field radiation, Phys. Rev. B **98**, 125401 (2018).

[117] L. Ge, K. Gong, Y. Cang, Y. Luo, X. Shi, and Y. Wu, Magnetically tunable multiband near-field radiative heat transfer between two graphene sheets, Phys. Rev. B **100**, 035414 (2019).

[118] Y. Imry and Z. Ovadyahu, Density-of-States Anomalies in a Disordered Conductor: A Tunneling Study, Phys. Rev. Lett. **49**, 841 (1982).

[119] J. T. Masden and N. Giordano, Finite-size effects in the electrical conduction of thin wires, Phys. Rev. B **36**, 4197 (1987).

[120] G. Zala, B. N. Narozhny, and I. L. Aleiner, Interaction corrections at intermediate temperatures: Longitudinal conductivity and kinetic equation, Phys. Rev. B **64**, 214204 (2001).

[121] B. Altshuler, A. Aronov, and A. Y. Zyuzin, Size effects in disordered conductors, Sov. Phys. JETP **59**, 415 (1984).

[122] D. Belitz and T. R. Kirkpatrick, The Anderson-Mott transition, Rev. Mod. Phys. **66**, 261 (1994).

[123] C. Castellani, C. Di Castro, P. A. Lee, and M. Ma, Interaction-driven metal-insulator transitions in disordered fermion systems, Phys. Rev. B **30**, 527 (1984).

[124] A. M. Finkel'stein, Metal–insulator transition in a disordered system, Zh. Eksp. Teor. Fiz **86**, 367 (1984).

[125] G. Schwiete and A. M. Finkel'stein, Keldysh approach to the renormalization group analysis of the disordered electron liquid, Phys. Rev. B **89**, 075437 (2014).

[126] K. Nagaev, Nonlinear conductivity of diffusive normal-metal contacts, Phys. Lett. A **189**, 134 (1994).

[127] P. Schwab and R. Raimondi, Quasiclassical theory of charge transport in disordered interacting electron systems, Ann. Phys. **12**, 471 (2003).

[128] D. B. Gutman, Y. Gefen, and A. D. Mirlin, Nonequilibrium Zero-Bias Anomaly in Disordered Metals, Phys. Rev. Lett. **100**, 086801 (2008).

[129] H. Fukuyama, in *Electron-Electron Interactions in Disordered Systems* (Elsevier, 1985), vol. 10 of *Modern Problems in Condensed Matter Sciences*, pp. 155 – 230.

[130] F. Pierre, H. Pothier, P. Joyez, N. O. Birge, D. Esteve, and M. H. Devoret, Electrodynamic Dip in the Local Density of States of a Metallic Wire, Phys. Rev. Lett. **86**, 1590 (2001).

[131] S. Hershfield, Current conservation and resistance fluctuations in a four probe geometry, Ann. Phys. **196**, 12 (1989).

[132] W.-K. Tse, B. Y.-K. Hu, and S. Das Sarma, Theory of Coulomb drag in graphene, Phys. Rev. B **76**, 081401 (2007).

[133] R. Gorbachev, A. Geim, M. Katsnelson, K. Novoselov, T. Tudorovskiy, I. Grigorieva, A. MacDonald, S. Morozov, K. Watanabe, T. Taniguchi, et al., Strong Coulomb drag and broken symmetry in double-layer graphene, Nature Physics **8**, 896 (2012).

[134] D. Y. Ho, I. Yudhistira, B. Y.-K. Hu, and S. Adam, Theory of Coulomb drag in spatially inhomogeneous 2D materials, Communications Physics **1**, 41 (2018).

[135] J. Wang and H. Guo, Relation between nonequilibrium Green's function and Lippmann-Schwinger formalism in the first-principles quantum transport theory, Phys. Rev. B **79**, 045119 (2009).